Fiber Optic Sensor Fused Additive Manufacturing

by

Ran Zou

B. S., Huazhong University of Science and Technology, 2010

M. S., Arizona State University, 2012

Submitted to the Graduate Faculty of

The Swanson School of Engineering in partial fulfillment

of the requirements for the degree of

Doctor of Philosophy

University of Pittsburgh

2020

UNIVERSITY OF PITTSBURGH

SWANSON SCHOOL OF ENGINEERING

This dissertation was presented

by

Ran Zou

It was defended on

May 4, 2020

and approved by

Jun Chen, Ph.D., Assistant Professor
Department of Electrical and Computer Engineering

Minhee Yun, Ph.D., Professor
Department of Electrical and Computer Engineering

Paul R. Ohodnicki, Ph.D., Associate Professor
Department of Mechanical Engineering and Materials Science

Susheng Tan, Ph.D., Associate Professor
Department of Electrical and Computer Engineering

Zhi-Hong Mao, Ph.D., Professor
Department of Electrical and Computer Engineering

Dissertation Director: Kevin P. Chen, Ph.D., Professor
Department of Electrical and Computer Engineering

Fiber Optic Sensor Fused Additive Manufacturing

Ran Zou, Ph.D.

University of Pittsburgh, 2020

Since its first patent in 1967, fiber optic sensor has been extensively applied in numerous fields thanks to its outstanding physical properties. With the novel advances in additive manufacturing technology, there is of great opportunity to build smart objects with functional components or embedded sensors, such as fiber optic sensors, during the fabrication process. These embedded components are capable of providing real-time data and structural information to validate or improve engineering designs. Though there are already a number of reports about embedded fiber optic sensors in additive manufacturing application with low melting point materials like polymers, it is of enormous interest but also challenge to embed fiber optic sensors in metal or metal alloy due to the high melting temperatures.

In this dissertation, standard telecom-grade single-mode optical fibers were metalized by nickel sulfamate electroplating method and successfully embedded into objects with flat surfaces and curved surfaces serving as smart distributed sensors in metal additive manufacturing applications. Based on Rayleigh optical frequency domain reflectometry technology, the embedded fiber optic sensors were proficient in providing accurate and distributed temperature and strain sensing in real-time with 5 mm spatial resolution under extreme environments. Both experimental and simulation results were provided to demonstrate the sensing capability of the embedded smart fiber sensor in the applications of metal additive manufacturing. This smart sensor embedding technique was further applied into laser processing methods like laser shock peening to monitor its distributed strain evolution in real-time. Additionally, an advanced laser processing method was studied to fabricate and enhance 3D MEMS devices using spatially modulated laser beams via a spatial light modulator.

Table of Contents

List of Tables

List of Figures

Preface

I would like to give my deepest thanks to my advisor Prof. Kevin Chen for his continuous supports and advices over the past years of my graduate study. I sincerely appreciate the opportunity to learn and research under his guidance.

I would like to thank all my dissertation committee members: Prof. Jun Chen, Prof. Minhee Yun, Prof. Paul R. Ohodnicki, Prof. Susheng Tan, and Prof. Zhi-Hong Mao for their long support and patience in my research. Additionally, I own special thanks to Prof. Albert To, who gave me numerous supports and guidance in learning additive manufacturing technology and mechanical engineering from scratch.

I would also like to thank Dr. Hui Lan, Xuan Liang, Sheng Huang, Mohan Wang, Rongtao Cao, Jingyu Wu, Zhaoqiang Peng, Kehao Zhao and all my colleagues and friends. They are always willing to help me both in research and in daily life. I am always grateful to have them around.

Most importantly, I would like to thank my family, who support and encourage me in all these years of study and research. It is their love that keeps me going.

And finally, I would like to acknowledge the financial support from the Department of Energy. This work would not have been possible without them.

1.0 Introduction

The aim of this dissertation is to provide the basics for realization of embedded optical fiber sensors to monitor temperature change and residual strains in 3D-printed metal components. It integrates the embedding techniques for fiber optic sensor, together with other elements for additive manufacturing (AM) processing. To aid in this goal, this dissertation respectively investigates into the residual strain induced in electroplating process and the real-time temperature and strain monitoring in additive manufacturing and post-machining process like Laser shock peening (LSP).

In this dissertation, we discuss applications of optical fiber sensors to monitor temperature and residual strains in 3D-printed metal components. The AM process uses materials in the form of powder, wire, or liquid; and solidifies them with thermal or photochemical process. A main concern for all melting deposition-based AM applications is residual stresses which are generated and accumulated due to the large temperature gradient between the highly localized melting zone and the cold substrate [1]. These thermally induced residual stresses may lead to reduced performance including limited corrosion-resistance, warpage, loss of edge tolerance, and even delamination in finished parts. Mitigating the residual stress remains as one of the major challenges for metal-based 3D printing processes such as electron beam melting (EBM), selective laser melting (SLM), Laser Engineered Net Shaping (LENS), and others.

Embedded fiber sensors are promising tools for monitoring residual strains induced by the AM processes. Fiber sensors with proper protection can survive the extreme manufacturing temperatures involved in various 3D printing processes. More importantly, unmodified optical fibers are often used to perform distributed strain measurements with high spatial resolution. Based on optical frequency domain reflectometry (OFDR), Rayleigh back-scattering can be used to measure the strain exerted on a test fiber with measurement resolution down to 1 με and sub-cm spatial resolution [2-7]. By introducing OFDR technology to metal AM, it is possible to achieve distributed measurements to produce temperature and residual strain contour maps for the entire volume of a printed part.

In this dissertation, we report both the theoretical simulation of the stresses induced during deposition along with experimental measurements of those stresses in Inconel 718 metal alloy components fabricated with the LENS additive manufacturing process. Residual strains measured by the fiber sensors quantitatively agreed with the stress simulations. This information can be useful for reducing or mitigating residual strain during or following the manufacturing process. It can also be used to perform continuous monitoring of 3D-printed parts against corrosion and metal frailty in service. In addition, the technique to embedding optical fiber sensors into curved surface, like a 3D printed Ti-6Al-4V turbine blade, is discussed. Further static test with this sensor embedded turbine blade was measured and analyzed. The result shows that optical fiber sensors were successfully embedded into complex 3D shape components, and the static test results showed reasonable strain sensing capability of the smart component. Moreover, the embedded fiber optic sensors were applied in laser shock peening applications to monitor strain distribution in real-time. And additionally, an advanced laser processing technique using spatially modulated laser beam in micro-fabrication applications was discussed.

1.1 Introduction of Embedded Sensor in Smart Structures

Owing to the advancement in novel engineering and manufacturing techniques, integrating particular functioning components, such as sensors, micro-circuits, and actuators, into the system to fabricate smart structures becomes an increasingly trendy design philosophy in manufacturing process. These smart structures add valuable functionalities in system performance enhancement, structural health monitoring, structural vibration control and transportation engineering, and sensing certain stimuli and responding adaptively in a controlled manner.

An important application of smart structure is composite material with embedded sensors, which provides access to sense and react correspondingly to the environment. Numerous types of embedded sensors, like strain gauges, accelerometers, ultrasonic sensors, passive acoustic sensors, etc., have been reported in real-life applications. Based on their different working principles, embedded sensors may be characterized as passive sensors, such as fiber optic sensors (FOS, also known as optical fiber sensor) with many variations like the fiber optic Bragg grating sensors, pre-embedded concrete bar (PECB) sensors, corrosion sensors; and active sensors such as the piezoelectric wafer active sensors [8]. However, most of current electric based embedded sensors still suffer from limitations like unstable performance under electromagnetic interference (EMI), high manufacturing cost, engineering difficulties in embedding process, the final products are fragile or have limited working period in harsh environment, lack of durability or multiplexing capability [9].

For all these reasons, embedded optical fiber sensor has attracted serious attention from researchers and has become a new research trend. Fiber optic sensors have already been reported as an important device with excellent performance in real-time in-situ monitoring applications due to their numerous advantages, such as immunity to electromagnetic interference, small size, light weight, durability, and high bandwidth, which allows multiple optical fiber sensors to be integrated within the material and operate independently and simultaneously in the same system [9].

1.2 Fiber Optic Sensors in Additive Manufacturing

1.2.1 Review of Fiber Optic Sensors

Generally speaking, the main component of the fiber optic sensor is a small diameter waveguide made from glass fiber that confines light within its regions due to the total reflection of light, as a result of the difference in optical indices of refraction. Mostly, the fiber optic sensor contains optical fiber, a light source, sensing element, and a detector. When the sensor exposed to external perturbations such as strain, pressure, or temperature, the sensing element modulates certain parameters of the optical system, usually as intensity, wavelength, polarization, or phase, which in turn changes the characteristics of the optical signal received at the detector. As a result, the measured parameter changes then represent fluctuations in the environment. Thanks to its miniature size, the optical fiber sensors can be embedded within the structural material or bonded to the member surface for real-time damage assessment. Another advantage of the fiber optic sensor is that the sensor may serve as both the sensing element and a medium to transfer signal. So, the detecting or signal processing instruments can be located away from the sensor allowing remote monitoring of structures in localized, multiplexed, or distributed arrangement [8]. Fiber optic sensors have already been used in a wide range of application for monitoring strain, pressure, temperature, bending, loading, and cracking in numerous engineering structures.

A fiber optic sensor uses fiber optics either as the sensing element itself (intrinsic sensor), or as the means to transport optical signals to or from an actual sensor (extrinsic sensor). Since its first patent in 1967 [10], fiber optic sensors have been widely applied in sensing temperature, strain, displacement, vibration, pressure, acceleration, rotation, electromagnetic field, radiation, etc.; covering numerous industrial areas, like energy, aerospace, defense, and medical fields [11, 12]. In general, the working principle of an intrinsic FOS is converting environmental features into a light signal modulation, usually in the form of intensity, phase, frequency, and polarization. While for an extrinsic FOS, the optical fiber works as the data carrier. Compared with conventional electrical sensors, FOS shows advantages like small size, light weight, inexpensive price, multiplexing capability, intrinsic safety in harsh environment, immunity to EMI, etc. FOS has many configurations based on their different working principles, as illustrated in Fig. 1. The following sections will provide a more detailed introduction about interferometric fiber sensors, fiber grating sensors, and fiber sensors based on optical time/frequency domain reflectometry techniques (OTDR and OFDR). Each category includes a variety of concepts that have been employed for different measured and applications.

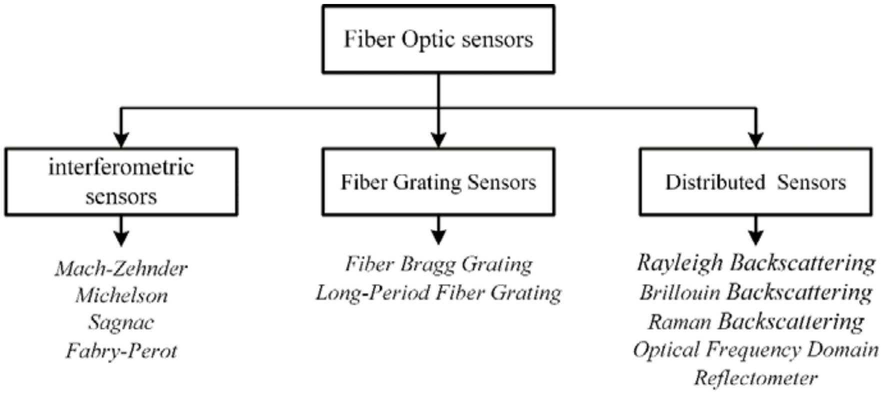

Figure 1 Overview of basic principles and types of fiber optic sensors.

1.2.1.1 Interferometric Fiber Sensors

Interferometric fiber optic sensor (IFOS) is a fiber-based interferometer which uses the interference between two light beams propagating through different optical paths in a single fiber or two fibers. Depending on different mechanical structures and operating principles, interferometric fiber sensors can be categorized as Mach-Zehnder, Michelson, Sagnac, and Fabry-Perot interferometers [13-17]. The scheme of each type of IFOS is given in Fig. 2.

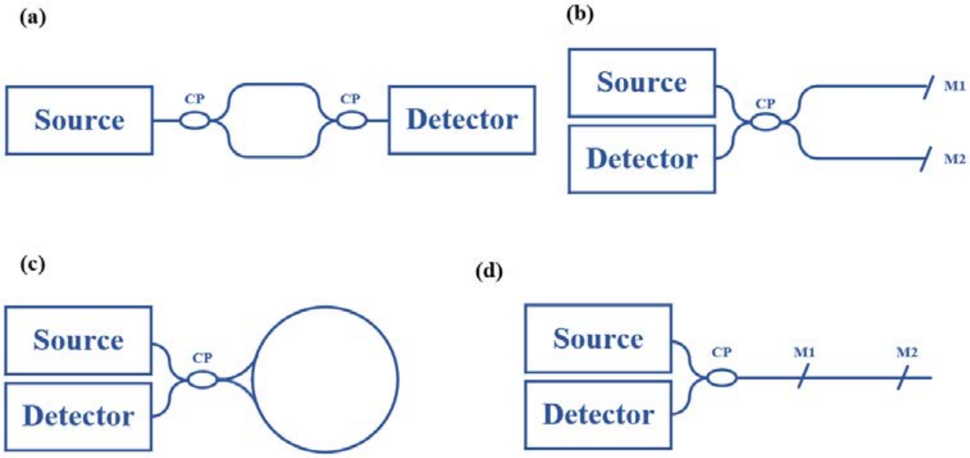

Figure 2 Schematic illustration of fiber-optic interferometers: (a) Mach-Zehnder (b) Michelson, (c) Sagnac, and (d) Fabry-Perot. CP: fiber coupler, M1 and M2: mirrors.

Mach-Zehnder Interferometer

Mach-Zehnder interferometer is a two-beam fiber optic interferometer [18, 19], as shown in Fig. 2b. The input light is divided by a fiber coupler into two beams propagating in the signal arm and reference arm, respectively. The two arms are then recombined through another fiber coupler and deliver the light signal into two photodetectors. When a small external environment disturbance is introduced to the signal beam, the phase of the light in the signal beam changes, which in turn affects the intensity of the optical fringes in the two photodetectors. By analyzing the intensity shift at the two outputs, the environmental disturbance on the signal arm can be determined.

Michelson Interferometer

Similar as Mach-Zehnder interferometer, Michelson interferometer is also a two-beam fiber optic interferometer [19] and they share comparable working principles. The output of the signal arm and reference arm are terminated by two mirrors. The reflected signals are combined at a fiber optic coupler and generate the interference signal captured by a photodetector.

Sagnac Interferometer

As shown in Fig. 2a. Sagnac interferometer is also a two-beam interferometer system. Nevertheless, unlike former two IFOSs, the two beams share the same optical fiber loop but with opposite directions using a fiber coupler. As the light travels in the two directions (usually known as clockwise (CW) and counterclockwise (CCW) directions, respectively) in the loop, the two beams recombined at the optical fiber coupler generating an interference fringe. When an external perturbation occurred near one end of the fiber loop, the length of the light path shifts resulting in a phase difference between two beams and finally leading to the interference fringe changes captured by a photodetector [18, 19].

Fabry-Perot Interferometer

A fiber Fabry-Perot interferometer (FFPI) is in general a multiple-beam interferometer system consisting of an on-fiber Fabry-Perot cavity. A Fabry-Perot interferometer (FPI) contains two mirrors with reflectance R_1 and R_2 (or transmittance T_1 and T_2, here $R_i + T_i = 1$, $i = 1, 2$) separated by an optically transparent cavity with length L. So, the total equivalent reflectance or transmittance of the cavity is given as:

$$R_{FPI} = \frac{R_1 + R_2 + 2\sqrt{R_1R_2}\cos\emptyset}{1 + R_1R_2 + 2\sqrt{R_1R_2}\cos\emptyset} \qquad (1-1)$$

$$T_{FPI} = \frac{T_1 + T_2}{1 + R_1R_2 + 2\sqrt{R_1R_2}\cos\emptyset} \qquad (1-2)$$

where $\emptyset = 4\pi nL/\lambda$ is the round-trip phase shift of the light in the FPI, as n is the refractive index of the cavity medium and λ is the free-space optical wavelength. Here an assumption is made that a π/2 phase shift is happened at each reflection. As a multi-beam interferometer system, FPI is extremely sensitive to environmental perturbations which induce changes in refractive index n or cavity length L [18-20].

Based on cavity structure configurations, fiber Fabry-Perot interferometers can be classified as intrinsic FPPI and extrinsic FPPI [21-25]. Fig. 3a-c show three configurations of intrinsic FPPIs. Such as in Fig. 3a where one end of fiber is cleaved of polished functioning as a mirror, while another reflector is internal to the fiber. Or, another structure may contain two internal mirrors in the fiber, as shown in Fig. 3b. These internal reflectors could be defects deliberately made by fusion splicers or lasers; or it may also be results from fusing uncoated fiber with optical fiber which has dielectric or metal coatings on one end [20]. The third structure of intrinsic FPPI is shown in Fig. 3c, where the two reflectors in the optical fiber are Fiber Bragg Gratings (FBG). These FBG mirrors are written by interfering two coherent UV laser beams on a single-mode fiber forming periodical low- and high-refractive index structures. Because of the nature of FBG, this type of FPPI is usually wavelength selective.

In comparison, Fig. 3d-g show four extrinsic FPPI configurations. In Fig. 3d, there is a diaphragm positioned near a cleaved or polished optical fiber, forming a Fabry-Perot cavity with micron level length between the fiber end and the diaphragm. The second configuration applies a film of transparent solid material on one end of fiber, in this case, the film itself is the cavity, as shown in Fig. 3e. FPPI structures like Fig. 3f use a single-mode fiber and a multi-mode fiber whose ends are polished or cleaved and positioned aligned with a short air gap in between. The last structure shown in Fig. 3g is also known as the "in-line fiber etalon", which uses a hollow core fiber to connect two single-mode fibers. The airgap in the hollow core fiber works as the cavity. Compared with intrinsic FFPIs whose sensing region is confined by the fiber core, extrinsic FFPIs suffer from optical loss due to diffraction, so their cavity length L are usually less than sub-millimeter level [19, 26-31].

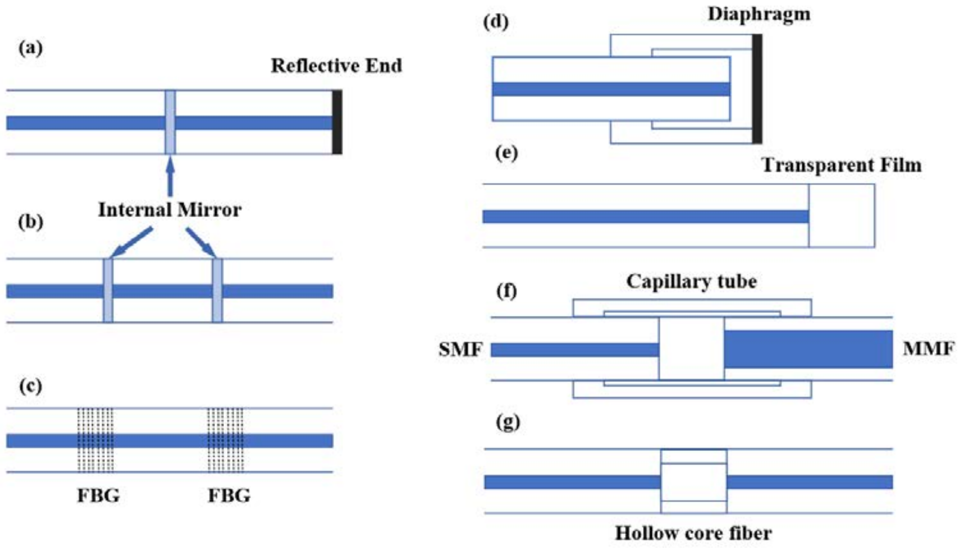

Figure 3 (a-c) Intrinsic and (d-g) extrinsic FPPI configurations.

Despite all these configurations, IFOSs are important sensing instruments in a wide range of applications, like underwater acoustic detection, voltage/current measurement in power field, and real-time biomedical pressure sensing [19, 32-35].

1.2.1.2 Fiber Grating Sensors

As one of the largest category of fiber optic sensors, the first formation of fiber gratings was reported in 1978 [36]. Ten years later, a more controllable and effective technique to write fiber gratings using a coherent ultraviolet (UV) two-beam interference pattern was reported [37]. Since then, intensive efforts have been spent on researching and developing fiber gratings and make it an excellent fiber optic communication and sensing element.

Fiber gratings have many configurations, as shown in Fig. 4. When phase matching condition satisfied, a fiber Bragg grating (FBG) couples light from the forward propagating core mode to the backward propagating core mode, just like shown in Fig.4a. While Fig. 4b shows that a long-period fiber grating (LPG) can couple light from the forward propagating core mode into forward propagating cladding mode.

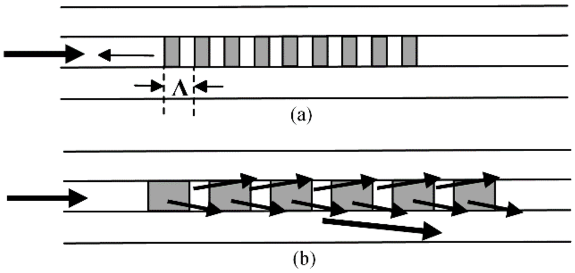

Figure 4 Types of fiber gratings: (a) Fiber Bragg gratings, (b) long-period fiber grating.

Fiber Bragg Grating Sensors

A fiber Bragg grating is a single-mode optical fiber whose core is exposed by an intense UV interference fringe pattern forming a periodical refractive index change in the fiber core. As shown in Fig. 5, there are two methods which are commonly used to form this interference fringe: either by a free-space two-beam holographic method, or through a diffractive phase mask [36-38].

Usually, to achieve higher sensitivity, fiber optics are preferred to be doped with hydrogen through H_2-loading method [39]. For a typical fiber Bragg grating, its physical length may be of a few millimeters and provide nearly total peak reflectivity with a reflection bandwidth less than 0.5 nm.

One of the most characteristic features of fiber Bragg grating is its narrow band reflection. At wavelength λ_B, given as the following formula, the incident light reaches the highest reflectivity.

$$\lambda_B = 2n_{eff}\Lambda \qquad (1-3)$$

where n_{eff} is the effective refractive index of the guided mode in the optical fiber and Λ is the period of the grating.

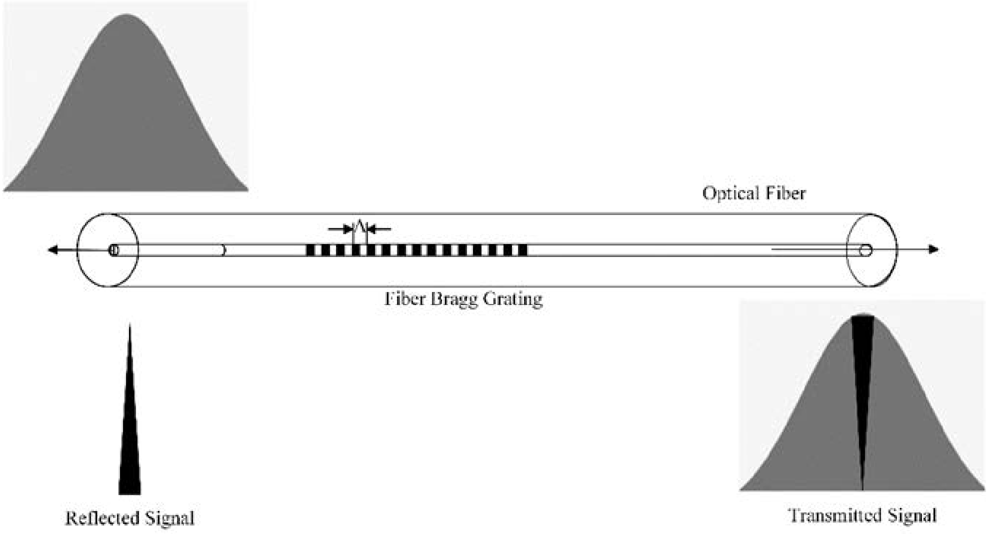

Figure 5 Schematic diagram of structure and spectral response of fiber bragg grating.

Temperature and strain sensing are two most popular applications for FBG sensors. When an external mechanical or thermal perturbation applied on an FBG, its refractive index or grating period changes. For a strain field, the pitch of the grating is expanded or compressed, directly causing a grating period shift. While sensing the temperature change of the FBG, it is principally through the thermal induced refractive index change of the fiber, while the thermal expansion coefficient of the fiber also has lesser effect on the measurement. The FBG calculates the strain or temperature change through the peak wavelength shift given as:

$$\frac{\Delta\lambda_B}{\lambda_B} = P_e\varepsilon + \left[P_e\left(\alpha_s - \alpha_f\right) + \varsigma\right]\Delta T \qquad (1-4)$$

where λ_B is the peak reflected wavelength; $\Delta\lambda_B$ is the wavelength shift due to thermal or mechanical perturbation; P_e is the strain-optic coefficient; α_s and α_f are the thermal expansion coefficients of surrounded fiber bonding material and fiber itself, respectively; ς is the thermal-optic coefficient; ε is the strain and ΔT is the temperature change [20].

Besides temperature and strain measurements, fiber Bragg gratings have been used in other sensing applications as well, like pressure, bending, load, vibration, acceleration, electromagnetic fields, and hydrogen [40-49]. Regardless of all these applications, their sensing mechanisms are more or less the same: Bragg wavelength shift induced by refractive index or grating period change. Additionally, by applying certain coatings on a D-shape fiber or side polished fiber, the FBG may also serve as chemical sensors too [50, 51].

Another characteristic of FBG is its capability for multiplexing sensing. In many applications where more than one sensor is required in the measurement, FBG is a great choice since multiple gratings can be written on a single fiber. Similar as in telecommunication applications, the FBG multiplexing techniques include wavelength division multiplexing (WDM), time division multiplexing (TDM), code division multiple access (CDMA), intensity and wavelength dual- coding multiplexing (IWDM), and spatial division multiplexing (SDM) [20, 52].

These multiplexing techniques turn FBG into a quasi-distributed sensing system that data can be collected at multiple points where the gratings exist.

Long-Period Fiber Grating Sensors

Compared with normal short-period FBG whose grating period are usually comparable to the optical wavelength, the long-period fiber grating (LPFG) has much longer modulated refractive index period which is normally greater than 100 μm. Generally speaking, there are two methods widely used to fabricate the LPFG in a Ge-doped fiber optics: using a phase amplitude mask or using a point to point fabrication method. For the first method, the optical fiber is scanned by a UV beam through a phase amplitude mask which has a periodical array of windows with a designed width. For the point to point fabrication technique, the UV beam exposes the fiber through a small slit inducing a refractive index change in the illuminated area. The fiber then moves along its z-axis forming gratings with the period equals to Λ. Compared with normal FBGs, the fabrication process for a LPGF is relatively cheaper and simpler.

The LPGF is capable to couple light between forward-propagating core mode and forward-propagating cladding mode, causing multiple attenuation resonance peaks during the transmission. LPFG was firstly designed as a band rejection filter, later, its application has been expanded to EDFA gain-flattening filters, WDM isolation filters, high extinction ratio polarizers, mode converters, temperature and strain sensors, refractive-index sensors, and sensing modulators [53-67].

For a LPFG, the light is coupled from the core mode to cladding modes that supported by the cladding-external medium waveguide structure. The coupling condition meets the following resonance requirement:

$$\frac{2\pi}{\Lambda} = \frac{2\pi}{\lambda}\left(n_{eco} - n_{ecla}^{i}\right) \qquad (1-5)$$

where n_{eco} and n_{ecla}^{i} are the effective index of the fundamental core mode and the ith cladding mode, λ is the resonance wavelength of the LPFG, and Λ is the period of the grating. From the formula, it is obvious that the resonance wavelength highly depends on the effective refractive index of the core and cladding modes. So, any environmental perturbations that induce the effective refractive index change, either by thermal, mechanical, optical, or any other methods, the LPFG may capture it sensitively through the resonance wavelength shift.

Similar as in fiber Bragg gratings, the wavelength shift of resonant peaks in the LPFG resulting from temperature, strain, and external refractive index changes can be given as the following equation:

$$\Delta\lambda_{res} = \left(\frac{d\lambda_{res}}{dT}\right)\Delta T + \left(\frac{d\lambda_{res}}{dS}\right)\Delta S + \left(\frac{d\lambda_{res}}{dn_{sur}}\right)\Delta n_{sur} \qquad (1-6)$$

where $\left(\frac{d\lambda_{res}}{dT}\right)$, $\left(\frac{d\lambda_{res}}{dS}\right)$, and $\left(\frac{d\lambda_{res}}{dn_{sur}}\right)$ are the temperature, strain, and surrounding refractive index sensitivity of the resonant wavelength. LPFGs are important sensing elements in sensor applications and great filters in telecommunication area.

1.2.1.3 Distributed Fiber Optic Sensors

All the FOSs we covered above are single point sensor or quasi-distributed sensors, which means data are only available at the locations of gratings or structures. For the past two decades, distributed optical fiber sensors (DOFS) based on scattered lights generated in optical fibers including Raman, Rayleigh, and Brillouin scattering have involved extensive attention and efforts in researching and development for many sensing applications. An ideal DOFS should provide environmental parameters like temperature, strain, vibration, or other information at any point along the optical fiber [68]. Despite all the advantages, when compared with other fiber optic sensors like FBG, the distributed fiber optic sensors usually come with a price: relatively low spatial resolution, slow measurement speed, limited sensing range, high system complexity, and high cost.

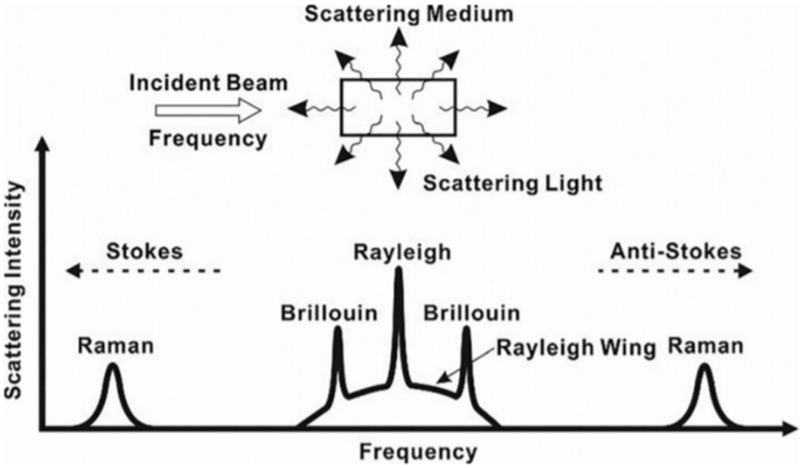

Figure 6 A typical spontaneous light scattering scatrum.

The basic sensing mechanism of DOFS is when an electromagnetic wave injected into an optical fiber, the propagation of the light will be modified by various mechanisms in the form of Rayleigh, Raman, and Brillouin scattering [68]. In general, when an incident beam illuminates a scattering medium, it will generate scattering signals in all directions. And the frequency spectrum of the scattering light, as shown in Fig. 6, contains Rayleigh, Raman, and Brillouin scattering. Among them, the central peak at the incident light frequency is Rayleigh scattering, also known as the elastic scattering, since no frequency shift induced during the scattering process. The scattering peaks next to the Rayleigh scattering is Brillouin scattering, which is induced from the light interaction with propagating acoustic phonons. While Raman scattering is generated from molecular vibrations. Brillouin and Raman scattering are considered as inelastic scattering, since there is a frequency shift from the incident light frequency. Usually, scattering shifted toward lower frequency is called Stokes, while for the opposite direction is called Anti-Stokes. These scattering signals may be altered by external perturbations like temperature, strain, and vibration. Through photodetectors, these changes may be captured and analyzed, and finally achieving the sensing purpose [69].

Optical Time Domain Refractometer (OTDR) Based on Rayleigh Backscattering

One of the most efficient and widely used DOFS is optical time domain refractometer (OTDR).

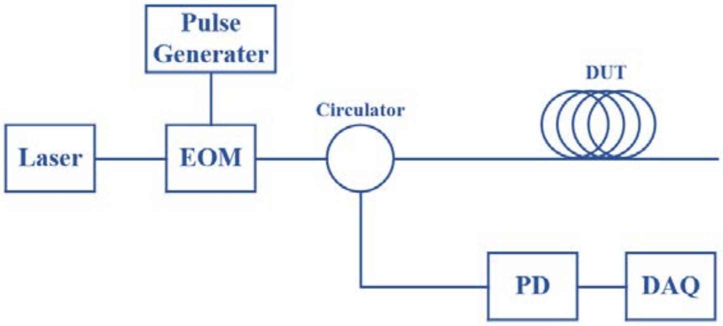

Figure 7 The scheme of a standard OTDR. EOM: electro-optic modulator; PD: photodiode; DAQ: data acquisition device; DUT: device under test.

As shown in Fig. 7, in general, an OTDR contains a pulsed light source, a photodetector, and an accurate synchronizing circuit. When the laser source shots a light pulse at a specific wavelength, the light pulse travels along the optical fiber and in the meanwhile generates Rayleigh scattering signals in random directions due to microscopic particles in the optical fiber. Part of the scattered light signals travels back (known as backscattering) through the fiber until reaching the photodetector in the OTDR. The backscattered light carries information like intensity and return time, which can be used to determine what is happening along the fiber sensor based on the distribution of optical return loss.

For a given OTDR system, the distance along the optical fiber and its spatial resolution or the accuracy is given as the following equations:

$$z = \frac{ct}{2n_{eff}} = \frac{v_g t}{2} \qquad (1-7)$$

$$\Delta z = \frac{\tau c}{2n_{eff}} = \frac{v_g \tau}{2} \qquad (1-8)$$

where c is the speed of light in free space, t is the backscattered detection time, τ is the pulse width of the laser source, v_g is the group velocity in the fiber, and n_{eff} is the effective refractive index of the fiber. For commercial OTDRs, the spatial resolution is usually around 1 m.

Optical Frequency Domain Reflectometer (OFDR)

Other than OTDR, distributed fiber sensors may also work in the frequency domain named as optical frequency domain reflectometer (OFDR) [70, 71]. Compared with OTDRs whose spatial resolution are usually within the meter level, OFDR offers much higher resolution combined with a large dynamic range. Rayleigh based OFDR (R-OFDR) uses a tunable laser to scan a frequency range of ΔF and through Fourier transformation produces a spatial resolution of:

$$\Delta z = \frac{c}{2n_{eff}\Delta \mathrm{F}} \qquad (1-9)$$

The basic measurement principle of a R-OFDR system is shown in Fig. 8. The light from a swept tunable laser source (TLS) is split by a 2x2 fiber optic coupler into two arms of a measurement interferometer: the reference arm and the measurement arm which contains the device under test (DUT). There is an optical circulator in the measurement arm with the connected device under test (DUT) as an input port and the output is the reflected light from the test fiber. The output light is then combined with the reference signal and passes through a polarization beam splitter (PBS). The polarization controller (PC) in the reference arm controls the refence light so that it can be evenly split at two ends of the PBS. The interference pattern of the combined signal is recorded as the laser sweeping through a certain wavelength range. A Fourier transform of these detected signals represents the amplitude and phase of the backscattered light which is related to the delay along the fiber. And a trigger interferometer with an already know delay is used to compensate the nonlinearities in the laser tuning.

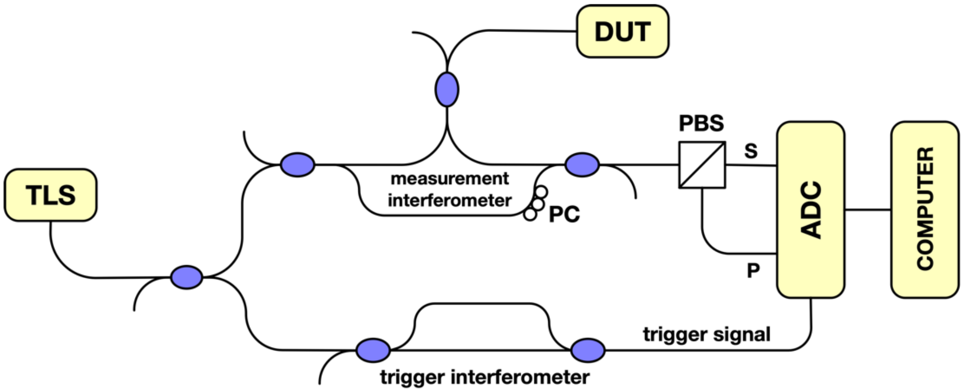

Figure 8 The basic optical network of an OFDR system. TLS: tunable laser source, DUT: device under test, PBS: polarized beam splitter, PC: polarization controller.

To measure the local strain or temperature change in the test fiber, a Rayleigh backscatter signal is first measured and stored at the ambient state to serve as a reference. Then, the scattered signal is measured again after strain or temperature applied to the optical fiber. These two data sets are cross correlated to generate a backscatter profile as a function of length with an increment of Δz, known as the Gauge Length which defines the spectral resolution and the signal-to-noise ratio of the measurement. When a certain section of the backscatter profile is selected, a shift in the spectrum of this piece of data in response to strain ε or temperature T is analogous to a shift in the resonance wavelength Δλ or the spectral shift Δν of a Bragg grating:

$$\frac{\Delta\lambda}{\lambda} = -\frac{\Delta\nu}{\nu} = K_T\Delta T + K_\varepsilon\varepsilon \qquad (1-10)$$

where λ and ν are the mean optical wavelength and frequency, and K_T and K_ε are the temperature and strain calibration constants of the optical fiber, respectively. The values for K_T and K_ε are largely determined by the dopant species and concentration in the core of the fiber, but also has a lesser relationship to the composition of the cladding and coating. If the strain is negligible, the temperature change be written as:

$$\Delta T = -\frac{\bar{\lambda}}{cK_T}\Delta\nu \qquad (1-11)$$

where $\bar{\lambda}$ is the center wavelength of the scan and c is the speed of light. Similarly, in the absence of a temperature change, the strain can be written as:

$$\varepsilon = -\frac{\bar{\lambda}}{cK_\varepsilon}\Delta\nu \qquad (1-12)$$

Thus, the distributed temperature and strain curves are merely rescaled copies of the spectral shift distribution.

Optical Backscattered Reflectometer

Based on Rayleigh optical frequency domain reflectometry, the optical backscatter reflectometer (OBR) uses swept-wavelength interferometry (SWI) to measure the Rayleigh backscatter as a function of length in the optical fiber with ultra-high spatial resolution.

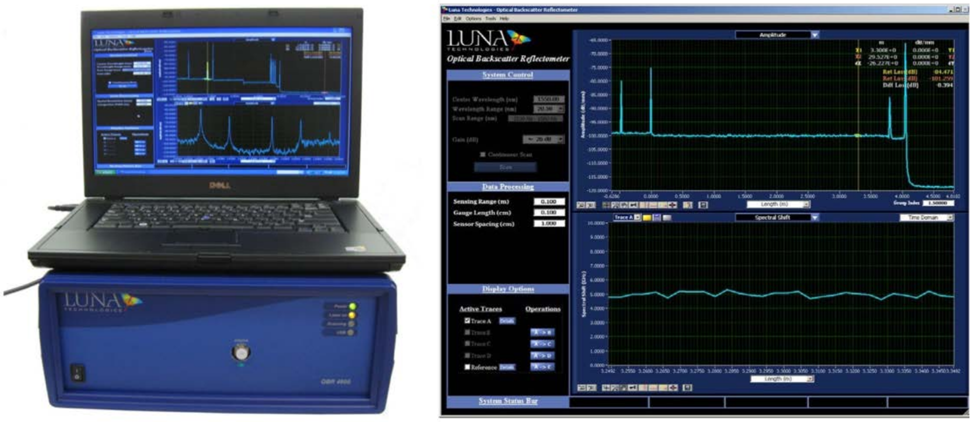

Figure 9 LUNA OBR 4600.

The Rayleigh backscattered signal from an individual optical fiber is caused by random fluctuations in the index profile along the fiber length. For a given optical fiber, the Rayleigh backscatter is a unique, random, but static property. The physical length and refraction index of the fiber are intrinsically sensitive to temperature and strain, and to a lesser extent of pressure, humidity (if the fiber coating is hydroscopic), electromagnetic fields, etc. When these environmental parameters alter, there is a change in the local period of the Rayleigh scatter which causes temporal and spectral shift in the locally reflected spectrum. The OBR measures this shift and turns a standard telecom-grade single-mode optical fiber into a robust and accurate distributed temperature/strain sensor with millimeter-range spatial resolution over tens of hundreds of meters of fiber.

1.2.2 Embedded Fiber Optics in Metal Components

The so-called “fourth industrial revolution” involves the integration of sensing devices into the variety of tools, materials and machines, that to enable accurate, real-time monitoring of relevant and important systems and processes. In previous studies, it can easily embed sensors in composite materials during the manufacturing process, that they have successfully used sensing devices to monitor innovative composite bridge structures [72]. The main attraction of using embedded fiber optic sensor systems is that they significantly reduce the number of front-end electronics required and are lightweight and non-intrusive. Embedded system allows the operator to get rid of the current time-based maintenance procedures and to make timely preventive and planned maintenance decisions. In many cases, cheaper conventional sensors, such as piezoelectric accelerometers, strain gauges or thermocouples, can be used if the monitoring conditions are appropriate. Although this is not the case in many professional fields, the optical fiber method is preferred [72, 73]. However, for metals, how to effectively combine sensors is a real challenge: the manufacturing process is operated at high temperature, and the application usually includes harsh environment, while the traditional sensor is not easy to bear. In most current applications, FOS is usually adhered to metal surfaces, just as it is usually used to monitor bridges and steel bars but the long-term degradation of adhesives and glues can affect the measured values, and then often lead to unexpected errors, such as the reduction of strain transfer due to reduced adhesion. Embedding FOS into metal structures can avoid these problems (and the resulting errors), so the challenge of creating a satisfactory, repeatable method to achieve this must be addressed [72].

Moreover, fiber optical sensor is composed of modified optical fiber. The core of the fiber is slightly surrounded by a concentric core (1%). Optical fibers are usually made of silica with refractive index modified dopants such as GeO_2. A protective coating of cushioning material (such as acrylate) is used to reduce light loss due to micro-bending that occurs when fibers are pressed against rough surfaces and to provide protection to the fragile optical fiber core and cladding. The diameters of core and cladding for a single mode fiber are 9 mm and 125 mm respectively. The metal layer must be applied to the fiber as embedding an FOS into metallic materials. The coating can mechanically protect the fibers from the effects of high temperature and mechanical loads during the embedding process. Moreover, they affect the binding with metals and may be affected by sliding or delamination [72, 74]. The first solution to embedding FOS into metal was based on deposition technology. In this case, the total diameter of the fiber required to withstand the embedding process is often as large as 2 mm, which is significantly larger than that of a typical communication-based fiber (cladding ~125 µm diameter).

Fiber optic sensors are used to measure changes in strain, temperature, magnetic and electric fields, acoustic and chemical concentrations, which are obtained by measuring induced changes in intensity, phase, wavelength, polarization, time domain characteristics and modal content caused by these external phenomena. These sensors may be broadly classified as external devices, which guide light out of the fiber, interact with the environment, and then re-enter the fiber, and internal devices, which transmit light throughout the length of the fiber. Intrinsic sensors have the advantage of being simple and may be low-key for embedded applications [75].

Since Heyman's introduction of embedded fiber optic sensors for materials in 1979, embedded fiber optic sensors have been used to directly measure internal strain, temperature, and chemical concentrations, as well as to measure the condition of the surrounding medium. Recently, multi-parameter, quasi-distributed and continuously distributed sensor devices have been reported that utilize special waveguide characteristics or signal processing techniques. The biggest advantage of optical fiber is its small size and relatively light weight. It can be configured to respond to different environmental impacts. It has high sensitivity, linearity and dynamic range. In addition, due to its own all-dielectric characteristics, it is not sensitive to interference. Nowadays, some large equipment, such as aircraft, in order to reduce their own weight, are made of composite materials that have the advantages of high strength, high stiffness, light weight and so on. However, during use, these factors such as impact can cause internal damage that is invisible to the surface. It may result of aircraft accidents and limit the use of composites and structures in the aerospace sector. Therefore, it is essential to inspect composite structures using structural health monitoring systems. The reason for building a structural monitoring system is that it can diagnose the health of the composite structure and also improve the reliability of the system's composite structure [76]. Combining sensors and composite structures is the most important step in building a structural monitoring system. Researchers have attempted to integrate various sensors, such as piezoelectric ceramics, metal strain gauges, and fiber optic sensors, into the composite structure. Studies have shown that fiber optic sensors are widely favored by researchers due to their inherent resistance to electromagnetic interference and ground loops, distributed and multi-channel operation, and high sensitivity. So, optical fiber sensors are frequently embedded in composite structures as a sensor network. Now structural health monitoring systems with optical fiber sensors are becoming a frontline research area of smart materials and structures [76].

Ultrasonic welding and vacuum brazing are commonly used solutions for embedded optical fibers. However, each solution still has drawbacks, such as the low temperature of the ultrasonic welding process limits the application of sensors [72] and the vacuum brazing process is relatively more complex, costly, and there are requirements to meet the vacuum chamber. For this reason, the technique of laser melting plays an important role as a new embedded fiber solution. It has been shown that the process of establishing a protective coating with a total diameter of up to 350 μm allows precise thermal control in real time, and is not limited by the properties of different materials. Furthermore, the solution does not require the creation of an additional vacuum gas chamber, providing sufficient operating space for production. However, the LMD (laser metal deposition) process requires the use of high-power lasers to generate the necessary level of heating, making the technology very expensive [72, 74, 77].

Ultrasonic Consolidation (UC) process is also used to embedding optical fibers in an aluminum matrix. In contrast to casting and metal deposition, the ultrasonic cementation (UC) process is a fast, low-cost, and scalable embedding process technology that can be set up to automatically embed large free-form metal structures with fibrous metal belts. The UC process differs slightly from standard ultrasonic welding in that "surface effects" and "volume effects" cause bonding during the cementation process. The "surface effect" refers to the effect of vibration causing interfacial friction between two mating surfaces, which is the bonding mechanism for many of the fundamentals in ultrasonic welding. The volumetric effect refers to the effect of vibration causing internal stress and plastic deformation of the metal structure, which usually occurs at or below the weld interface. The volume effect is more fully utilized in the UC process than in the ultrasonic welding process. In the ultrasonic welding process, the shape of the weld is mainly maintained by the shape of the sonic electrode and the anvil, which reduces the metal displacement in the weld area. In the UC process, this is mainly accomplished by surface effects, i.e., surface friction and adhesion forces cause metallurgical bonding on the mating surface of the base foil [73].

Nowadays, 3D printing or additive manufacturing (AM) is an increasingly popular manufacturing method due to its nature in shrinking product development cycle time and increasing product complexity. The object is created by laying down successive layers of materials based on a single computer-generated model file. It shows unbeatable advantages that conventional fabrication methods can hardly or never achieve, like building products with complex shapes and different materials. Bypassing the needs of traditional machining process, such as welding, milling, and grinding; 3D printing is an affordable and high-speed way for prototyping.

Additive manufacturing allows full access to any point of interest during the fabrication of the object, which offers great opportunity for embedding sensors and components into the printed part to form a smart functional component. Recently, a number of researchers have begun to explore the prospect of sensor fusion for additive manufacturing. Through this paradigm, sensors are embedded into 3D printed parts in a layer-by-layer manufacturing process in order to produce "smart" functional products. By introducing embedded sensors into this part, it is possible to validate and improve the design at the prototyping stage, gaining information on the performance and structural integrity of the functional part over the life of the part. This information is important for many industries, particularly in the energy and aerospace sectors. As mentioned earlier, among the existing sensor technologies, fiber optic-based sensors have been considered as the best choice for sensor fusion AM of smart components. Continuous research has shown that the high-temperature elasticity of optical fibers, as well as their inherent corrosion resistance, results in a higher reliability of the material during thermal deposition or in harsh operating environments [78].

Embedding optical fibers into 3D printed parts has long been attempted, but there are still some technical issues that need to be addressed in the realization of fiber optic smart parts. The embedding of fiber optic sensors has been demonstrated using 3D printing processes with substrates ranging from composites [79], to plastics [80, 81], to un-sintered metal [78, 82-84]. In some cases, the incorporation of these sensors requires that the available temperature range of the sensor-fused smart components be kept below 350°C [79-81]. When using additive metal-based processes for production, the smart components for high-temperature processes have to be taken into account as well, which is also a challenge for embedded fiber optic technology. In addition, the laser, electron beam or sintering furnace used as a molten additive material during the process needs to be continuously manufactured at temperatures within the melting zone of the resulting metal. In order to avoid the effects of high temperatures on the material, the researchers used metal sheaths up to 700 meters thick to protect the optical fibers. Typically, the metal sheath is deposited on the fiber through a low-temperature process, such as electroless plating, electroplating [85] or a mixture of electroplating and magnetron sputtering [86]. Subsequently, the metal-coated fibers are embedded in metal parts using various AM process ranging from low-temperature ultrasonic consolidation [87], to high-temperature brazing at ~800 °C [88], to extreme high-temperature processes that melt metal powders at > 1500 °C [86]. Point fiber sensors such as fiber Bragg gratings (FBG) and Fabry-Perot cavities [77, 84-88] have been successfully embedded in metal parts using 3D printing. Despite these successes, operational temperatures for fiber sensor-embedded smart components produced using all-metal AM processes have also been limited to less than 400 °C [78]. This limitation is thought to be due to the large difference in coefficient of thermal expansion (CTE) between the metal coating and the silica fiber, which leads to delamination between the two.

1.3 Outline

Following this introduction, Chapter 1 introduces the background knowledge about four main types of fiber optic sensors, including fiber interferometer, fiber gratings, optical time domain reflectometers (OTDR), and optical frequency domain reflectometers (OFDR). It also covers previous studies in embedding sensors and functional structures, especially optical fiber sensors, to fabricate smart components.

Chapter 2 gives theories and simulation analysis about the AM process, covering both thermal analysis and mechanical analysis. It also introduces the embedded sensors and components in AM applications. Moreover, we discussed the detailed experimental procedurals to embed optical fiber sensors in AM applications. Starts from sample preparation, then Nickel electroplating, and finally the embedding process. We also investigate the both simulation analysis and experimental results of the sensor characterization test, including the temperature measurements and strain measurements.

Chapter 3 shows some more practical applications with embedded optical fiber sensors by extending this sensor embedding technique into more complex situations: AM applications with curved surface. This chapter introduces the motivation, detailed experimental steps to embed pre-shaped optical fiber sensors into 3D additive manufacturing applications, and a standard static test to check the sensing capability of the embedded fiber sensor.

Chapter 4 gives another example of embedded fiber optic sensor used in laser processing application to monitor the real-time strain distribution in the laser peening process. This chapter also introduces an advanced laser processing technique to enhance micro-fabrication applications with the help of a spatial light modulator.

2.0 Embedding Techniques for Fiber Optic Sensors

Embedding of fibers in metal structures mainly depends on the types of the fiber and matrix. Conventional discontinuous and continuous fibers are embedded in composites by casting, diffusion bonding, metal spray, or electrodeposition techniques. These methods have some limitations such as elevated processing temperatures, high cost of tooling, and limitations on geometrical complexity. In this chapter, we report both the theoretical simulation of the stresses induced during deposition along with experimental measurements of those stresses in Inconel 718 metal alloy components fabricated with the LENS additive manufacturing process. Residual strains measured by the fiber sensors quantitatively agreed with the stress simulations. This information can be useful for reducing or mitigating residual strain during or following the manufacturing process. It can also be used to perform continuous monitoring of 3D print parts against corrosion and metal frailty in service. In addition, the technique to embedding optical fiber sensors into curved surface, like a 3D printed Ti-6Al-4V turbine blade, is discussed. Further load test with this sensor embedded turbine blade was measured and analyzed.

2.1 An Analytical Model for the Thermos-Mechanical Process

A detailed thermos-mechanical process simulation was developed to predict the temperature and residual strains in the metal parts produced by the LENS process. The key governing equations involved in the sequentially coupled thermal and mechanical analysis are briefly discussed below. The equations were implemented using ANSYS finite element analysis (FEM) package (ANSYS v17.2).

2.1.1 Thermal Analysis

Consider a body $\boldsymbol{V}$ in the Lagrangian description for the thermal analysis, where a material point is denoted by $\boldsymbol{r}(\boldsymbol{r} \in \mathbf{V})$ as the reference. Given the thermal energy balance at time t, the governing equation can be written as follows:

$$\rho C_p \frac{dT(\boldsymbol{r},t)}{dt} = -\nabla \cdot \boldsymbol{q}(\boldsymbol{r},t) + Q(\boldsymbol{r},t), \boldsymbol{r} \in \boldsymbol{V} \qquad (2-1)$$

where ρ is the mass density of the metal material; C_p is the specific heat capacity; T is the temperature; $\boldsymbol{q}$ is the thermal flux vector. Q is the internal heat source, which is the key quantity in the thermal process modeling, since the intensive heat input is the cause of the residual strains in the AM processes. To model the heat source, a double ellipsoid model is employed, which has been shown to be accurate for modeling powder-fed laser fusion processes. Details of the double ellipsoid model can be found in [89].

Thermal boundary conditions are necessary for solving the governing equations. Three categories of boundary conditions are involved in this thermal analysis:

(1) Dirichlet boundary conditions:

$$T = \bar{T}, \qquad \boldsymbol{r} \in S_D^T \qquad (2-2)$$

where the temperature on the boundary S_D^T is fixed as a constant value $\bar{T}$. This boundary condition was implemented on four corners where the Inconel substrate was bolted to the base of the LENS chamber.

(2) Neumann boundary conditions:

$$-k\nabla T \cdot \boldsymbol{n} = \bar{q},\ \boldsymbol{r} \in S_N^T \tag{2-3}$$

where k is the coefficient of the thermal conductivity and ∇T is the temperature change. This equation indicates that the thermal flux along the normal vector $\boldsymbol{n}$ to the boundary S_N^T is prescribed by a constant $\bar{q}$. This boundary condition is applied to the laser-scanned surface of the Inconel substrate where metal powders are deposited, laser melted, and consolidated.

(3) Robin boundary conditions:

$$-k\nabla T \cdot \boldsymbol{n} = h(T - T_a), \boldsymbol{r} \in S_R^T \tag{2-4}$$

where h is the coefficient of convection and T_a denotes the ambient temperature. The heat convection related to the temperature change is applied to the surface S_R^T, which describes convective thermal heat flow from the hot substrate surface to the argon gas in the LENS chamber.

Besides the boundary conditions, the initial condition has to be considered since the governing equation contains some time-dependent terms. The following thermal initial condition was used in this paper:

$$T(\boldsymbol{r}, 0) = T_0(\boldsymbol{r}, 0), \boldsymbol{r} \in \mathbf{V} \tag{2-5}$$

where T_0 is the initial temperature prior to the laser deposition process. The temperature history determined by the thermal analysis is applied to the model as a thermal load and boundary values in the mechanical analysis. Using these boundary conditions, full-scale thermal analysis was carried out for the entire Inconel substrate during the LENS deposition.

2.1.2 Mechanical Analysis

Quasi-static mechanical analysis is performed to model the residual strain in the AM metal parts after the Inconel substrate cooled to room temperature. The governing equation of the quasi-static mechanical analysis is written as:

$$\nabla \cdot \boldsymbol{\sigma} + \rho \boldsymbol{f} = \mathbf{0}, \boldsymbol{r} \in \mathbf{V} \tag{2-6}$$

where $\boldsymbol{\sigma}$ is the stress tensor, and $\boldsymbol{f}$ is the body force per unit volume. The Dirichlet boundary condition of the displacement field is then applied to the model:

$$\boldsymbol{u} = \bar{\mathbf{u}}, \boldsymbol{r} \in S_D^M \tag{2-7}$$

where $\bar{\mathbf{u}}$ is constant displacement on S_D^M. Usually, this condition indicates a fixed boundary constraint in the AM process. The stress tensor $\boldsymbol{\sigma}$ is calculated based on the material constitutive model as follows:

$$\boldsymbol{\sigma} = \boldsymbol{C}\boldsymbol{\varepsilon}_e \tag{2-8}$$

$$\boldsymbol{\varepsilon}_e = \boldsymbol{\varepsilon} - \boldsymbol{\varepsilon}_p - \boldsymbol{\varepsilon_t} \tag{2-9}$$

where $\boldsymbol{C}$ is the fourth-order elastic tensor; $\boldsymbol{\varepsilon}$, $\boldsymbol{\varepsilon}_e$, $\boldsymbol{\varepsilon}_p$and $\boldsymbol{\varepsilon_t}$ are the total, elastic, plastic and thermal strains, respectively.

The elastoplastic model has been widely used for mechanical modeling of powder-feed laser 3D-printing processes. Our process model has been fully validated by other thermal and mechanical experiments [89]. In comparison with thermal analysis, modeling of mechanical properties is more complex and more computationally intensive. Key parameters corresponding to thermal and mechanical properties of the material, such as thermal conductivity coefficient, CTE, and elastic modulus, are temperature dependent in the wide temperature range that the processed material experiences. This leads to highly nonlinear thermomechanical behavior that requires much care in order to obtain accurate simulation results. In this work, the element mesh of the model was made sufficiently small to capture the extremely thermal gradient at the laser focal spot. Because the substrate was much larger than the focused laser spot, a large number of elements are needed in the simulation, which requires high computational cost for a full-scale simulation over the entire substrate. Additionally, because a point heat source was used to model the laser focal spot along the laser scanning path, thousands of load steps were employed to ensure the accuracy and convergence of the numerical simulation. As a result, it was determined to be too time-consuming to simulate the deposition process for the entire metal part. Finally, the metal deposited at each location was sintered by repeated micro-welding or multiple applications of laser energy. This ensured that the stress and deformation at any one point was affected locally by any neighboring deposits. Therefore, it was deemed to be more reasonable to simulate a small representative volume of the entire part rather than simulate the entire substrate to obtain the residual strains. Given these limitations, a mechanical analysis was carried out on a small strip of 3D printed area 28.0 (L) × 3.0 (W) × 0.6 (D) mm^3 in dimension.

2.2 Metalizing Fiber Optic Sensors

To practically embed optical fiber sensors into additive manufacturing applications, the following three main steps should be considered in designing the experiment: prepare samples including both optical fibers and metal substrates, protect optical fibers with metal coatings through electroplating method, and finally embed the fiber sensors into the substrate using 3D printing technique.

2.2.1 Sample Preparation

The optical fibers chosen for serving as the embedded smart sensors are copper-coated single-mode silica fiber (Cu1300 from IVG Fiber^{TM}, as shown in Fig. 10a).

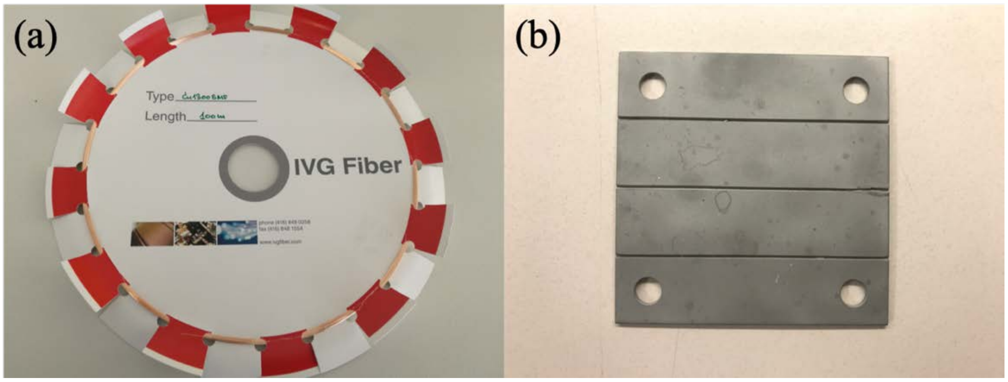

Figure 10 (a) Cu1300 single-mode optical fiber and (b) IN718 plate after machining.

The fiber has a 125 µm cladding diameter protected by 20 µm thick copper layer deposited using a sputtering process. The metalized fibers can survive at a temperature of 600 °C for less than 60 seconds. They are stable for much longer periods of time at 450 °C. Optical fibers were first cleaned by dipping in acetone for 30 minutes to remove any organic residues on the copper coating. They were then rinsed in methanol and DI water, and ready for the further treatment.

A 100 × 100 × 2 mm^3 Inconel alloy (IN718) plate (Rolled Alloys, Inc.) was used as the substrate for fiber sensor embedding. The IN718 plate was first milled to form three grooves with dimensions (L×W×H) of 100 × 2 × 1.25 mm^3, as shown in Fig. 10b. The surface of the substrate was then sandblasted to improve bonding for AM deposited metal. After the surface preparation, the plate-surface was covered by masking tapes leaving the three trenches exposed.

2.2.2 Nickel Electroplating

Even though the Cu1300 optical fiber can withstand much higher temperature than normal single-mode fibers, the fiber embedding processing was performed using a LENS system (OPTOMEC LENS450), where the local temperature around the laser focus in the LENS process may easily exceed 1500 °C. So, a further protective metal layers were required for the copper-coated optical fiber.

2.2.2.1 Nickel Sulfamate Bath

After thoroughly cleaned, the Cu1300 fibers were taped onto a plastic frame to keep them straight during electroplating, as shown in Fig. 11.

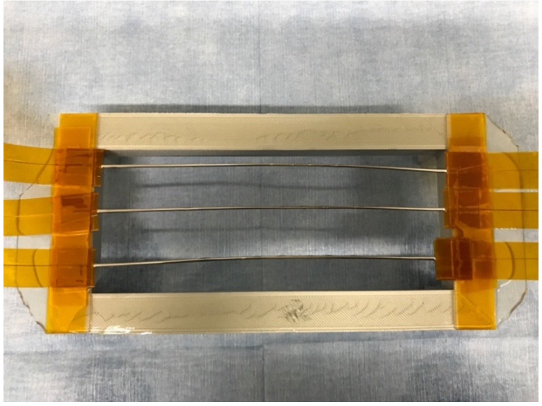

Figure 11 Three pieces of Cu1300 optical fiber are electroplated with Nickel through Nickel sulfamate bath.

The optical fibers together with the plastic frame were then transferred to a nickel sulfamate bath for electroplating. A detailed record of the electroplating conditions is given in Table 1. The optical fiber was electroplated for 24 hours to form a 350 µm thick nickel layer on top of the copper coating.

Table 1 The Parameters for Nickel Electroplating

<table>
<tr><th colspan="3">Electroplating Bath Solution</th></tr>
<tr><th>Chemical name</th><th>Formula</th><th>Bath concentration</th></tr>
<tr><td>Nickel sulfamate</td><td>$Ni(SO_3NH_2)_2$</td><td>280-320 g/l</td></tr>
<tr><td>Nickel chloride</td><td>$NiCl_2\cdot 6H_2O$</td><td>40-60 g/l</td></tr>
<tr><td>Boric acid</td><td>H_3BO_3</td><td>20-44 g/l</td></tr>
<tr><th colspan="3">Electroplating Conditions</th></tr>
<tr><th>Temperature</th><td colspan="2">45 °C</td></tr>
<tr><th>pH</th><td colspan="2">3.5-4.5</td></tr>
<tr><th>Cathode current density</th><td colspan="2">3.858 A/dm^2</td></tr>
<tr><th>Deposition rate</th><td colspan="2">12.5 µm/hour</td></tr>
</table>

2.2.2.2 Residual Stress Induced in Electroplating Process

In practice, even though the optical fibers were well fixed onto the plastic frame to keep straight, it would usually suffer from significantly bend after electroplating, as shown in Fig. 12a. The deformation of the fiber sensor results poor fitting to the pre-machined grooves on the substrate, which later affect the embedding process with AM.

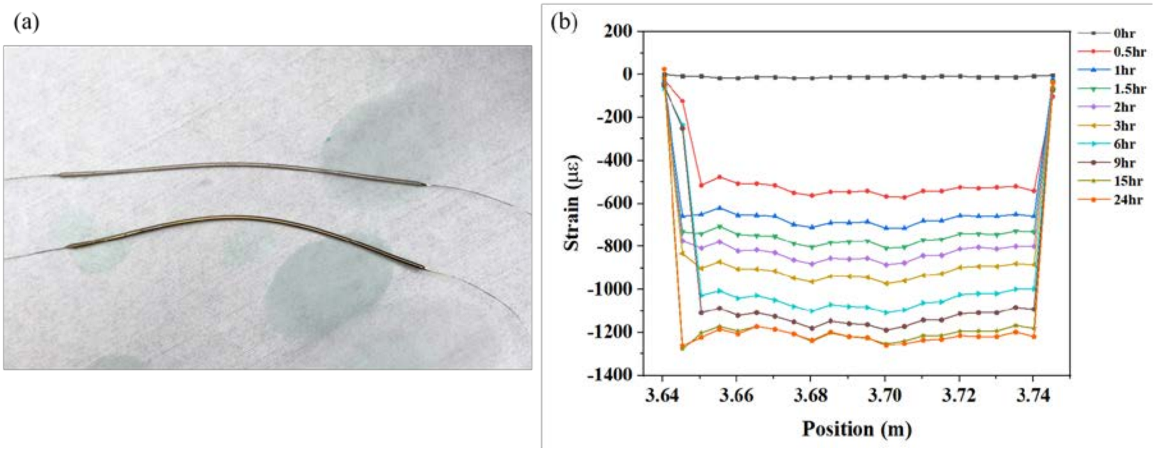

Figure 12. (a) The Nickel electroplated fibers were buckled during electroplating process. Upper fiber: using revised electroplating recipe; Bottom fiber: using default Nickel Sulfamate Electroplating recipe. (b) The distributed residual strain along optical fiber during the electroplating process with the default recipe.

The deformation was caused by the residual stress accumulated in the Nickel electroplating process. To capture the residual strain, we fused the optical fiber with single-mode fibers (SMF-28e) through fusion splicer, and then connected the whole piece to the OBR. The strain distribution along the optical fiber sensor was measured by OBR in real-time with 5 mm spatial resolution, the results are given in Fig. 12b. From the plot, it can be seen that the strain distribution along the Nickel electroplated fiber sensor shows a slight “U” shape with a relatively flat bottom line along the fiber axis. Since the strain value is negative, the residual strain is compressive strain. Moreover, the residual strain generally accumulated and increased as the electroplating process goes on. After

24-hour Nickel Sulfamate bathing, the average residual strain measured by OBR was maintained at around -1200 με.

Previous work [90] shows that certain electroplating parameters have great impact to the mechanical properties of the Nickel Sulfamate deposition. Chlorides or bromides are usually applied to the electroplating bath to accelerate the deposition rate and balance the internal stress, while too much Chlorides may induce compressive stress. In addition, increasing electroplating temperature and maintaining the pH value of the solution between 4.0 and 4.2 turn out to be efficient methods to reduce residual stress accumulated during the Nickel Sulfamate electroplating. The modified chemical composition and operating conditions of the Nickel Sulfamate electroplating are given in Table 2.

Table 2 The Revised Parameters for Nickel Electroplating

<table>
<tr><th colspan="3">Revised Electroplating Bath Solution</th></tr>
<tr><td>Chemical name</td><td>Formula</td><td>Bath concentration</td></tr>
<tr><td>Nickel sulfamate</td><td>$Ni(SO_3NH_2)_2$</td><td>315 g/l</td></tr>
<tr><td>Nickel chloride</td><td>$NiCl_2 \cdot 6H_2O$</td><td>0 g/l</td></tr>
<tr><td>Boric acid</td><td>H_3BO_3</td><td>45 g/l</td></tr>
<tr><th colspan="3">Electroplating Conditions</th></tr>
<tr><td colspan="2">Temperature</td><td>49 °C</td></tr>
<tr><td colspan="2">pH</td><td>4.2</td></tr>
<tr><td colspan="2">Cathode current density</td><td>3.858 A/dm^2</td></tr>
</table>

Another piece of Cu1300 optical fiber was Nickel electroplated using the revised Nickel Sulfamate bath concentration and conditions. The fiber sample was also connected to OBR similar as described in last section and was electroplated for 20 hours. The captured residual strain distribution was plotted and given in Fig. 13.

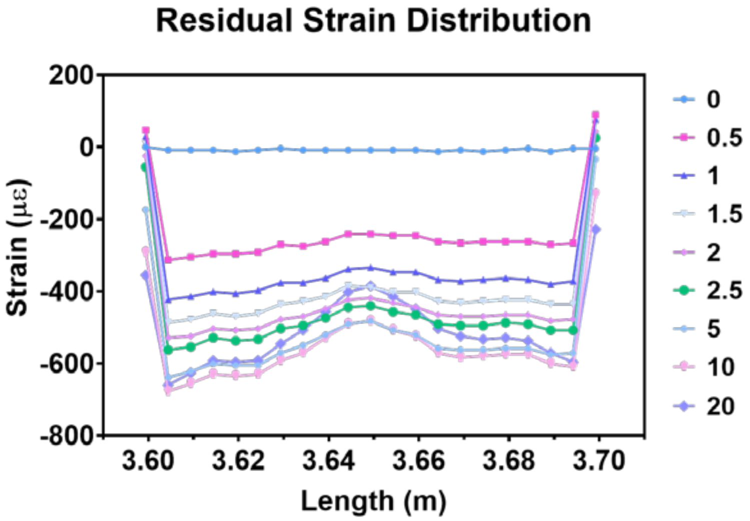

Figure 13 The residual strain distribution along the tested optical fiber during the Nickel electroplating process with modified Nickel Sulfamate bath concentration and conditions.

From the plot, it can be seen that the strain distribution along all the optical fiber was relatively uniform for the first 2 hours, as the strain curves are generally flat. Then, the center part of the electroplated optical fiber accumulated less compressive compared with other area, and the strain curves show a slight "W" shape along the fiber axis. Compared with the old Nickel electroplating concentration and conditions, in general, the residual strain generated during the electroplating with new recipe is much smaller, with less than 700 με compressive strain at maximum. To further analyze the residual strain induced in the Nickel electroplating process, the mean and median value of the measured strain distribution at each time period was subtracted from the collected data and plot as shown in Fig. 14.

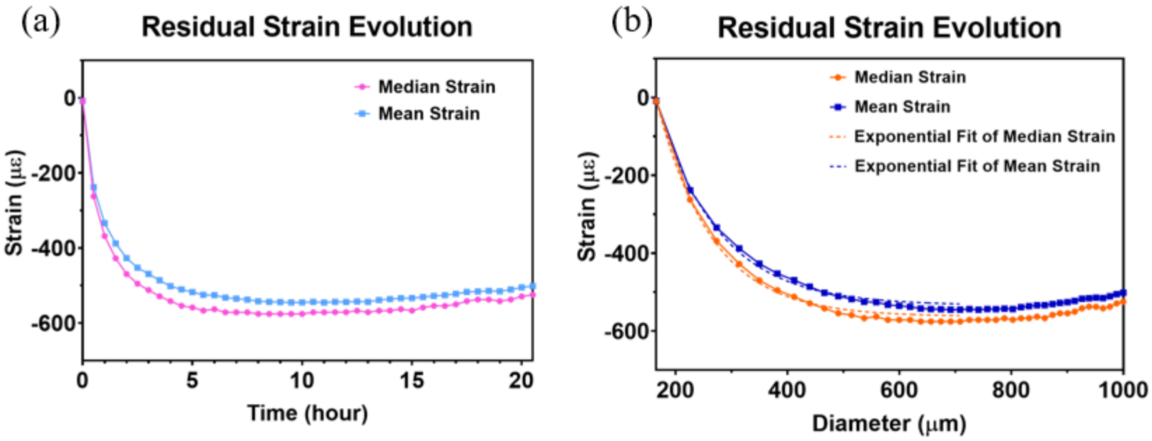

Figure 14 Residual strain evolution along optical fiber during the nickel electroplating process.

According to Faraday’s laws of electrolysis, the mass of the electroplated metal can be given as the following equation:

$$m = \frac{QM}{Fz} = \frac{ItM}{Fz} \tag{2-10}$$

where m is the mass of the substance liberated at an electrode in grams, Q is the total electric charge passed through the substance coulombs, $F = 96485.33289(59)\ C/mol$ is the Faraday constant, M is the molar mass of the substance in grams per mol, and z is the valency number of ions of the substance (electrons transferred per ion). In our case, the electroplated optical fiber can be considered as a cylinder, so based on the Faraday’s law, the theoretical real-time thickness of the electroplated Ni (or equivalently the diameter of the fiber sensor) can be calculated. The result is given in the following plot.

The fiber bending phenomenon is known as buckling, a mathematical instability that leads to failure mode. When a critical load is applied on the subject, buckling may occur. According to Euler formula, the critical Euler buckling stress is give as:

$$\sigma_{Euler} = \kappa \frac{\pi^2 E}{\left(\frac{L}{r}\right)^2} \qquad (2-11)$$

where E is the elastic modulus, L is the length of the component, r is the radius of gyration, and κ is a constant depending on the restrains of the two ends of the components, which has a large influence on the critical buckling load. According to the deformation of our fiber samples, the occurred buckling matches the condition in Fig. 15a.

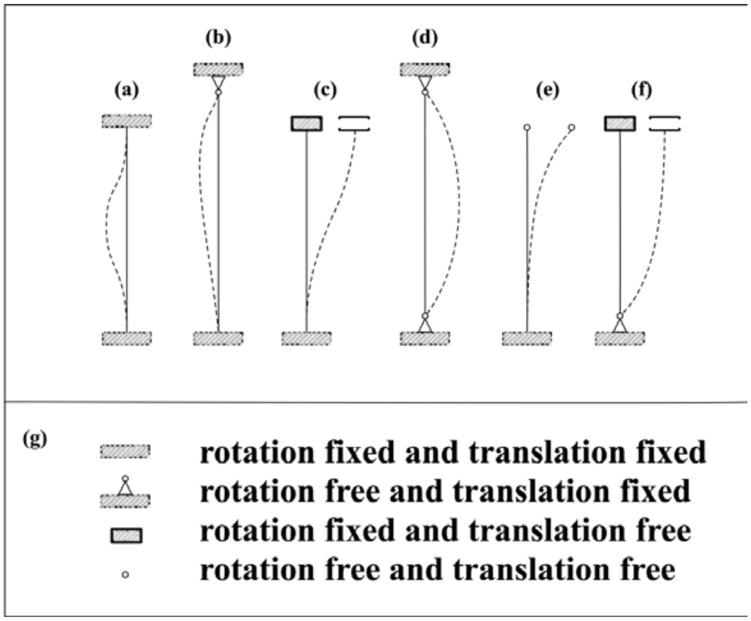

Figure 15 Different buckling models due the difference in boundary conditions.

2.3 Embedding Fiber Optic Sensors

2.3.1 Embedding Procedures

After electroplating, one metal-plated fiber (~865 μm in diameter) and one stainless-steel tube (SS316) (1060 μm outer diameter and 700 μm inner diameter) were placed side-by-side in each groove. Additional electroplating of the entire assembly was then carried out using the same parameters detailed in Table 2 for an additional 12 hours to fill the grooves and provide further protection against the extreme temperatures in the LENS process.

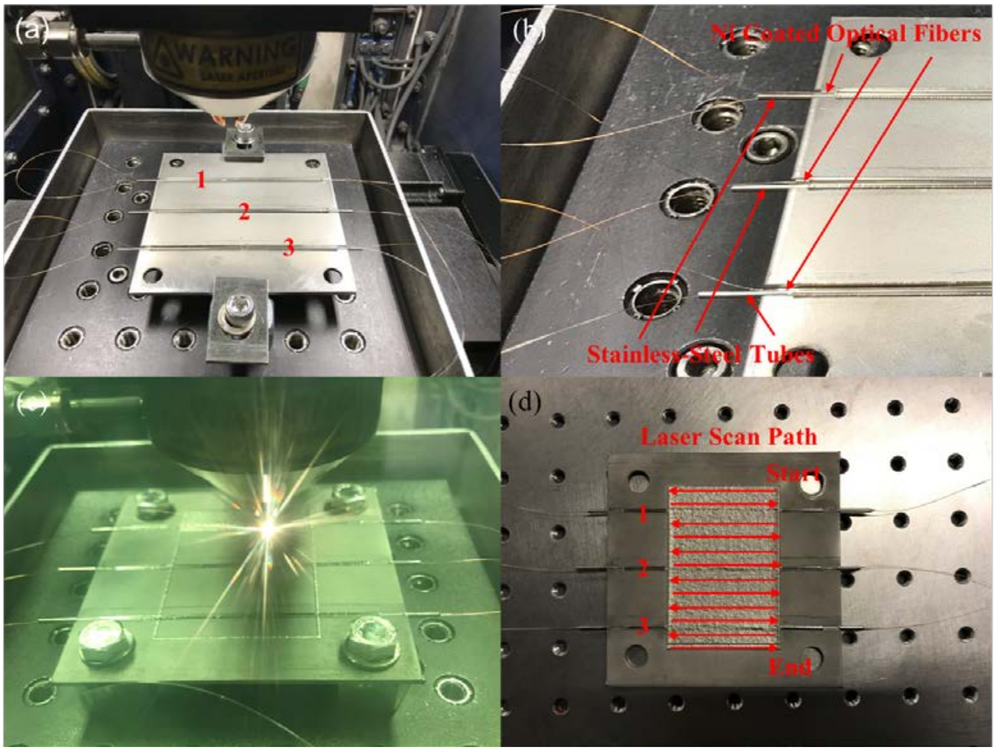

Figure 16 (a) Three sets of temperature and strain sensors were embedded into the pre-machined grooves through nickel electroplating method. (b) Zoomed-in figure of the Ni-coated optical fibers for strain measurement and the stainless-steel tube protected fibers for temperature monitoring. (c) The LENS depositing process. (d) An IN718 block was deposited onto the sample.

After the plating process, standard single-mode telecommunication fiber (Corning SMF-28e+) with polymer jacket removed was inserted into the stainless-steel tubes as shown in Fig. 16a, b. Both the copper/nickel coated fibers and the uncoated fibers were fusion-spliced into a single string for interrogation by an optical backscatter reflectometer (LUNA Innovations OBR4600). The fibers inserted in stainless steel tubes were not mechanically coupled to the substrate and would therefore be used to perform temperature measurements, while the electroplated fibers were well-coupled to the substrates and would be used to perform strain measurements. A measurement resolution of 5 mm was employed for either strain or temperature sensing. Compared with the size of the three-dimensional metal depositions, this spatial resolution is sufficiently high to describe the continuous distribution of the strain/temperature in the AM produced components. The Inconel substrate and installed fibers were fixed inside the LENS system for deposition using four hold-down bolts as shown in Fig. 16c. Additional Inconel layers were then deposited on the surface of the substrate to cover the embedded fibers as shown in Fig. 16d. The LENS process parameters are summarized in Table 3.

Table 3 The Parameters of the LENS Depositing Process

Process parameters	Values
Laser power	275 W
Laser scanning velocity	17 mm/s
Powder feed rate	26 round per minute (RPM)
Laser scanning angle	0°

After the LENS process, the sample was allowed to cool to room temperature for one hour. Substrate temperatures were confirmed by the fiber sensors inserted in the stainless-steel tubes. Residual strain measurements were performed after the substrate had cooled to room temperature.

2.3.2 Manufacturing Issues

The deposition quality is largely depended on the printing parameters. Inappropriate printing conditions may lead to fiber damage or failure to fully embedding. Here, we mainly consider the following parameters during the deposition process: laser power, laser scanning velocity, powder feed rate, and laser scanning angle.

In general, higher laser power and lower scanning velocity would result a much condenser metal deposition. However, this also means more heat is generated on the object surface, which may lead to burn or ablation of the fiber sensors. But, if the laser power is too low or laser scanning velocity too fast, the metal powder carried by the gas flow may not have enough heat to melt, which in turn leads to poor deposition or embedding quality. Similar thing happened with the powder feed rate: too much, the metal powder may accumulate at the molten pool, sometimes even prevents the following deposition; too few, there is not enough powder to absorb the huge heat generated by the laser, which leads to the direct ablation of the fiber sensors. To reduce thermal induced residual strain and avoid delamination, a proper laser scanning angle should be considered. Early studies show that each layer with different laser scanning angle will reduce the accumulated strain in the component.

2.4 Characterization of Embedded Fiber Optic Sensors

Though optical fiber sensors were successfully embedded into 3D printed components. Its sensing capability, both thermal and mechanical, still needs to be examined. In this chapter, we designed and performed experiments to measure temperature and strain distribution along embedded optical fiber sensors during the additive manufacturing process. And compared the experimental results with simulation analysis.

2.4.1 Temperature Measurement

In this section, the sensor embedded 3D-printed component was firstly examined through a temperature calibration test. The distributed temperature evolution was also captured during the cooling phase of the 3D printing process. The experimental result was analyzed and compared with the thermal simulation results.

2.4.1.1 Temperature Calibration

To examine the capability of the embedded fiber sensor, the component shown in Fig. 12a was used to monitor the temperature change and residual stress induced in the metal AM processes. To accomplish that, all three embedded fibers were fused together and connected to an optical backscattering reflectometer (LUNA OBR4600) that utilizes Rayleigh backscattering in the frequency domain to determine temperature change and strain with 5 mm spatial resolution. First, the samples together with a thermal coupler were moved into a furnace for temperature test calibration purpose. The temperature in the furnace was controlled to rise from room temperature (20 ºC) to 500 ºC. For every 100 ºC, the temperature was ramped for 10 minutes and maintained for 20 minutes before next ramping period. The measured temperature vs. time plot was shown in Fig. 17. The blue, black, and red curves represent the temperature measured through the thermal coupler, optical fiber outside of the tube, and fiber in the tube, respectively. It can be seen from the plot that the optical fiber outside of the tube matches pretty well with the temperature measured by the thermal coupler, especially at higher temperatures. Due to the air gap between the inner surface of the stainless-steel tube and the optical fiber, it requires more time to reach the desired temperature inside the tube and the sensitivity of the temperature sensor is lower (especially below 300 ºC).

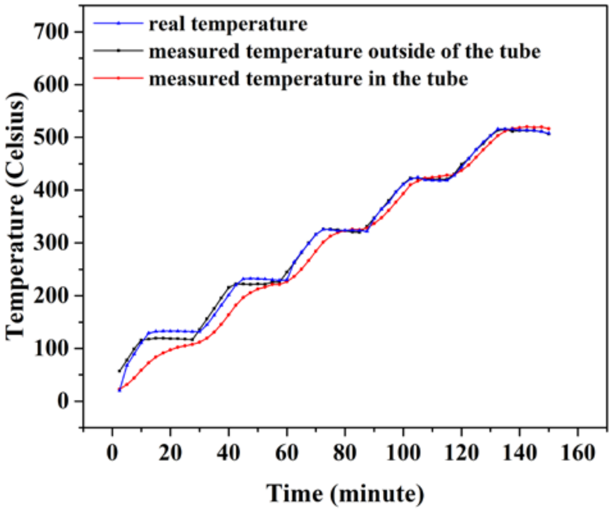

Figure 17 Temperature calibration tests for the embedded sensors.

2.4.1.2 Temperature Evolution in Cooling Process

To test the temperature and strain sensing capabilities of the embedded sensors, the LENS system performed deposition that covered a volume of 55 (L) × 72 (W) × 0.6 (D) mm^3 using IN718 powder with average particle sizes of 50~150 μm (TIMET®). The LENS system required 72 round-trip passes to cover the deposition area once, with 2 layers to reach the desired thickness. In each laser pass, the LENS system deposited a trace of 0.5 mm wide and 0.3 mm thick. Temperature profiles were captured using the Rayleigh backscattering OFDR instrument. The temperature profile was measured right after the laser deposition was completed, because mechanical vibration impeded measurements during deposition. These results are presented in Fig. 18. The temperature profile was recorded right after the laser deposition was completed and the laser was turned off. Therefore, the temperature profiles measured at T = 0 min shown in Fig. 18 were taken at 395, 233, 72 seconds after the laser had completed deposition for Sensor 1, 2, and 3, respectively. All temperature profiles measured by three fiber sensors in Fig. 18 were performed at the same time. It is evident that the embedded fiber sensors cooled rapidly from the local laser heating. The peak temperature of Sensor 3 dropped from the melting temperature of the Inconel powder (> 1400 °C) to 335 °C after 72 seconds. The accelerated thermal convection and conduction toward both ends of deposition area lead to faster cooling rates compared to those in the center of the deposition area. The temperature profiles became uniform across the substrate after about 5 minutes and returned to the chamber ambient temperature after 30 minutes.

The measured temperature increases were then compared to the temperatures simulated using FEA with boundary conditions described in Section III. The finite element model-derived temperatures across the entire two-layer part are shown in Fig. 19a and 19b. The temperature profile during the laser scanning powder fusion process is shown in Fig. 19a. The temperature at the laser fusion point readily exceeds 2500 °C. This process simulation was performed while 45 % of laser power (275 W) was absorbed by the deposited powder and substrate [89]. The *1/e* width of the laser focal spot was estimated as 520 μm diameter spot, which is the fabrication resolution of the LENS process. The long comet tail as seen in Fig. 19a shows the temperature contours resulting from the laser scanning and powder fusion, which is a typical feature of the AM laser sintering process. Simulation results shown in Fig. 19a and 19b highlight drastic and rapid temperature change over very short period of times (0.5 second) right after the completion of the deposition. Over 0.5 second after the turn-off of the point laser heat source, local temperature around the focal spot drops from over 2500 °C to less than 1000 °C. Heat quickly spread and dissipated across the entire substrates. For area further away from the last laser deposition point, the point laser source will have fewer impacts on its cooling process, which has been well underway.

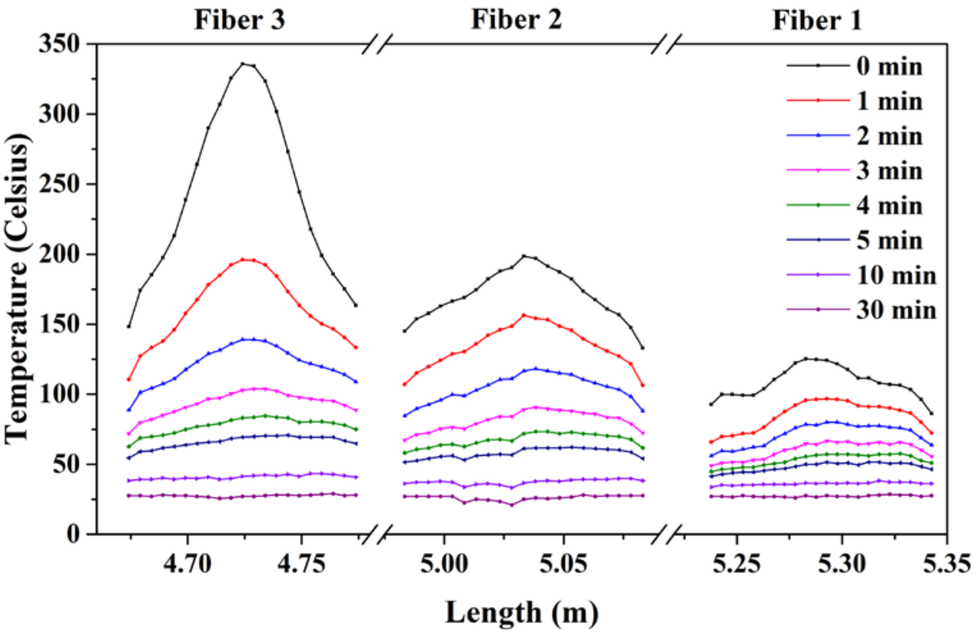

Figure 18 The fiber-measured distributed temperature history profiles at different positions in the cooling period after the depositing process.

To compare the simulation results with those measured by the fiber sensors, the temperature data were extracted at the time of 1 second right after the deposition was completed, as the same sampling time point adopted in the in-situ experimental measurement. The simulated temperature profiles at the locations of the three fibers are compared with measured temperature profiles using the embedded fiber sensors. These comparisons are presented in Fig. 19c-e.

Although the surface temperature change at the deposition location is very drastic right after the laser powder deposition, our simulation shows that the temperature change is significantly more modest just 1 mm away from the laser focal spot. It is noted that when the fiber sensor performed temperature profile measurements, 72 seconds lapsed after the laser scanned through the location of Fiber Sensor 3. The temperature gradient at fiber locations becomes smaller between the surface and embedded fibers. This allows sensor measurements to accurately reflect the surface temperature simulations. This is indeed the case as shown in Fig. 19c-e.

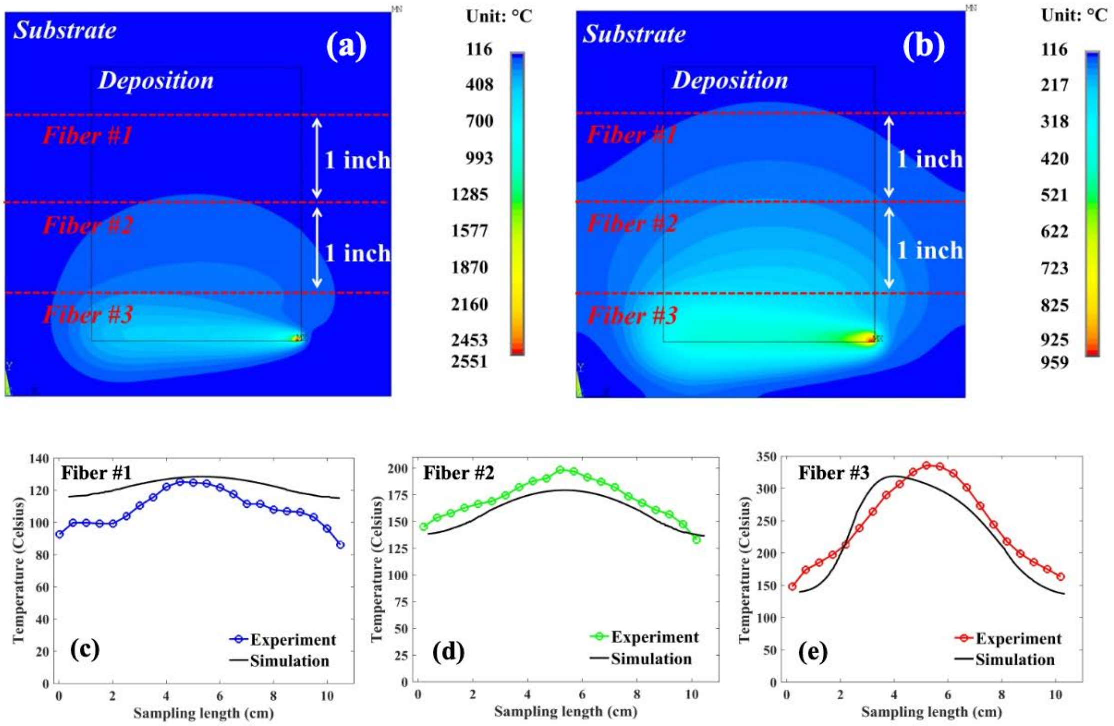

Figure 19 The simulated global temperature profiles of the LENS deposition process (a) upon the completion of the deposition, and (b) 0.5 second after the deposition process. Comparison of temperature profiles between the simulation results (b) and measured results by fiber sensors are shown in (c)-(e).

Overall, simulation results are consistent with the temperature sensors embedded by the LENS process. Both simulations and fiber sensors’ measurements yield the same locations of peak temperature located approximately in the middle of the deposition area with Embedded Sensor 1 and 2. The peak temperature measured by Fiber Sensor 1 agrees within 8 °C, while the discrepancy grows larger toward the edges. Average difference of the temperature profiles between measurement and simulation is 12 °C for Fiber Sensor 1. The simulation and measurement reach better agreement for Fiber Sensor 2. The simulation predicts 179 °C peak temperature, and this is 19 °C lower than the sensor measurement. However, the average temperature difference between the simulation and measurements drops to 10 °C. The discrepancy between the simulation and the experiment is consistent across the entire temperature profiles at this location. As we move to the locations closer to the laser heating source, both simulation and measurements record higher temperatures. At location of Fiber Sensor 3, the FEA model predicts 320 °C peak temperatures, while the embedded sensor measured 335 °C. The FEA model predict the location of peak temperature at 3.6 cm to the left side of the deposition area as shown in Fig. 19e, while the fiber sensor measured the peak temperature at 5.2 cm to the right side of the deposition area. Possible reason for that difference is the exactly localized thermal boundary conditions of the depositions cannot be simulated. There may be some error between the simulated and practical thermal gradient in the cooling deposition area. As a result, the extreme temperature may be located at different positions. Additionally, the average temperature difference between the simulation and the modeling at this location is 20 °C.

2.4.2 Strain Measurement

Measuring distributed residual strain is one of the most important features of this project. The embedded fiber sensor captured the residual strain generated in the deposition process. The plastic strain was subtracted from the total strain by removing all fixtures of the sample, while the elastic strain was released. The measured strain was then compared with a FEA simulation for further analysis.

2.4.2.1 Measuring Residual Strain with OBR

However, a more important capability enabled by embedded fiber sensors is the measurement of strain distribution. In this work, all strain measurements were performed 60 minutes after the laser depositions to ensure strain measurements were performed at a constant temperature confirmed by the distributed fiber temperature sensors. The strain measurement was a two-step process. Distributed strain profiles were the first measurement after the substrate was cooled but still firmly attached to the deposition chamber using four bolts as shown in Fig. 16c. The strain measurements were carried out again after four bolts were removed and fiber sensor embedded samples are released. These results are shown in Fig. 20.

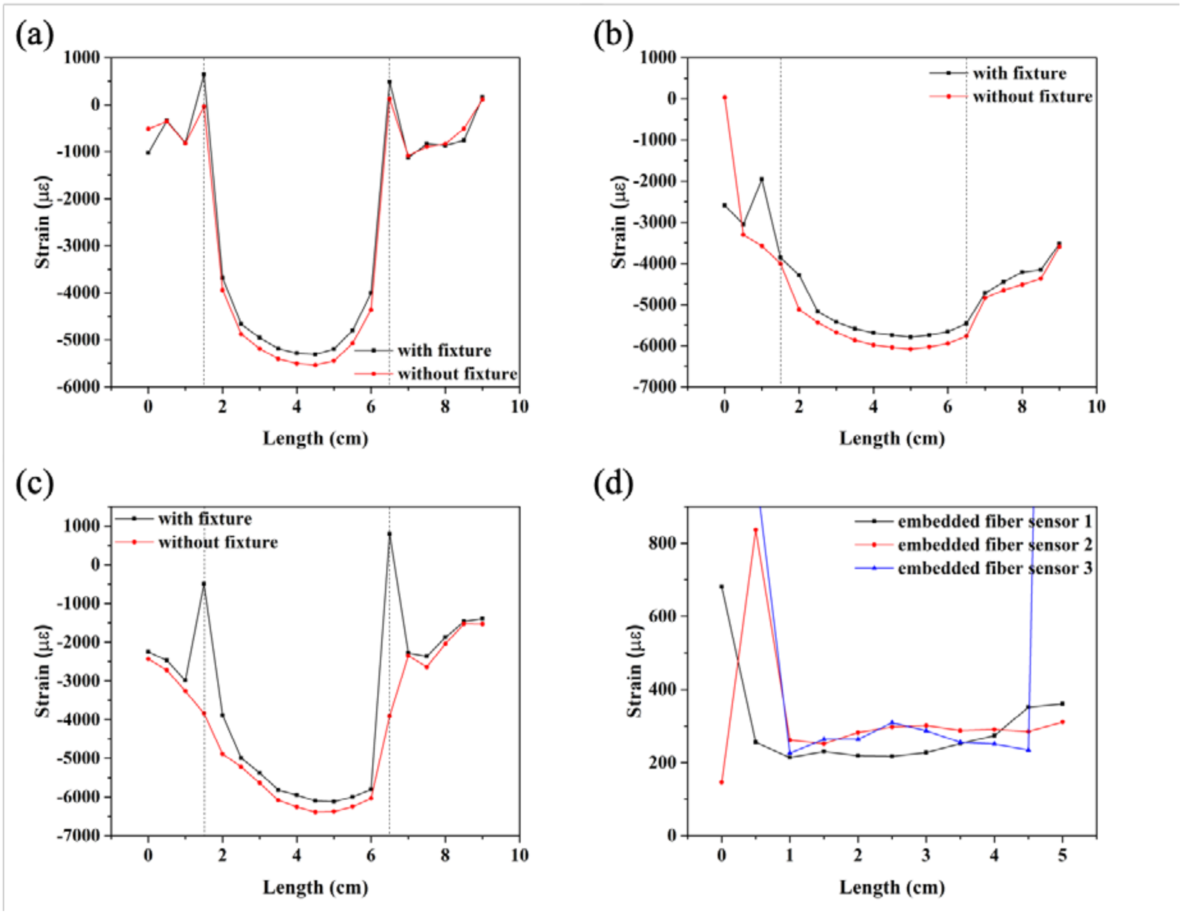

Figure 20 (a) The residual elastic and plastic strains induced in the metal LENS process measured by the embedded fiber (a) sensor 1, (b) sensor 2, and (c) sensor 3. (d) The released elastic strain measured by three embedded fiber sensors after relaxing the fixed substrate.

In general, the LENS process induced significant strain in the Inconel substrates. Black traces shown in Fig. 16a-c reveal over 5000-6000 με of compressive strain induced in substrates at three sensor locations. Peaks of the maximum strain tilt toward the right sides of the deposition areas. Toward the edge of deposition area, measurements of Fiber Sensor 1 show drastic reductions of strain, while the measured strains show less reduction by Fiber Sensor 2 and 3. Once the fixture bolts were removed, which allows relax of the substrate, strain profiles were measured again. The strain profiles after the sample relaxations are also shown in Fig. 20a-c (red), which reveals slightly higher compressive strain. The strain measured by fiber sensors after the sample relaxation is plastic strain that is permanently induced in the substrates during the LENS deposition. The elastic strains induced by the LENS process can be found by subtracting strains measured when the sample was relaxed from the strain measured when the samples were clamped. The elastic strain profiles measured by three sensors are shown in Fig. 20d. It can be seen from the plot that the elastic strains induced by the LENS process are rather uniform across the deposition area in all three locations in the range of 200~300 με tensile strains. Possible reason for small elastic strains is that there are very small gaps between the coated fibers and the trench inside surfaces. These gaps may cause weak bonding for the fibers and the elastic strains induced by heat can be naturally relieved in the cooling process. Although metal and silica fibers have large differences in their CTEs, which limited the application temperatures of embedded fiber strain sensors. However, at the room temperature, fiber sensors embedded in metal substrates can be suitable tools to measure strains induced by various processes. Fiber sensors can readily measure over ±10,000 με, thus strain induced by the 3D printing process as shown in Fig. 20 are well-within the measurement ranges of the fiber sensors.

2.4.2.2 Experimental Strain Distribution Compared with FEA Simulation

To gauge the validity of the sensor measurements, a post-processing FEA simulation was performed to compute the residual strains near the bottom surface of the deposition area. Since we cannot afford the expensive computational time of full-scale mechanical analysis to investigate the strains as discussed in Section III, this simulation was performed on a $56 \times 3.0 \times 0.6$ mm^3 area as shown in Fig. 21. The lower zoom-in plot in Fig. 21 shows the laser scanning trajectories in the small-scale simulated area. In total, 5 zigzagged parallel single-track laser passes were simulated using a very fine finite element mesh to ensure accuracy.

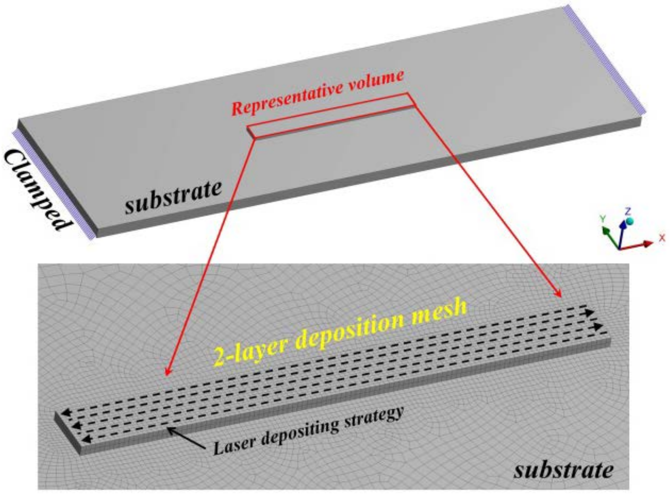

Figure 21 The small-scale process simulation model of the two-layer deposition (red box) as the representative volume of the large deposition area (upper), and the detailed laser scanning strategy in the laser fusion process (lower).

The mechanical strains were simulated in the elastoplastic analysis. Distributed plastic strain profile computed by FEA is presented in Fig. 22 together with measurement results by three embedded fiber strain sensors. Compared with the experimental results shown in Fig. 22, the strain distribution calculated by FEA is similar to the measurement results in the center region of the deposition area. The magnitude of the calculated plastic strain is around -5700 μƐ, which is close to the averaged measured strains. This consistency suggests that fiber sensors with thick metal protective jacket can be used to accurately measure residual strain induced by the LENS process. The two drastic changes in the plastic strain curve correspond to regions close to the edge of metal depositions. Due to the zigzagged laser scanning path, the laser beam stayed at the edge of the deposition area for slightly longer time, leading to more accumulation of residual plastic strain caused by the large thermal strain. This resulted in higher compressive strain along the edge of the deposition area, which yields two valleys in the simulated strain profile. The residual strain introduced by the LENS deposition rapidly decreases outside the deposition area. This leads to a large spike in plastic strain deposition around the edge area, which contributes measurement variation of fiber sensors shown in Fig. 22. This spike was not captured in the experimental measurement. The possible reason is that overlarge local deformation may cause some micro-bending of the optical fibers, which affects the precision of their measurement. Meanwhile, since the sharp transitional area in the curves is very narrow, it may locate in the interval where the spatial sensing points of the optical fibers are not available. This suggests that the 5 mm spatial resolution of fiber sensors is not adequate to capture these drastic strain changes around edges of the deposition. Despite the localized difference due to the edge effect, the rest part of the simulated and experimental curves matches very well.

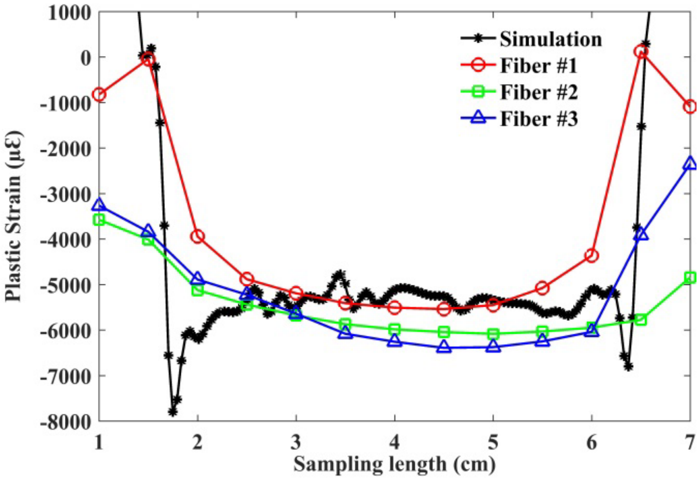

Figure 22 Comparison of the predicted residual plastic strains along the embedded fibers through detailed process simulation and the embedded fiber-based experimental results in the metal LENS process.

3.0 Embedding Fiber Optic Sensors in 3D Applications

Due to the layered deposition nature of additive manufacturing, the dimension of the embedded fiber sensor is limited in a 2D surface. Especially for AM techniques like DMLS and SLM, where recoating blades will be blocked by the sensor if the surface is not flat. However, thanks to the gap between laser head and deposition surface, LENS offers great opportunities to embed optical fiber sensors into more complex 3D structures with curved surface. In this chapter, we will introduce the procedures for embedding pre-shaped optical fiber sensors into 3D AM applications, and characterize the sensing capability through a standard static test.

3.1 Introduction

As introduced in previous chapters, to embed optical fiber sensors into metalized structures through additive manufacturing process, certain protective activities should be taken about the fiber sensors, since fiber sensors need to sustain extreme high manufacturing temperatures of the melting zone induced by laser, electron beam, or sintering furnace that often exceed 1500°C. A conventional solution is electroplating metal over the optical fiber to form a protection layer, which has already been covered in our previous works. However, when it comes to curved surface or even 3D structures, things become tricky, because it is difficult to maintain the shape of the fiber sensors in electroplating process. In this project, we successfully developed an efficient way to solve this problem.

3.2 Sample Preparation

In our project, we plan to embed optical fiber sensors in a turbine blade shown in Fig.23a to monitor its strain/temperature change. A curved shallow trench with 1.2 mm width and 1.25 mm depth was predesigned on the blade surface, where fiber sensor is going to be embedded. This structure was 3D printed with Ti-6Al-4V powder through selective laser melting (SLM). The same structure with base removed was 3D printed with resin using stereolithography technique to serve as the resin mold in electroplating process. In electroplating process, the optical fiber would be insert into the trench of the resin mold and electroplate with nickel using Ni sulfamate bath to form around 600 μm thick nickel protective layer. To better maintain the shape of the optical fiber in electroplating process, six "teeth" were added on top of the trench in resin mold, as shown in Fig. 23b. These teeth would be removed after few hours' electroplating to achieve thicker and more uniform electroplating results.

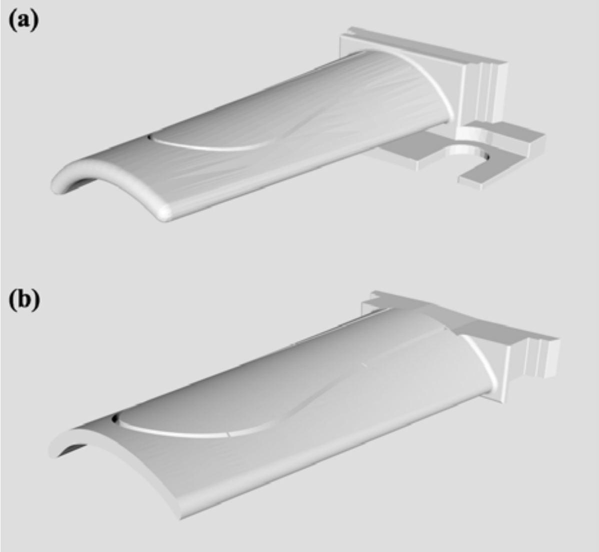

Figure 23 The 3D structure of (a) the printed turbine blade and (b) its resin mold for electroplating.

We used the same optical fiber (Cu1300 from IVG Fiber^{TM}) as introduced in Chapter 2, followed by the same cleaning procedures for sample preparation purpose.

3.3 Electroplating

The electroplating process is very similar as that introduced in Chapter 2. The same Nickel sulfamate bath was applied. However, to maintain the shape of the optical fiber sensor in the electroplating process, the pre-printed mold was required, and certain parameters need to be changed as well.

3.3.1 Electroplating Setup

After being thoroughly cleaned, fibers were insert into the trench as shown in Fig. 23b to keep its shape during electroplating. The optical fiber was then transferred to a nickel sulfamate bath (shown in Fig. 24a), with the same electroplating condition given in Table 2. The optical fiber was electroplated for 12 hours to form around 150-µm thick nickel layer. Then the teeth on the resin mold were removed and further electroplating the fiber with triple current density for another 12 hours to generate a 650-µm thick nickel coating on the optical fiber, as shown in Fig. 24b.

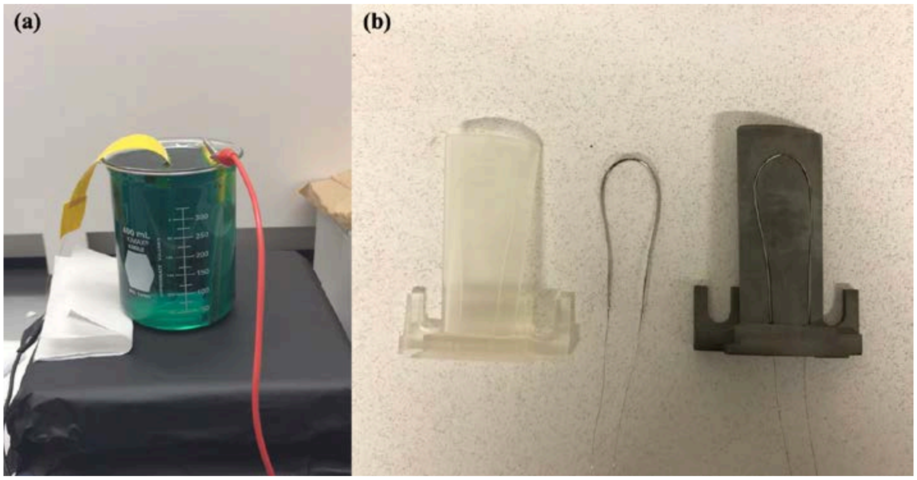

Figure 24 (a) optical fiber was electroplated with Ni sulfamate bath, (b) fixed by the resin mold, optical fiber maintains its shape after 24-hour electroplating process.

3.3.2 Residual Strain Induced in Electroplating Process

The electroplating process itself may introduce residual stress along the optical fiber, which can be monitored by OBR. Here we nickel electroplated two pieces of fiber samples and connect them to OBR to capture the distributed strain change as a function of time, the results are shown as Fig. 25.

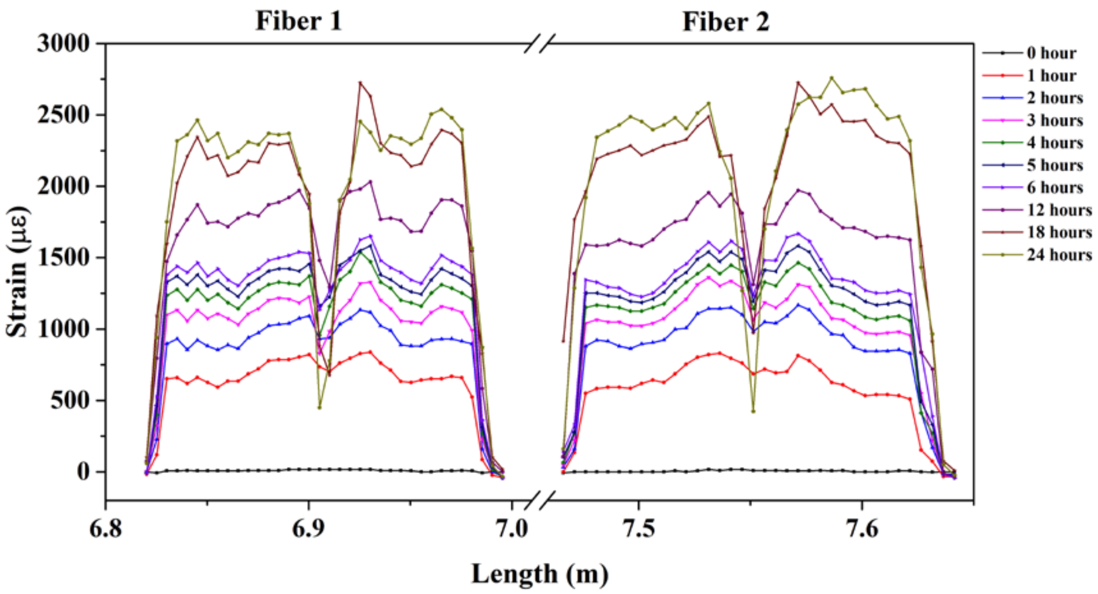

Figure 25 Distributed strain profile measured in electroplating process.

The two fiber samples show very similar strain profile: residual strain accumulated as the electroplating process went on, the center part of the electroplated optical fiber (top part on the resin mold) shows a sharp valley, which is probably because electroplating process expand the volume of the fiber, however, the fibers are limited by the fixtures at two ends and the trench itself, so fibers on two sides tend to compress the center part, which lead to a much lower strain.

The distributed strain profile was then inserted into the coordinate matrix of the pre-milled trench on the turbine blade through MATLAB, to plot the distributed strain in 3D at different electroplating time, as shown in Fig. 26. From the 3D plot, it can be seen that less strain accumulated at the end and the top part of the trench, which is probably because these parts acts as fixtures of the optical fiber during the electroplating process. While more strain was grown on the two sides of the trench.

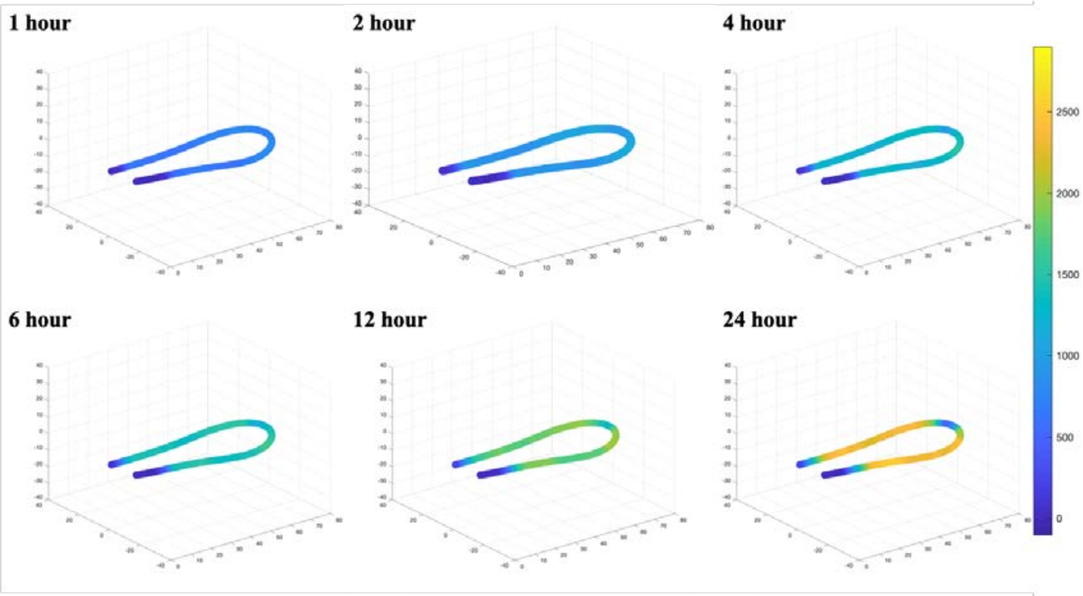

Figure 26 The 3D distributed residual strain accumulated on Fiber 1 in the Nickel sulfamate electroplating process.

We selected the median strain on two fibers at different time and plot the strain-time curve as shown in Fig. 27. It can be seen that regardless different electroplating current (0.03 A for Fig. 27a and 0.1 A for Fig. 27b), the strain profile increased exponentially vs time.

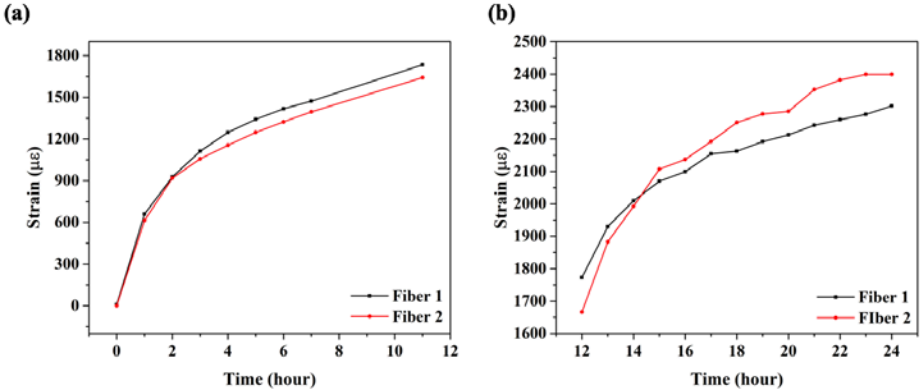

Figure 27 Strain profile vs time on two fiber samples (a) 0.03 A for first 11 hours, (b) 0.1 A for the rest 12 hours.

3.4 Embedding 3D Fiber Sensors

3.4.1 Modification for Curved Surface

After electroplating process, the Ni coated optical fiber was transferred into the trench of the 3D-printed Ti-6Al-4V turbine blade, as shown in Fig. 28, perfectly matched the trench on the turbine blade.

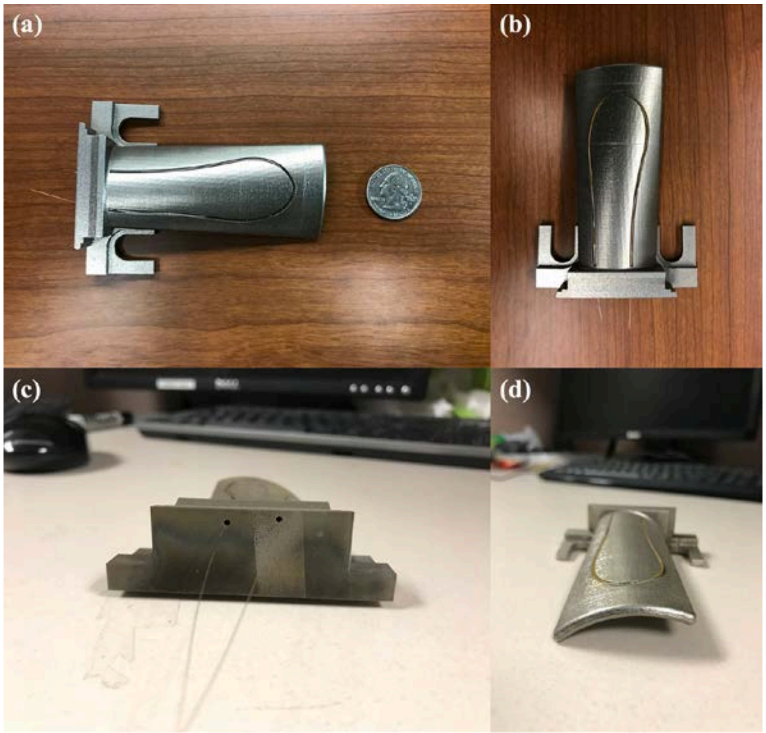

Figure 28 The Ni electroplated optical fiber was transferred into the turbine blade.

The turbine blade together with optical fiber in its trench was then moved into the LENS machine, shown in Fig. 29a, to perform the embedding process. The whole process can be illustrated like Fig. 29b.

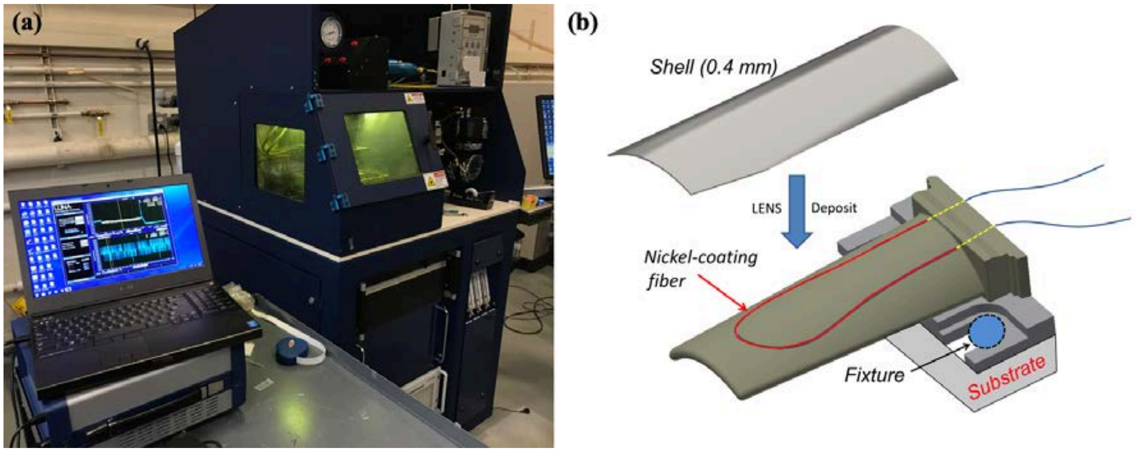

Figure 29 (a) Laser Engineered Net Shaping (LENS), (b) embedding fiber sensors using additive manufacturing technology.

We were going to print a thin Ti-6Al-4V shell, shown in Fig. 30, to cover the Ni-coated fiber sensor to achieve the embedding purpose. The detailed embedding parameters are given in Table 3.

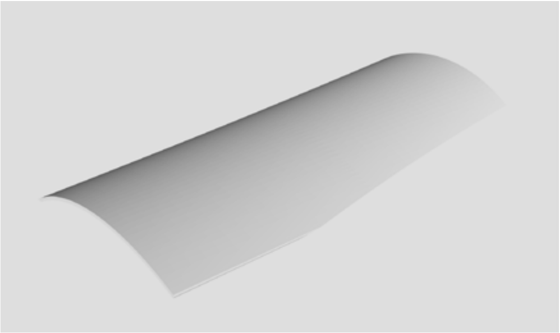

Figure 30 A thin Ti-6Al-4V metal shell was 3D-printed onto the turbine blade to embed fiber sensors.

3.4.2 Slice Model

3D printing is a layer-by-layer process. In order to deposit the thin metal shell on the sample, we need firstly slice it into multiple layers. The shell structure was sliced into 19 layers with 0.013 inch for each layer, as shown in Fig. 31. The red lines show the contour of each layer, while the yellow lines are the laser scanning path. In general, the LENS would scan the contour first and then fill the contour with metal powders following the laser scan path (those yellow lines). This would result a thicker deposition on the contour. So, to achieve a more uniform deposition results, we need to remove the contour (red lines) when generating the path planning code.

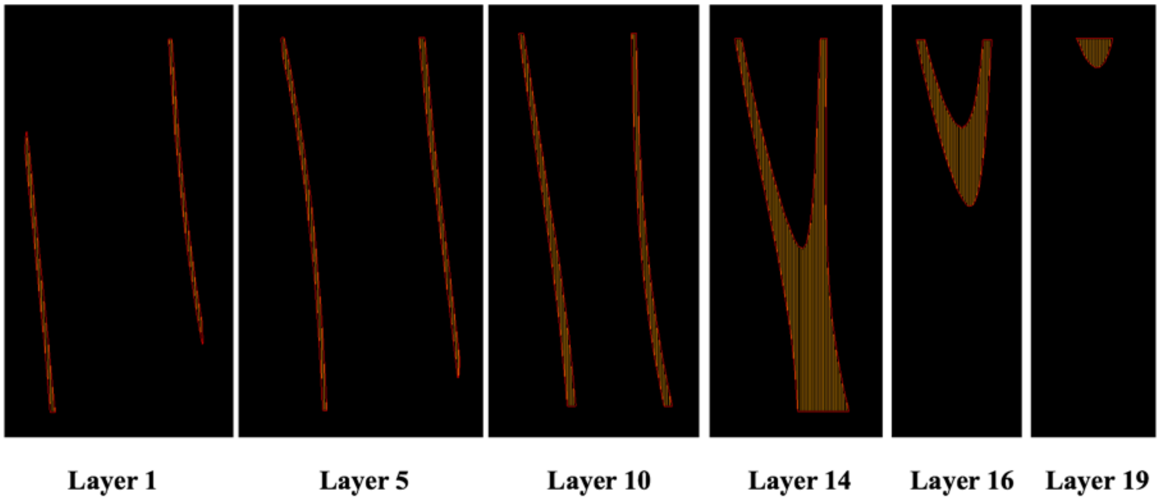

Figure 31 Each layer of the computer-generated slice of the metal shell.

3.4.3 Parameters and Embedding Issues

The whole deposition process was shown in Fig. 32. The whole structure was fixed onto the motion stage in LENS through two bolts. Then, a total of two layers of Ti-6Al-4V powder was deposited onto the turbine blade through LENS to fully cover the pre-shaped Ni coated optical fiber sensor. The final product is shown in Fig. 33 and is ready for further strain sensing capability test.

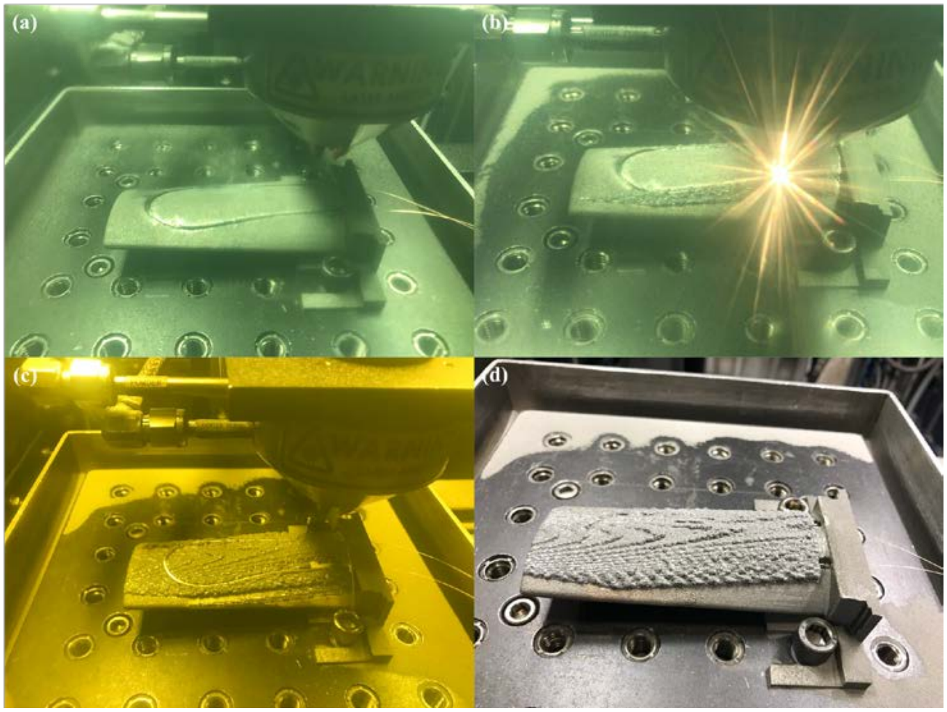

Figure 32 (a) The Ti-6Al-4V turbine blade with Ni electroplated fiber sensor was moved into the LENS chamber and fixed using two screws. (b) Deposition in progress. (c) A single layer was not enough to cover the fiber sensor. (d) After deposit the second layer of Ti-6Al-4V metal powder, the Ni-coated fiber sensor was fully embedded into the turbine blade.

Technically, the strain change induced in the embedding process could be monitored by the OBR in real-time. However, the R-OFDR makes OBR sensitive to the vibration. For LENS machining process, the sample was fixed on the stage, which kept moving followed the computer-generated path planning code. In addition, during embedding process, the phase change in fiber sensor was caused by both temperature and strain, the OBR itself cannot distinguish these two properties with a single fiber. But when it comes to direct metal laser sintering technique, it is a totally different story. The sample would be fixed on the plat form, while lasers scanning the sample controlled by a pair of Galvo mirror. If we embedded both a Ni-coated fiber sensor and a hollow metal tube with optical fiber insert in it (similar as what introduced in Chapter 2), it would be highly possible to monitor the distributed strain and temperature change in the 3D printing process in real-time.

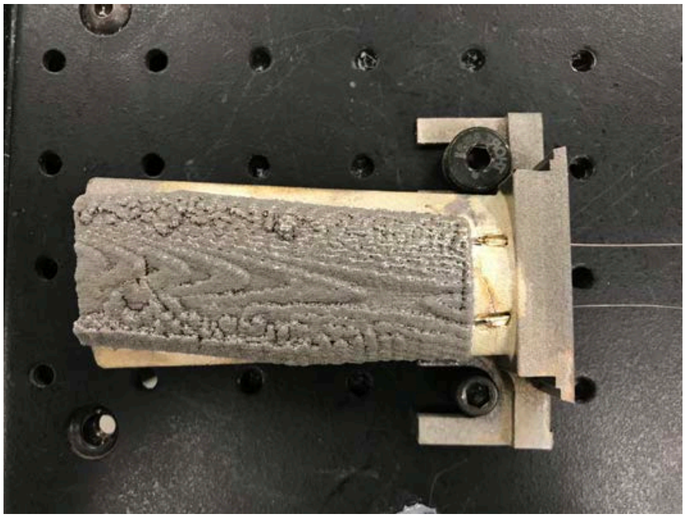

Figure 33 A zoom-in photo of the fiber sensor embedded component.

3.5 Sensing Capability Test

To test the sensing capability of the smart sensor embedded component, we performed a standard static test, to be more precisely, a cantilever beam bending experiment. The base of the turbine blade was fixed on the optical table, while the turbine blade forms a cantilever beam. A small hole with around 3 mm diameter was drill on the top part of the turbine blade (slightly to the left as can be seen from Fig. 34). A copper wire was insert into the small hole to apply load to the sensor embedded component during the static test. In this experiment, 5 loads: 32 N, 64 N, 96 N, 128 N, 160 N were applied respectively. The distributed strain along the embedded fiber sensor was captured through OBR and plotted in Fig. 35.

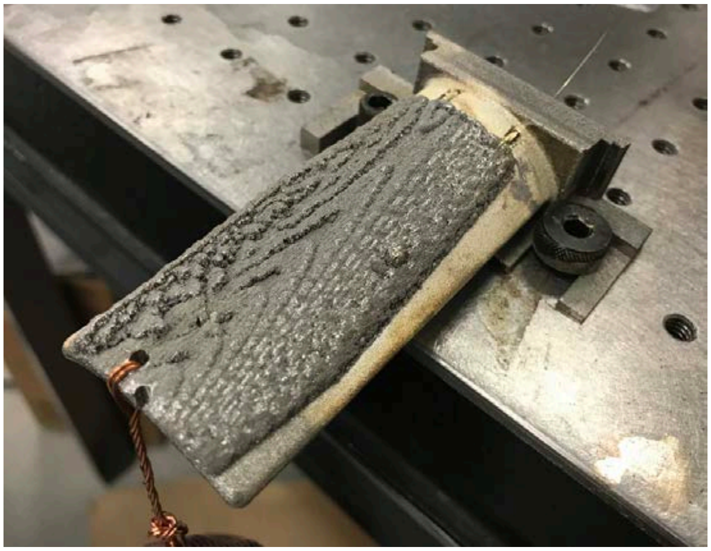

Figure 34 A cantilever beam bending test was performed to the fiber sensor embedded component.

It can be seen from Fig. 35a that the distributed elastic strain along the embedded fiber sensor was positive, which means tension, and in general, was increased when more load applied. We picked up five points along the optical fiber and labeled them as X_1, X_2, X_3, X_4, and X_5. The load-strain relationship at these five positions are given in Fig. 35b. Under the assumption of small deformation condition, the elastic strain has a linear relationship between the applied load. This can be observed at X_1, X_2, X_4, and X_5. Though slopes are different, the strain at these four points increased almost linearly as the load gained. However, this phenomenon does not apply to point X_3, which can be explained as follow: X_3 was close to the drilled hole where load was applied. The force was perpendicular to the fiber axis. And since fiber sensors can only capture strain change along its axis, so the measured strain doesn't show similar trend as that at other four points.

In addition, this sample is far from perfect. The embedded result can be significantly improved by adjusting printing parameters (metal powder flow rate, laser power, scanning path and direction, scanning velocity, etc.). The surface finishing can also be improved through post-machining like polishing and sand-blasting. The complex 3D structure and imperfect embedding condition lead to less accurate and less sensitive strain measurement results. So, our next goal is to optimize parameters and achieve better embedding results.

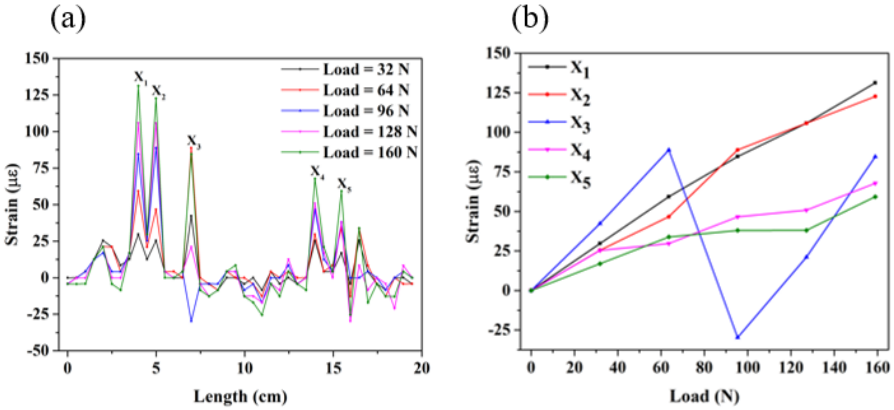

Figure 35 The strain distribution along embedded optical fiber sensor when different loads were applied to the cantilever beam.

4.0 Adaptive Laser Processing Method with Real-Time Strain Monitoring

4.1 Background

Laser shock forming (LSF) and laser shock peening (LSP) are laser processing methods that use laser-induced shock wave to perform high-precision geometrical adjustments or surface treatments of a work pieces. The LSF process uses high-intensity laser pulses to vaporize an opaque sacrificial film coated on sample surface. The ablation of sacrificial materials exerts strong recoiling mechanic shockwave into surface of the materials, which leads to plastic deformation that compress materials [91-93]. This process can effectively reduce defect density near the surface, which improve surface quality. The LSF has also been widely used to adjust geometrical shapes of work pieces. As a contact-free and mask-less process, the laser shock forming process can form component without any mechanical tools [92-94]. Compared with laser thermal forming methods, laser shock micro-forming is a non-thermal method only changes material around the laser focused area, which makes it possible to form work pieces at the room temperature with high precision.

The first laser shock forming works were performed in the late 1960s, while high intensity laser beam was used to form and to enhance aeronautical aluminum alloys [95, 96]. Since then, various plasma confinement schemes were studied to enhance the laser-induced shock waves to improve the laser processing outcome. Since then, the laser forming process has been widely used in manufacturing and material processing. Although the LSF process have been extensively explore for large work pieces since 1980s, its application for structures at millimeter scale or below have been recent endeavors. This is driven by the flourish of miniaturized mechanic components, micro-electromechanical systems (MEMS), and even nano-mechanic structures. For example, during the fabrication of MEMS devices, micro-mechanic structures such as free-standing structures or suspension structures are susceptible to the residual stress accumulated within materials. The laser shock micro-forming (LS-µF) process could be the effective approach to adjust their geometrical shapes even after the release of the micromechanical structures. However, the adaption of the LSF to handle small work pieces at micrometer scales is not straightforward. In early 1980s, the laser forming process have been extended to process miniaturized metal structures and components at millimeter scale to address precision manufacturing demands on miniaturized electromechanical systems [96].

Compressive stress can be induced on desired surface of the work piece to improve mechanic strength. This is impossible for any other microfabrication technique. Forming of work pieces with extraordinary curvature can also has also been achieved [92-94]. The LS-µF process is a non-contact high-precision laser processing scheme to improve surface quality of specimen [91]. It has also been widely used to adjust geometrical shape and to control residual stress in MEMS structures. The increased requirement on the manufacturing precision on large work pieces also require more precise laser forming processes. Over the last decade, the laser forming process have been further extended to the micrometer scale to handle smaller work pieces in MEMS devices, micro-optical components, and even nano-mechanic structures [97-99].

Although the laser shock micro-forming has been extensively studied over the last decades, most of experimental researches have been performed using a laser beam with Gaussian shape. The existing laser forming process is a point-by-point laser processing scheme, where a single focused beam is scanned through the targeted working area using computer-controlled motion stages. When handling specimen with large sizes, this point-by-point laser process could have sufficient resolution to deform workpiece with required precision. This is because the laser focal size and laser-induced shockwave profiles is much smaller than the size of the specimen. However, the laser-induced shockwave produced by a focused Gaussian beam has a circular profile. When the laser shock forming process is used to handle small workpiece in micrometer scales, the laser-induced shockwave profile, even produced by a highly focused Gaussian beam, is comparable to the size of the workpiece itself. The circular shockwave profile might not be able to yield required deform for micro-components.

To address these challenges, this section presents an adaptive optical technique for laser shock micro- forming process. Using a computer-controlled spatial light modulator (SLM), the on-target laser foci can be flexibly formed in arbitrary shapes to excite laser shockwave with suitable size, shape, and intensity. Shockwaves simultaneously excited at multiple locations by multiple laser beams can also be generated. Using this flexible pulse laser beam forming tool, this paper presents studies shockwaves with noncircular profiles to deform free-standing MEMS structures on micrometer scales. Shockwaves simultaneously induced by multiple laser beams and their effects on the mechanic deformations on MEMS structures were also presented. This paper shows that the adaptive optics pulse laser beam forming tool can significantly improve the manufacturing flexibility, precision, and throughput of the laser shock micro-forming technique.

4.1.1 Laser Induced Shockwave

The principle of laser shock forming is shown in Fig. 36. A pulsed laser beam with high power intensity and short irradiation duration is focused on the metal specimen surface covered with a layer of absorbent coating and transparent confine overlay, which causes the absorbent coating at the surface of the work piece vaporized and ionized immediately. In the meantime, high pressure plasma is generated at the focusing area and expanded rapidly. Some remaining laser shock energy is absorbed by the vapor and plasma, leading to violent expansion and explosion at the surfaces of the metal specimen. The confining layer then traps the vapor and plasma, preventing the energy from expanding outward the metal specimen, and consequently causes the higher pressure to rise transiently. As a result, the peak pressure of the shockwave induced by the laser focused at the sample surface is greater than the dynamic yield strength of the material, generates the plastic flow on the metal sample, leaving residual stress on the yield region, which in turn leads to deformation of the metal specimen to balance with the stress [100]. With laser shock forming processing, when the stress of the up surface is larger than that of bottom surface, there will be convex deformation; otherwise, the result is concave deformation [101]. As a non-thermal laser process, LSF takes advantage of the laser induced shockwave to adjust the curvature of metal samples. Compared with conventional forming methods, LSF shows advantages such as non-contact, tool-free, high efficiency and precision. Moreover, the laser induced compressive stress at the metal surface may also enhance its mechanical properties like improving hardness and preventing metal fatigue or corrosion [102].

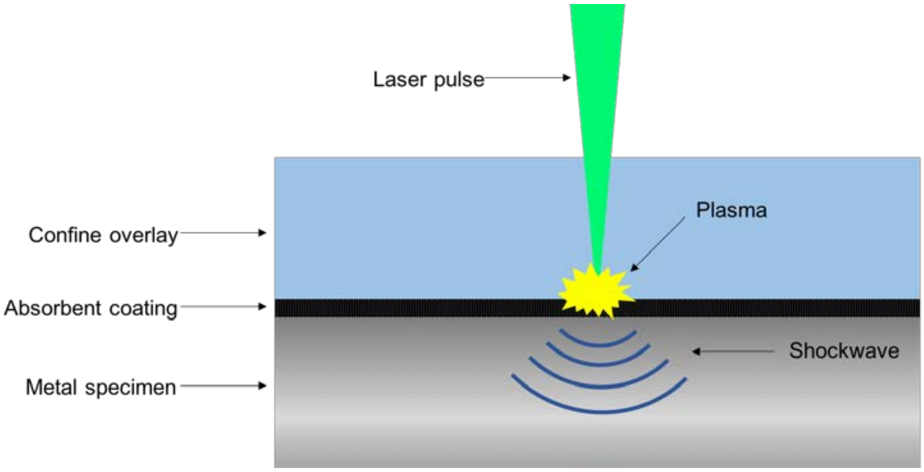

Figure 36 Scheme of Laser shock micro-forming.

4.1.2 Absorbent Coating and Confine Overlay

Laser absorbing sacrificial coatings (commercially using flat organic paint, black tape, or aluminum foil) are conventionally applied on the metal surface during laser shock process to enhance the intensity of the laser induced shockwave, but also protect the metal surface from ablation and melting. In laser shock process, the laser pulse has short energy deposition time, which in turn limits the diffusion of thermal energy just a few microns away from the interaction zone. In general, the sacrificial coating has a thickness greater than tens of microns, which is thick enough to protect the metal specimen beneath the coating [103]. After the initial explosion, the laser generated plasma and vapors continue to absorb the laser energy until the end of the energy deposition [104]. Without the absorption layer, the laser heated zone caused by the thermal effect is compressively plasticized by the surrounding material during the dilatation, possibly causing undesirable tensile stresses after cooling. In the contrast, if the metal surface is protected by a thermal absorbing material, the thermal effect then only occurs in the coating layer. However, the laser induced shockwave penetrates the coating layer and creates a pure mechanical effect on the metal surface. After the laser pulse duration, the surrounding material reacts to the volume expansion of the treating zone and generates a compressive stress field in the metal specimen [105-111]. Early studies report that the thermal protective coating is a key element to enhance plasma properties and the plasma pressure [106, 109-111]. In order to increase the magnitude of dynamic stresses in the metal material, the coating layer could combine its constraining characteristics with some impedance mismatch effects [106, 111]. When using a thick enough coating with low acoustic impedance, a much higher magnitude of dynamic stress than the plasma pressure, compared with that in the uncoated material could be achieved inside the material [111].

In laser shock processing applications, without a transparent overlay on top of the sacrificial layer to confine the laser-induced plasma and prevents it from expanding freely from the solid surface. Accordingly, the incident laser energy will be less efficiently converted into shockwaves to induce compressive residual stresses in the metal. Compared to plasmas generated in vacuum state, transparent overlays (such as water and glass) could increase the shockwave intensity propagation into the metal by up to two orders of magnitude [111].

4.1.3 Spatial Modulation of Laser Pulse

4.1.3.1 Spatial Light Modulator

A spatial light modulator (SLM) is a liquid crystal device that modulates light by converting digitized data into coherent optical information according to a fixed spatial pattern, which makes it an essential device in a wide variety of applications, including beam steering, optical tweezers, diffractive optics, pulse shaping and more. The scheme of a phase-only liquid crystal SLM is shown as Fig. 37. Polarized light enters the device from the top, passes through the cover glass, transparent conductive film, and liquid crystal (LC) layer, then gets reflected from each pixel electrodes and returns through the same path. Drive signals generated from the driver boards travel through circuitry in the silicon backplane (VLSI die) to each pixel. The analog voltage induced on each electrode (pixel) produces an electric field between that pixel and the cover glass. This field produces a change in the optical properties of the liquid crystal layer. Since each pixel is independently controlled, a phase pattern may be generated by loading different voltages onto each pixel.

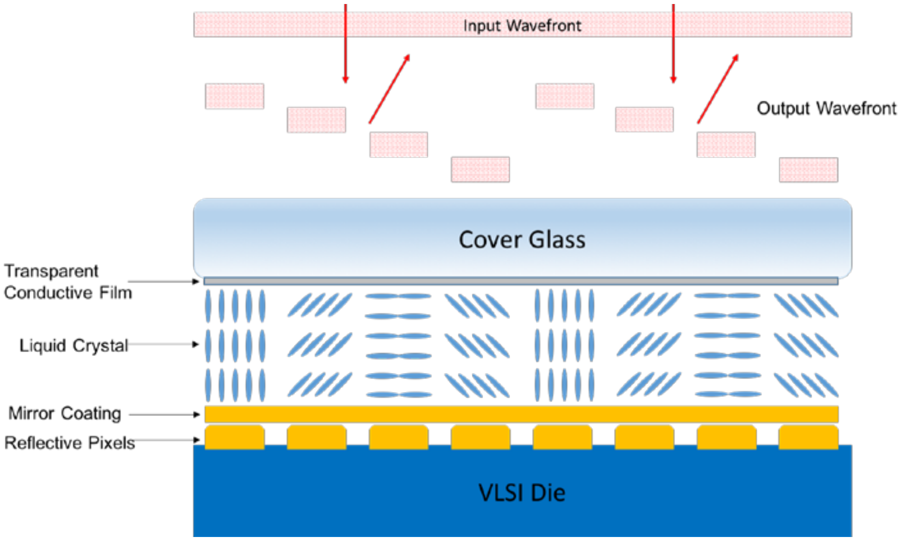

Figure 37 Cross sectional illustration of a liquid crystal spatial light modulator.

4.1.3.2 Phase Modulation

The phase-only spatial light modulators are fabricated with nematic liquid crystal, aligned in a homogenous configuration. Nematic liquid crystal has a variable electro-optic response to voltage. A simplified side view of a spatial light modulator's liquid crystal layer is shown in Fig. 38. When no voltage is applied to the LC, the molecules are parallel to the SLM cover glass and VLSI backplane. In this case, incident light will experience the largest difference between the extraordinary (n_e) and ordinary (n_o) index of refraction. As the voltage applied to the liquid crystal increases, the LC will tilt until the extreme is reached and the LC is nearly normal to the SLM cover glass and VLSI backplane. At this point the difference between the extraordinary and ordinary index of refraction is nearly zero.

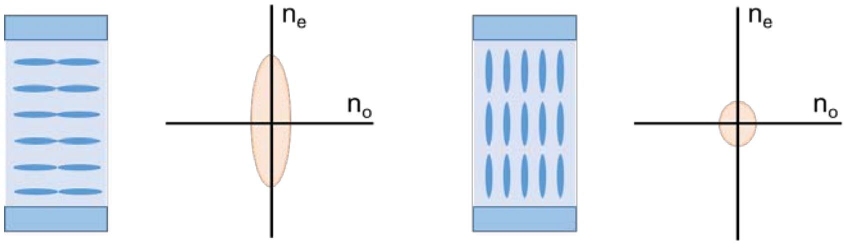

Figure 38 The diagram illustrates the liquid crystal orientation with respect to the coverglass and VLSI backplane as a function of applied voltage. The molecules are parallel to the coverglass and backplane when no field is applied, and are nearly perpendicular to the coverglass and backplane when full field is applied.

If light incident upon the SLM is linearly polarized and parallel to the extraordinary axis, then a pure, voltage dependent phase shift will be observed. For example, if no voltage is applied to the pixel, the maximum phase retardation (typically a full wave at the design wavelength) will be applied. Likewise, if the pixel is programmed for maximum voltage, a minimum phase delay is applied. The result is a programmable phase modulation on a per pixel basis.

Each of the SLM pixels is independently programmable to 65,535 discrete voltage states, all providing phase modulation. The response of the liquid crystal within the SLM to the applied pixel value (voltage) is nonlinear. To account for this, a look-up-table (LUT) is usually combined with the SLM. When this LUT is applied to an input image, the result is a linear output phase response ranging from 0 to 2π.

4.1.3.3 Optical Test Setup

Depending on the application of the SLM, many different optical setups can be used for either combined phase-amplitude mode or phase-only mode. Two examples of phase-only optical test setups are shown below.

The first optical setup, illustrated in Fig. 39, is a modification of a Twyman-Green interferometer [112]. Here, a monochromatic and collimated light source passes through a non-polarizing 50:50 beamsplitter to split the beam into two beams with equal intensity. One of these beams illuminates the SLM, while the other illuminates a reference mirror. Each of these reflected beams is then recombined at the image plane of a lens. If the reference mirror and the SLM are perfectly aligned such that they are nearly coplanar, interference fringes will be visible at the image plane. A camera is usually placed at the image plane to magnify the fringes for easier viewing. When the phase-only SLM is driven with different phase patterns, dynamic interference fringes can be viewed. Analyzing the interference fringes will then provide insight into the phase modulation provided by the SLM [113].

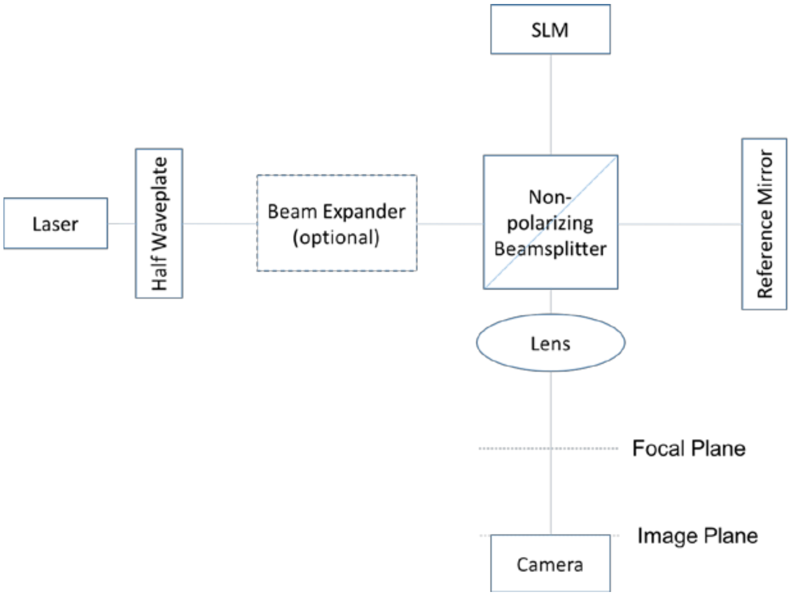

Figure 39 A Twyman-Green interferometer for testing a phase only SLM.

An off-axis setup, shown in Figure 40, is designed to maximize throughput by eliminating the non-polarizing beam splitter. A laser beam is incident on the SLM with a slight angle, reflects off of the reflective pixel pads, and then imaged onto a camera through a lens. Since this optical setup is not an interferometer, the actual phase modulation will not be visible on the camera. The off-axis angle should be kept to a minimum in order to reduce crosstalk effects due to the beam traveling through more than one-pixel region. Minimizing the off-axis angle also keeps the phase stroke closer to the designed value.

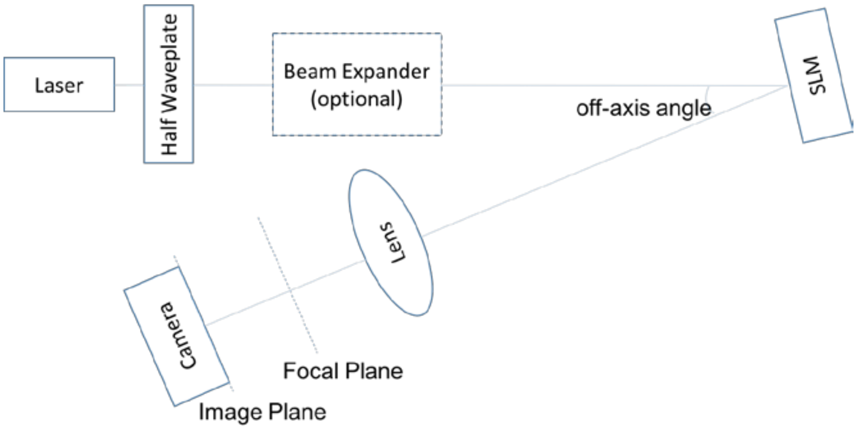

Figure 40 Off-axis optical setup for the phase only SLM.

There are a few important parameters to be considered when working with an SLM.

Polarization – The SLM is basically a variable single-order retardation plate, or wave plate. Like all wave plates, there is a fast axis and a slow axis. However, for most phase-only SLMs, only the index of refraction along the slow axis can be modulated electronically. When the light source is linearly polarized and parallel to the slow axis of the SLM, the result is phase-only modulation of the light source. If instead the light source were incorrectly oriented to be linearly polarized perpendicular to the slow axis, there would be no modulation observed with variable voltage. The use of a passive half-wave plate will greatly facilitate achieving the desired polarization alignment.

Diffraction – The SLM has discrete, reflective pixel pads in order to isolate the electrical signals and allow phase patterns to be written into the SLM. As a result of these discrete pixel pads, there will be diffraction. This diffraction can easily be seen in the focal plane of the lens. There will be a very bright center spot (0^{th} -order), surrounded by a grid of spots becoming progressively dimmer as they get further from the 0^{th}-order. In order to attain the maximum throughput, it is suggested to use as many of the diffracted spots, or orders, as possible. However, some applications do not allow the use of more than one order (typically the 0^{th}-order).

Dispersion – Liquid crystal waveplates are not very achromatic because the index of refraction varies as a function of wavelength. This dispersion means that a device designed to provide a 2π phase stroke at one wavelength, will provide less than 2π phase stroke at a longer wavelength, and more than 2π phase stroke at a shorter wavelength.

Optical Quality – Due to the very small pixel pitch of the SLM, it is important to use high quality optics. A single element lens will generally have too much spherical aberration to provide a good, sharp focus across the entire clear aperture of the SLM. As a result, it is recommended to always use at least a doublet lens. For the same reason, the longer the focal length of the lens, the better the resulting image at the image plane. In addition, the transmitted wavefront distortion of most beamsplitter cubes is typically around $\lambda/4$, contributing to unacceptable wavefront distortion at the image plane. The use of a beamsplitter plate in place of a beamsplitter cube could improve the wavefront distortion, but using a beamsplitter plate requires the use of a compensating plate in the reference leg of the Twyman-Green interferometer.

4.1.4 Gerchberg-Saxton Algorithm

The basic algorithm is an iterative procedure which is shown schematically as Fig. 41. The input data to the algorithm are the amplitudes picture at the source plane and amplitude of the target image. The amplitudes are proportional to the square roots of the measured intensities. The two sets of data are accessed once per complete iteration.

To begin with, a random number generator is applied to generate a series of random number between π and −π which serves as the initial estimate phase function. The phase function then multiplies the amplitude plane at source, and the Fourier transform of this synthesized complex discrete function is performed. After the Fourier transform, the amplitude is an approximation of the target amplitude plan, which comparing with the target intensity to decide when to break the iteration. The phases of the discrete complex function resulting from the Fourier transformation are extracted and combined with the target amplitude to form a new distribution function. Then, by performing the inverse Fourier transform on this function, the new phase function of this estimation is going to replace the random phase function mentioned in the first step of the iteration, and the process is repeated until the intensity error between the approximation and target is acceptable.

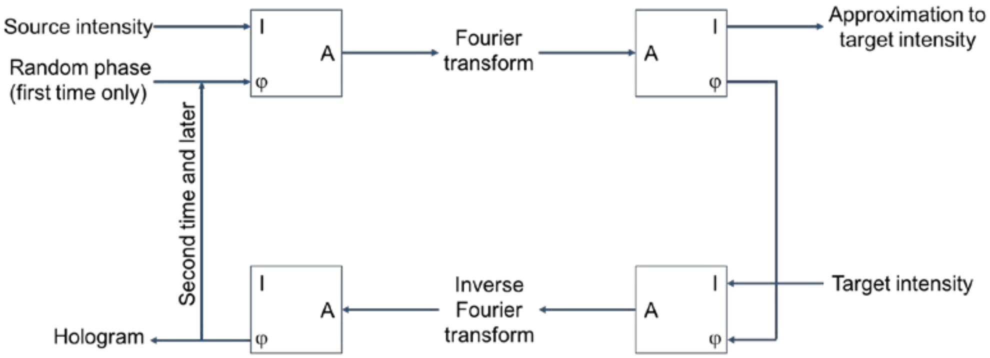

Figure 41 Scheme of Gerchberg-Saxton algorithm.

4.2 Adaptive Laser Shock Micro-Forming in 3D MEMS Device Fabrication

4.2.1 System Setup

The experimental setup is schematically presented in Fig. 42. The laser used in this study was a Nd:YAG Q-switched laser (Quanta-Ray GCR-11). The laser operated at the wavelength of 532 nm with 10 Hz repetition rate. The pulse duration is between 6 ns and 7 ns. The Gaussian-shaped beam size is 6.4 mm (FWHM) in diameter at the laser output. The laser was first expanded to 13 mm in diameter using a pair of spherical lenses as the beam expander. The pulse energy is controlled by an attenuator which consisted of a half-wave plate and a polarizing beam splitter. The polarization beam splitter also ensured that the output laser polarization matches the primary axis of the SLM in order to maximize the modulation efficiency. The SLM (Boulder Nonlinear System, P512-0532) is a liquid-crystal-on-silicon SLM with 512 by 512 pixels operated in reflective mode. The SLM is controlled via 16-bit DVI controller which gives a 200 resolvable phase level between 0 and 2π at 532 nm. A 10-mm square aperture was used to select the laser beam to cover 95% of the active area of SLM in the center. The SLM generated a hologram with a virtual image behind itself. An adaptive Gerchberg-Saxton algorithm was used to calculate the pattern on the hologram [114]. This virtual image was then relayed and focused onto sample surface through lens 1 (focal length of 400 mm) and lens 3 (focal length of 20 mm).

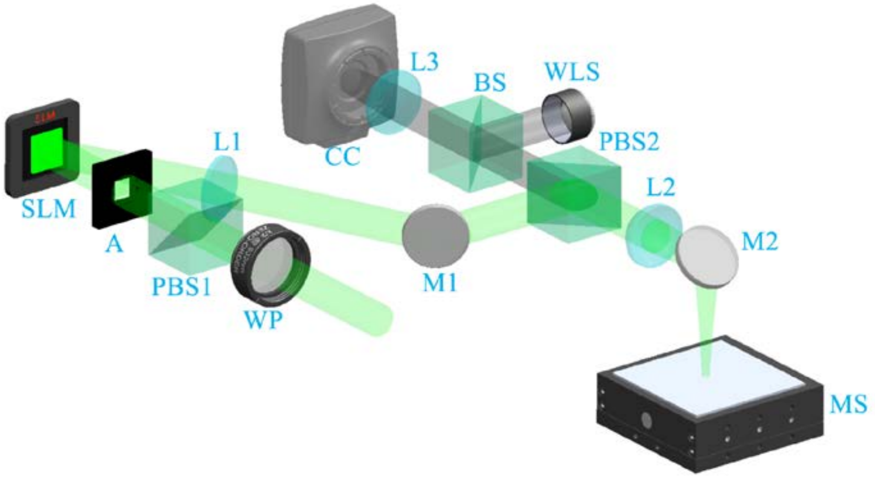

Figure 42 Sketch of the proposed adaptive laser system for the LS-μF process. WP: Half-wave plate; PBS: Polarizing beam splitter; A: Aperture; L: Lens; SLM: Spatial light modulator; M: Mirror; BS: Beam splitter; MS: Motion stage; WLS: White light source; CC: CMOS camera.

An optical imaging setup was also implemented to observe the LS-μF process on sample surfaces in real time. This imaging system consist of a CMOS camera and an imaging lens. A white light source was used to illuminate sample surface using a beam splitter cube. The overall adaptive laser beam forming system project 30% of the laser output on the sample target surface. This is largely limited by the diffraction efficiency of the SLM. The peak laser intensity is limited by the damage threshold of the SLM of 3.5 MW/cm^2 for laser pulse. In this experiment, the peak laser intensity was capped to below 1 MW/cm^2 to avoid equipment damage.

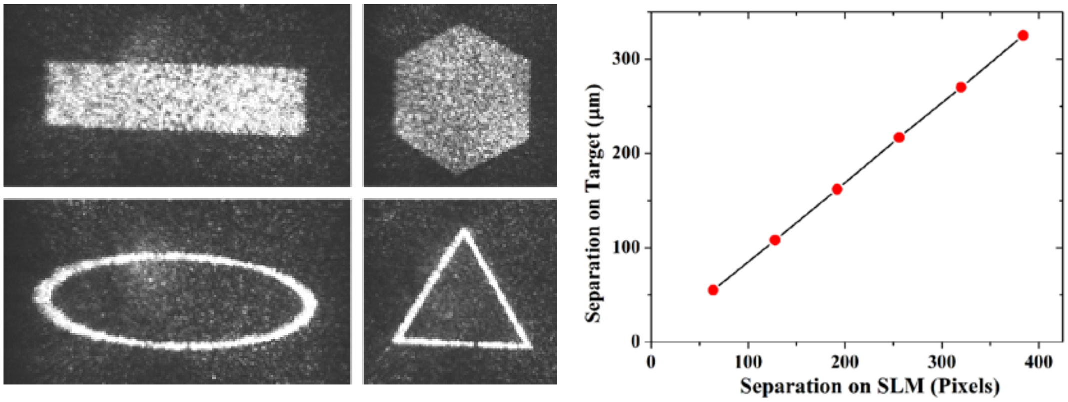

Figure 43 (a) Various laser beam shapes projected on an aluminum surface recorded by the CCD camera. (b) the SLM calibration results between the imaging pixel size and the actual on-target size of the laser projection.

Fig. 43a shows four examples of the laser beam shaping using the SLM. These shaped beams were projected on the target surface and recorded by the CMOS camera. The spatial light modulator was firstly calibrated to accurately control the beam shape and size on target. This was accomplished by a calibration experiment. A pair of bars with the width of 1 pixel was projected onto a flat aluminum plate to generate two ablation marks. By measuring the separation of the separation of the ablated line features. The correlation between SLM input image in term of number of pixels can be related to physical separation on targets. Fig. 43b shows the calibration results using two bars separated by 64, 128, 192, 256, 320, and 384 pixels, respectively.

4.2.2 Results and Discussion

In this thesis, free-standing MEMS structures were fabricated in 8111 aluminum alloy foil with 20 μm thickness. The free-standing structures is bridges with 750 μm in length and 125 μm in width. They were fabricated via the laser ablation process. Fig. 44a show a SEM photo of the MEMS structures. The metal surface was spray coated with KRYLON® Colormaster™ paint as a sacrificial layer. The thickness of the sacrificial layer was measured by an optical profilometer (Zygo NewView 8000) to be ~10 µm. Liquid water was used as plasma confined media. The samples were then submersed in waters with 3-mm below the water surface. After the laser shock process, the remained sacrificial layer on the sample was removed carefully with acetone, and then cleaned with IPA and deionized water. Zygo NewView 8000 optical profiling system was used to monitor the surface profile before and after LS-µF process. SEM (JSM6510 Scanning electron microscope) images were also observed for more detailed surface profile results.

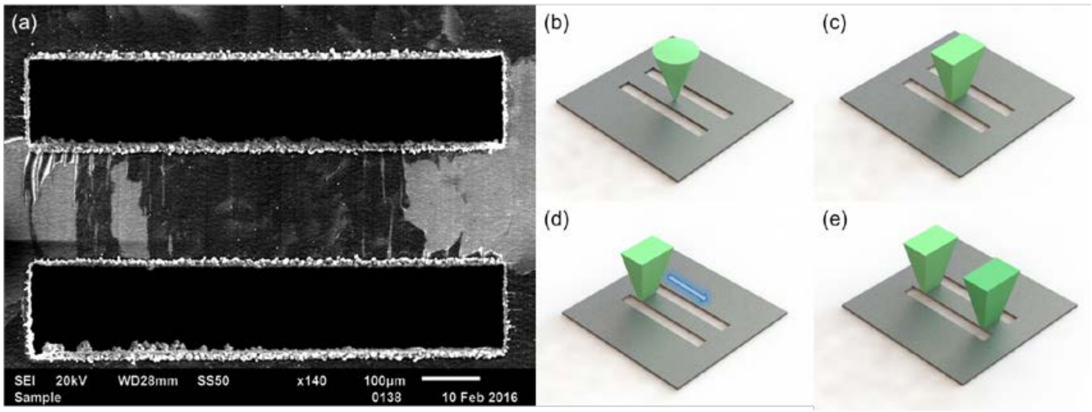

Figure 44 (a) An SEM image of the tested metal sample. LS-µF using various laser beam profile: (b) Gaussian beam, (c) bar-shaped beam, (d) two bar-shaped beams were first projected on the left part then right part of the metal surface, (e) two bar-shaped laser beams were simultaneously projected onto the sample surface.

Two sets of experiments were carried out. They are schematically depicted in Fig. 44b-e. The first set of experiments study effects of laser beam profiles on the shockwave generations and resulted deformations. In this experiment (Fig. 44b-c), a SLM-shaped laser beam was compared with a Gaussian beam. The second set of experiments study laser shock micro-forming using multiple laser beams generated by the SLM. In this experiment (Fig. 44d-e), two rectangular shape beams were simultaneously projected on free standing structures. The micro-forming results were the compared with one shaped laser beam with the same beam energy projected on the same locations sequentially.

4.2.2.1 SLM-Shaped Laser Beam Shock Micro-Forming

To study effects of laser beam profiles to the outcome laser-induced deformation on MEMS structures, comparative experiments were carried out. The laser micro-forming experiment was first carried out using an unshaped laser beam while the output from the frequency-double YAG laser was directly focused onto the surface of the free-standing structures as depicted in Fig. 44b-c. In this experiment, the pulse laser was focused on-target using a fused silica convex lens with a focal distance of 20 cm. The focal size (FWHM) was estimated to be ~10 μm in diameter. The on-target pulse energy is 0.3 mJ. The laser-induced deformation was then examined using SEM as shown in Fig. 45a. The shockwave deforms the entire bridge. The largest deformation, which is located at the focal point of the laser, was measured as 50 μm below the original location. The profile of the laser-induced deformation is presented in Fig. 45b. Although the depth of laser-induced deformation can be changed by the laser pulse energy as shown in Fig. 45b, the profile of the laser-induced deformation remains the same. The other important feature of the laser-induced deformation exerted by the Gaussian beam profile is the non-uniformity across the width of the bridge around the focal spot. This is evident in zoom-in SEM photo shown in Fig. 45c. Although the laser excited shockwave induce deformation with sizes many times larger than that of the laser focal size (10 μm), the Gaussian energy profile still produce a circular deformation around the laser focal spot. An atomic force microscope was used to study the surface morphology across the laser focal spot. It reveals similar surface morphology to those area receiving no laser irradiation. This suggests that the crate shape shown in Fig. 45c was induced by mechanic deformation rather than laser ablation or the laser melting. Using an optical profilometer (Zygo NewView 8000), 3D surface image of the deformed region in the freestanding bridge is presented in Fig. 45d. The FWHM of this circular deformed region was measured as 80 μm, about ×8 times larger than that the laser focal spot.

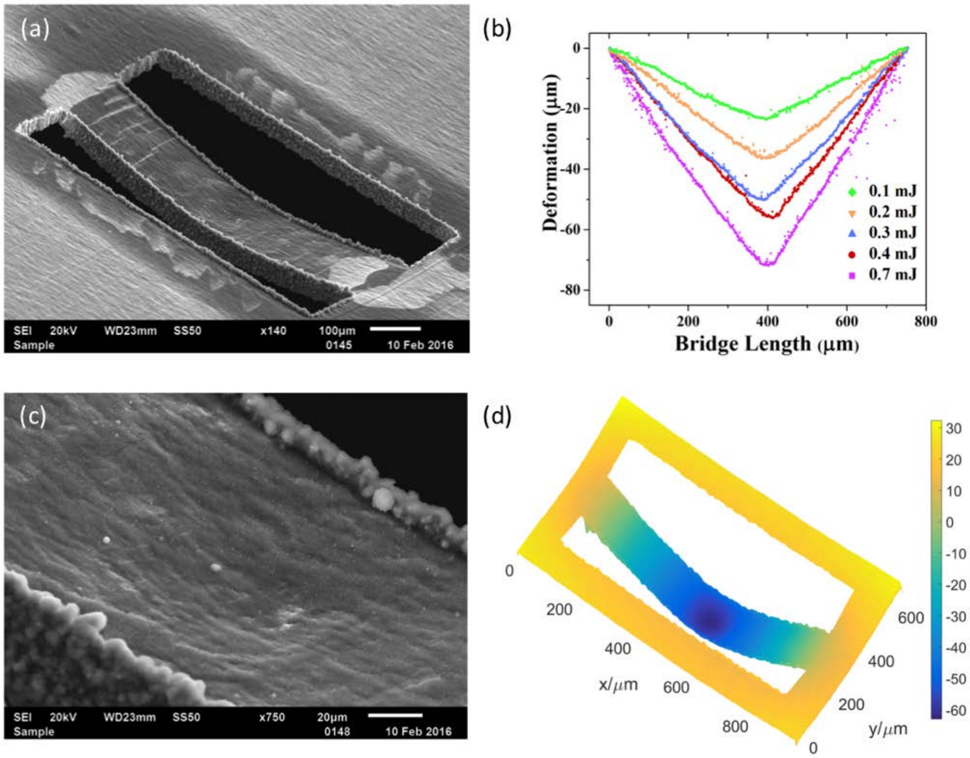

Figure 45 (a) Birdview SEM images of laser micro-formed free-standing bridge structures by a Gaussian laser beam, (b) the deformation depth vs. on-target laser energy using the Gaussian laser beam, (c) the close-up image around laser-impact region, and (d) 3D surface profile plot of the deformed bridge by the Gaussian beam.

Results presented in Fig. 45 reveal limitation of the laser shock micro-forming using Gaussian beams at micrometer scale. When the feature size is comparable to sizes of the laser-shock induced mechanic deformations, the processing non-uniformity due to the non-uniformed laser energy distribution becomes significant. This is evidently shown in Fig. 45c-d. To improve the laser shock processing uniformity at micron scales. A SLM-shaped laser beam was used to generate shockwave. Using the SLM laser projection system, a rectangular laser beam profile with sizes of 10 µm × 125 µm was projected onto free-standing structures to generate shockwave. Even the laser intensity distribution inside the shaped laser beam might not be uniform, the shaped laser beam produces significant improvements in deformation uniformity.

A laser-deformed freestanding structure is shown in Fig. 46a. This feature was produced by a SLM-shaped laser pulse with on-target energy of 0.3 mJ, which is the same as what used to produce results in Fig. 45 using a Gaussian beam. The maximum deformation produced by the shaped laser beam was measured by the optical surface profilometer as 24-μm, this is about half of what was achieved using a focused Gaussian laser beam presented in Fig. 45a-b. This is probably due to the on-target area of the shaped laser beam is much larger (>10 times). The recoil pressure induced by the laser ablation will become weaker. Fig. 46b shows the deformation profiles across the length of the freestanding bridge produced by a single shaped laser pulse with 0.1, 0.2, 0.3, 0.4 and 0.7 mJ, respective. Along the length of the free-standing bridge, the deformation profiles deformed by the SLM-shaped beam produce similar deformation profiles to those produced by the Gaussian beam as shown in Fig. 45b. However, along the width of the bridge, the shaped laser beam produced much more uniform deformation. This is shown in a zoom-in SEM picture Fig. 46c. Surface profile measurement results is presented in the inset of Fig. 46d. Both reveal a uniform deformation across the 125 μm width of the bridge. Fig. 46d compares the deformation profiles produced by the shaped laser beam and an unshaped Gaussian beam with identical on-target pulse energy of 0.3 mJ. The crate depth produced by the Gaussian beam exceeds 12 μm. While the SLM-shaped laser beam yield far less surface height variation ~2.2 μm.

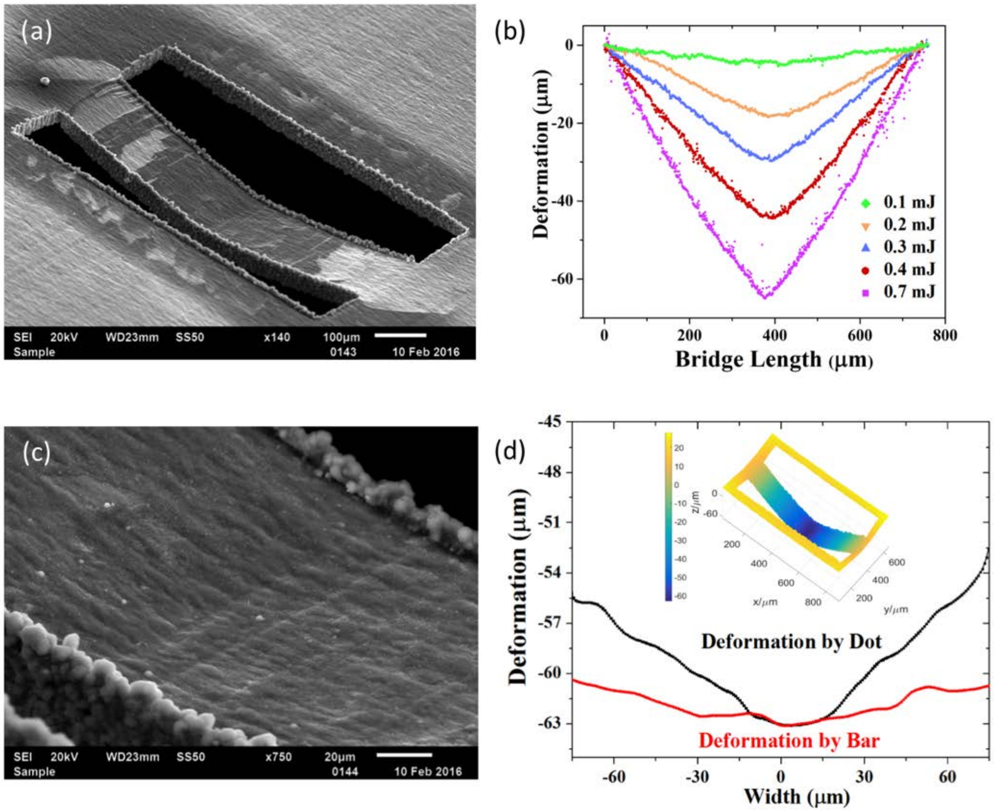

Figure 46 (a) Birdview SEM images of laser micro-formed free-standing bridge structures by a rectangular-shape laser beam, (b) the deformation depth vs. on-target laser energy using the shaped laser beam, (c) the close-upimage around laser-impact region, (d) surface profile measurements along the width of the free-standing bridge using a Gaussian beam and a shaped laser beam. The 3D surface profile plot of the deformed bridge by the shaped laser beam is shown as insert.

The effect of number of repeated pulses was studied first. The pulse energy chosen here was 0.3 mJ/pulse and the focused pulse shaped was about 10 µm in diameter for single dot beam, and 10 µm by 125 µm for bar-shape beam. The crater depth was plot as a function of number of laser pulses, as shown in Fig. 47a. The crater depth increased with the number of laser pulses. We can also see that the initial pulses have larger bending effect compared with later pulse. This agrees with previous study [102].

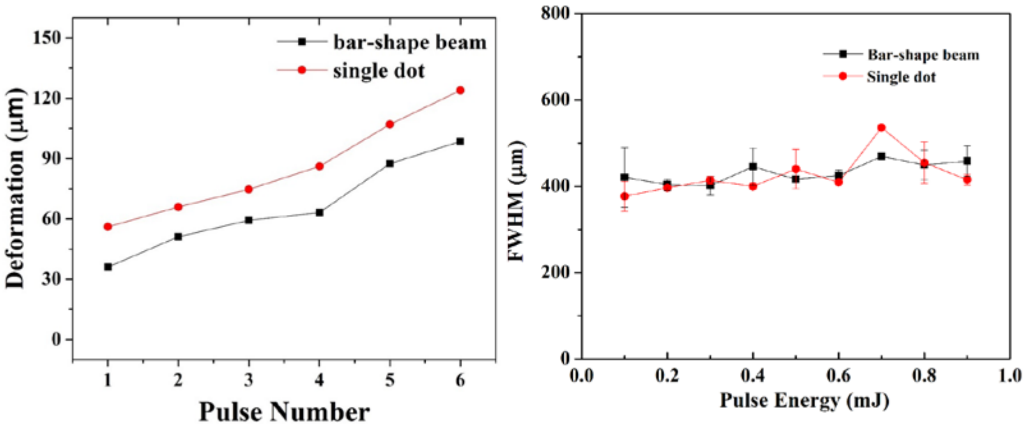

Figure 47 (a) Relationship between laser-induced deformation FWHM value and laser pulser energy. (b) Laser-induced deformation depth vs. pulse numbers using 0.4 mJ pulse energy.

The relationship between bending deformation on metal sheet and laser pulse energy was also studied in detail. We were using the same beam shapes but with different laser pulse energies: ramping up from 0.1 mJ/pulse to 0.9 mJ/pulse. The result is given in Fig. 47b, the depth of the dent formed by laser induced shockwave increases as the pulse energy goes higher, while the full width at half maximum (FWHM) of the dent almost maintains the same value.

4.2.2.2 Shockwave Simultaneously Induced by Multiple Laser Beams

One main drawback in conventional LSF process is lacking of parallelism. In other words, it is a point-by-point laser processing scheme, which not only slows down the whole forming process, but also possibly reduces precision in certain applications. When two points are overlapped or closely contacted with each other, the plastically deformation generated by the first laser pulse will affect the bending result caused by the second pulse [115]. This defect can be reduced by program controlling the energy of each laser pulse, but it also increases the cost and system complexity. However, a SLM can simultaneously generate multiple laser beams to deform several working areas at once. To determine how parallel laser processing works, the same metal bridge introduced in former sections was bent in two different experimental environments. The first bridge was firstly shocked on its left part by a 10 µm x 125 µm bar-shape laser beam generated by SLM, and then a same shock on the right part. The distance between these two bars was controlled by SLM. On the second step, the SLM was programed to shape the laser beam profile into two bars with same size and same separation as applied in first bridge, and use it to bend the metal bridge. The laser pulse energy was maintained as 0.2 mJ in the first situation and 0.4 mJ in the second experiment, so that the two experiments had same total on target pulse energy. The 1D profile scan result for the cross section of the bridge is given in Fig. 48b, and the optical surface profiling results are shown in Fig. 48a.

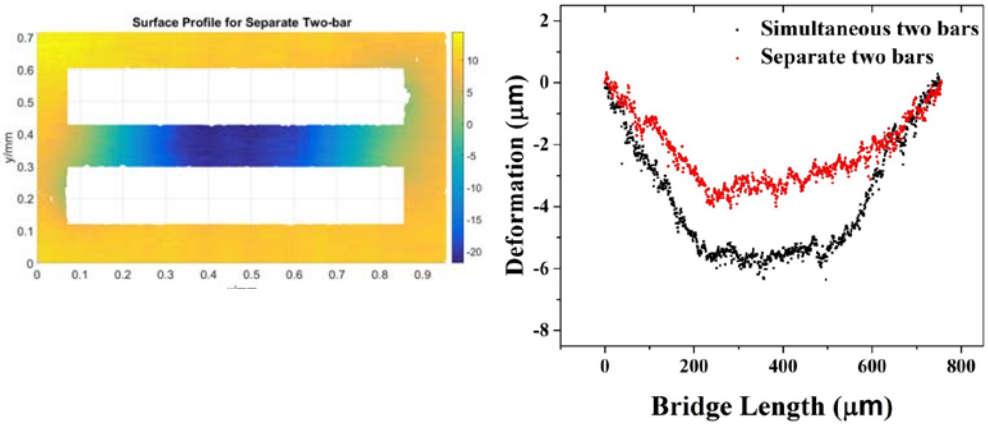

Figure 48 (a) Surface profile of the free-standing bridge simultaneously deformed by two laser bars. The spacing between two laser bars is 324 µm. (b) 1D surface profile of free-standing bridge deformed by simultaneous two bars and separate two bars.

It is interesting to see that a flatter and more uniform surface profile is reached when the bridge is shocked by simultaneous two bars. Additionally, the drawback in traditional LSF is also shown in Fig. 48. Since the left part of the bridge got shocked at first, the deformation in that area was larger compared with the right part, which was shocked a few seconds later.

Previous research work [116] shows that shockwaves generated by simultaneously multiple laser beams can be accumulated with each other if they are close enough and increase the pressure at the intersection. From Fig. 48, we can tell that even the total on target pulse energy were the same, simultaneous two-bar shaped beam formed deeper dents compared with separate two bar shape beams.

4.3 Laser Shock Peening with Real-Time Distributed Strain Sensing

As described in previous chapters, despite laser additive manufacturing is a promising tool in fabrication process, the product suffers from fatigue strength problems like tensile residual stress, micro-cracks, and porous microstructures, which may be improved by post heating treatment or mechanical treatment [117-121]. Sharing very similar working principles with laser shock forming, Laser shock peening (LSP) is a widely used laser processing method in industrial areas to enhance mechanical properties of the metal specimens. However, compared with laser shock forming, LSP usually involves much higher laser pulse energy, so the previously introduced adaptive laser processing method is no longer available due to the low damage threshold of the SLM. In this section, we are going to introduce a real-time distributed strain monitoring system for metal LSP applications with embedded fiber optic sensors.

4.3.1 Sample Preparation and Experiment Setup

An IN718 cantilever beam with pre-designed shallow groove (1.25 mm in width and 1.5 mm in depth) was 3D printed through DMLS to serve as the substrate for the LSP experiment, as shown in Fig. 49. The same nickel electroplating process and fiber sensor embedding method mentioned in Chapter 2 and 3 was applied to fabricate a sensor embedded cantilever beam. The Cu1300 copper-coated single mode fiber was nickel electroplated to form a 10 cm long and 400 µm thick protective coating as shown in Fig. 49a. The electroplated fiber was then inserted into the groove on the 3D-printed cantilever beam and its two ends were fixed by copper tapes. The whole component was then transferred to the LENS chamber and deposited with two layers of IN718 powder with the same printing parameters given in Table 2, as shown in Fig. 49b,c. The final product is an IN718 cantilever beam with embedded optical fiber sensor which is fully covered by around 1.5 mm thick metal powder layer. Further mechanical test was performed to this sensor embedded part to evaluate its sensing capability in strain measurement.

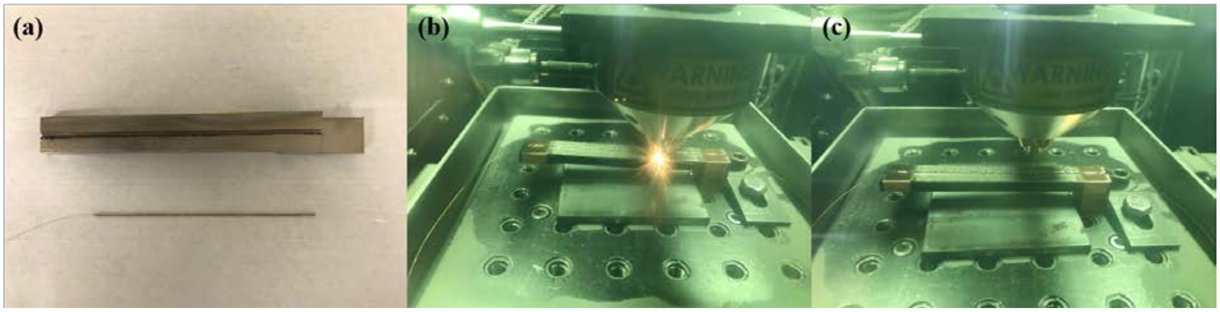

Figure 49 (a) Nickel electroplated optical fiber sensor and a 3D-printed cantilever beam with IN718 powder using DMLS technique. (b) Embedding the fiber sensor through LENS. (c) The optical fiber sensor was fully embedded into the cantilever beam after two layers of deposition.

4.3.2 Cantilever Beam Strain Calibration Test

Similar as in Section 3.5, in order to verify the strain sensing capability of the sensor embedded cantilever beam, a standard static test was performed to calibrate the smart component. As illustrated in the FEA model shown in Fig. 50, one end of the cantilever beam was clamped onto an optical table through two bolts, while loads ranging from 32 N to 160 N were applied perpendicularly to the other end of the cantilever beam. The strain distribution along the embedded fiber optic sensor under different loads was measured through OBR. The applied loads were then removed to confirm the whole structure could be restored to its original condition, so that the sensor embedded cantilever beam can provide reliable and accurate strain distribution in measurement.

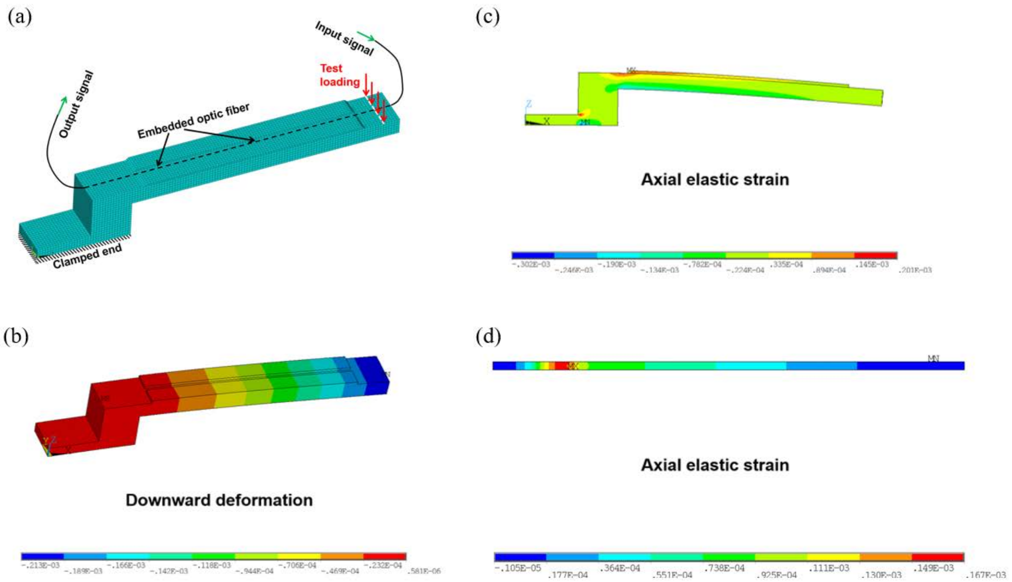

Figure 50 (a) A FEA model of the the sensor embedded cantilever beam. (b) Downward deformation of the whole structure after the 3D-printing process. (c) The cross-section view of the axial elastic strain mapping. (d) The axial elastic strain distribution along the embedded optical fiber.

As a representative of the whole process, the elastic strain distribution in the sensor embedded cantilever beam under 32 N load was simulated using FEA simulation program (ANSYS v17.2). After applying the 32 N load at the right end of the cantilever beam, the downward deformation of the whole structure is simulated using FEA shown in Fig. 50b. The largest deformation is -0.213 mm located at the right end of the cantilever beam, while the left side near the fixtures shows little deformation. A cross-section view of the axial elastic strain along the length direction of the cantilever beam is given in Fig. 50c. While Fig. 50d shows the bird-view of the elastic strain distribution along the long axis of the metal component, it can be observed that at the left side of the cantilever beam, the elastic strain first increased sharply to the left edge of the deposited metal powder block, before a smooth drop till the right end of the cantilever beam. Fig. 51 gives further quantitative analysis of the FEA simulation during the whole process, Fig. 51a shows the 3D elastic strain mapping of the whole structure, with a maximum value of 199 με near the left edge of the deposited IN718 powder layer and a minimum of -206 με located at the bottom left part of the cantilever beam. A zoomed-in cross-section view of the elastic strain mapping is shown in Fig. 51b, where the dashed line represents the embedded fiber optic sensor. Considering the 1.5 mm thick metal powder deposition and 400 μm Nickel protective coating, we subtract a 1-D strain distribution 1.9 mm beneath the surface of the component, as shown in the plot in Fig. 51b. According to the infinitesimal strain theory, among the embedded optical fiber section, the elastic strain drops linearly as the position moves towards the right end of the cantilever beam, and the slope of this strain-position curve is around -0.667 μm/cm.

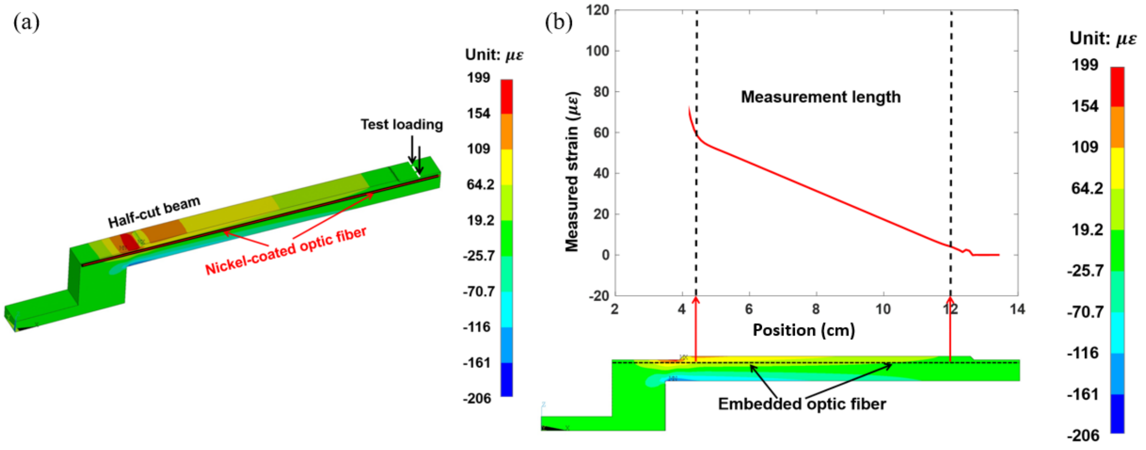

Figure 51 (a) The elastic strain mapping of the cantilever beam in the bending test with 32 N load. (b) A zoom-in elastic strain distribution along the fiber sensor.

Besides the FEA mechanical simulation, the experimental data of strain distribution along the embedded optical fiber was also captured through OBR during the static test. The 1-D elastic strain mapping in the loading and unloading process are given in Fig. 52. In general, the strain plot shows a sharp rise from the input end of the embedded optical fiber to the left edge of the deposited powder block, following by an almost linear decrease in strain till the fiber output. This linear drop is supported by the infinitesimal strain theory that under small displacement condition, the non-linear and second-order terms of the finite strain tensor are neglectable, the infinitesimal strain tensor ε is linear. In general, these strain curves show nearly perfect match to the FEA simulation results using ANSYS. In the loading process, generally the magnitude of the elastic strain shows an increasing trend while the applied load raised from 32 N to 160 N. However, at lower loads the curve is much smoother compared with relatively more fluctuating curves at higher loads, especially for the points at 20 mm, 30 mm, and 50 mm. This is possibly due to the defects like pores and micro cracks induced during the metal additive manufacturing process, which later causing micro bending on the embedded optical fiber sensor. This phenomenon becomes more significant in the unloading process: there is a sharp valley on the strain curve located at the 45 mm point when the applied load is 128 N and 96 N. Nonetheless, when all loads were removed, the purple curve in Fig. 52b shows that except slight shift between 15 mm and 25 mm region, the elastic strain distribution almost returned back to near zero after this loading-unloading process, which means the embedded fiber optic sensor survived under the manufacturing and testing process, and it is capable to perform reliable and repeated measurement.

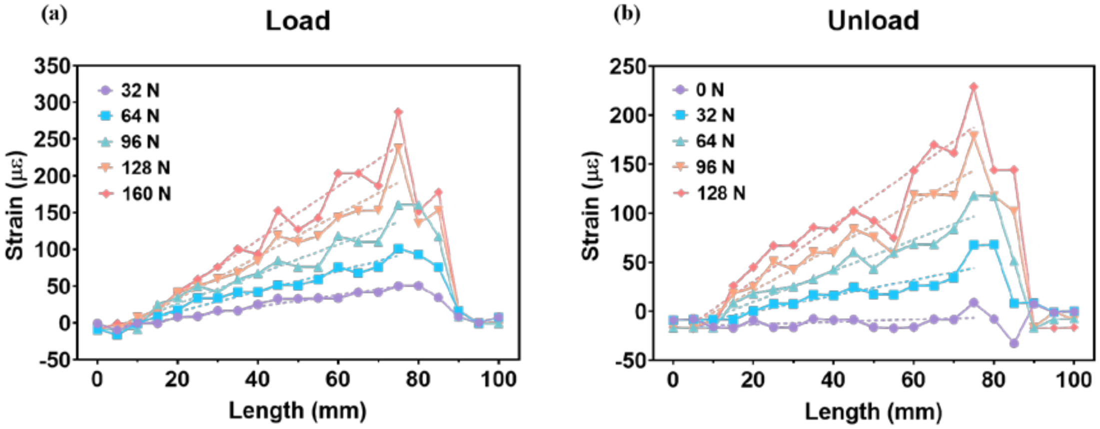

Figure 52 The axial elastic strain profile along the embedded optical fiber under various loads during the (a) loading and (b) unloading process.

To further analyze the elastic strain in the cantilever beam, linear fitting was performed to the dropping section of the strain curve as shown in the dashed lines in Fig. 52. The slope of each fitting curve was measured and given in Fig. 53. It can be observed that there is a linear relationship between the slope and the force of the applied load. This proves that the strain measured by the embedded fiber optic sensors are elastic strain instead of residual plastic strain.

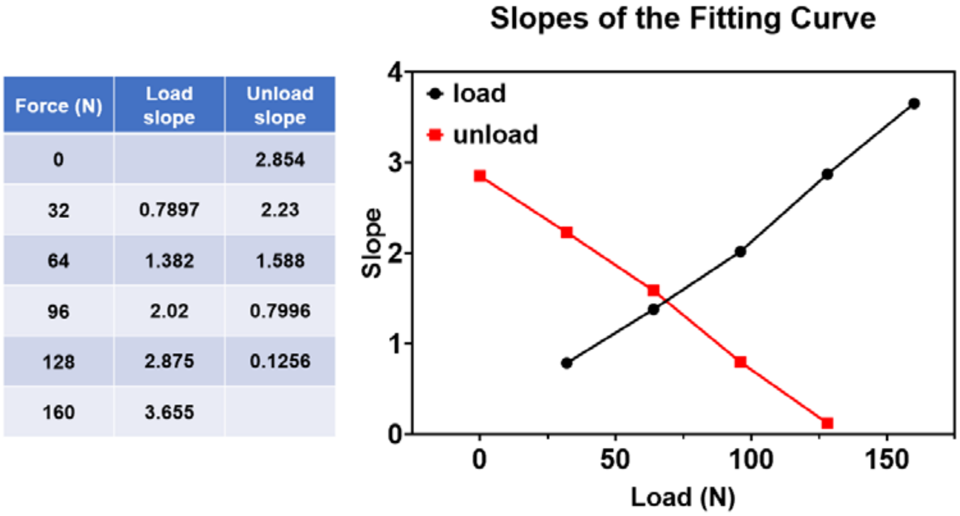

Force (N)	Load slope	Unload slope
0		2.854
32	0.7897	2.23
64	1.382	1.588
96	2.02	0.7996
128	2.875	0.1256
160	3.655	

Figure 53 The slope of the linear fitting curve of the strain distribution.

The static test proves that our embedded optical fiber sensor can support reliable and accurate distributed strain measurement with high spatial resolution.

4.3.3 Real-Time Monitoring in Laser Shock Peening Process

After the standard static test, the sensor embedded cantilever beam was first covered by a thin layer of black tape with 177 μm thickness as the sacrificial layer to avoid direct ablation from the high-power laser pulse. Then the sample was carefully mount on a motion stage and covered by a flowing water layer to confine the laser induced shockwave as shown in Fig. 54.

(a) (b)

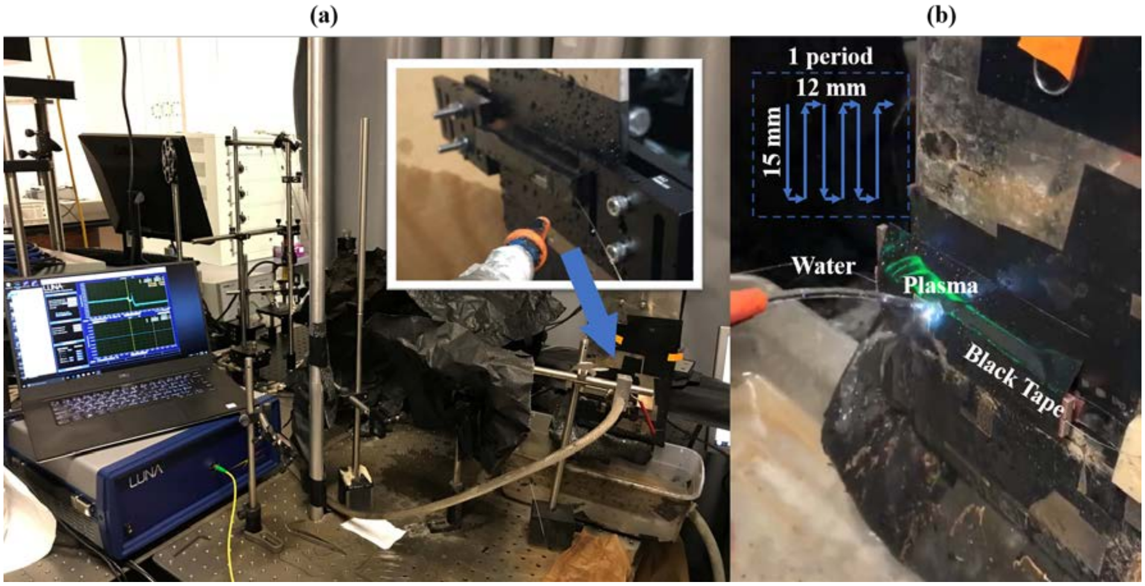

Figure 54 (a) The experimental setup of the LSP test. (b) A zoom-in photo of the tested sample during the LSP process.

To achieve optimal laser shock peening performance, we chose the highest laser pulse energy. A more detailed laser parameter used in the LSP process is given in Table 4.

Table 4 Parameters for the laser applied in the LSP process

Wavelength (nm)	1064
Beam Profile	Gaussian Beam
Pulse Energy (mJ)	850
Pulse Width (ns)	7
Repetition Rate (Hz)	10
On-target Beam Diameter (mm)	1
Overlap Ratio	50%
Number of Scans	1

The fixed sample was moved with the motion stage following a zig-zag scanning path, so that the laser pulses can cover the whole cantilever beam, as shown in Fig. 54. The embedded optical fiber sensor was connected to the OBR to measure the real-time strain change during the laser shock peening process. Because OBR is sensitive with vibration, it is very difficult to perform measurement when the stage was moving. So, we divided the whole scanning path into 6 periods with each period covered 15 mm x 12 mm area, as shown in Fig. 54b. After scanning one period, the motion stage was paused and a residual strain measurement was performed using OBR. A FEA mechanical simulation of the laser shock peening process was also performed using ANSYS to simulate the evolution of the strain distribution along the tested cantilever beam. A more detailed discussion is given in the next section.

4.3.4 Results and Discussion

The residual strain distribution of the cantilever beam after each laser shock peening period were measured and calculated as shown in Fig. 55. In general, the measured residual strain were mostly negative values along the whole tested area, which means compressive strain. These experimental results agree with early studies that laser shock peening induces compressive stress to the metal part. The plot also shows that after each laser shock peening period, the maximum residual strain increased constantly from -20 με in the first period to -200 με in the sixth period. For the first three periods, the left part of the cantilever beam shows higher residual strain than the right part; while in the 4th and 5th period, more residual strain is accumulated in the right part of the cantilever beam. After all six periods, the strain distribution shows a general “U shape” with a relatively flat bottom from 1.5 cm to 5 cm with an average -160 με compressive strain.

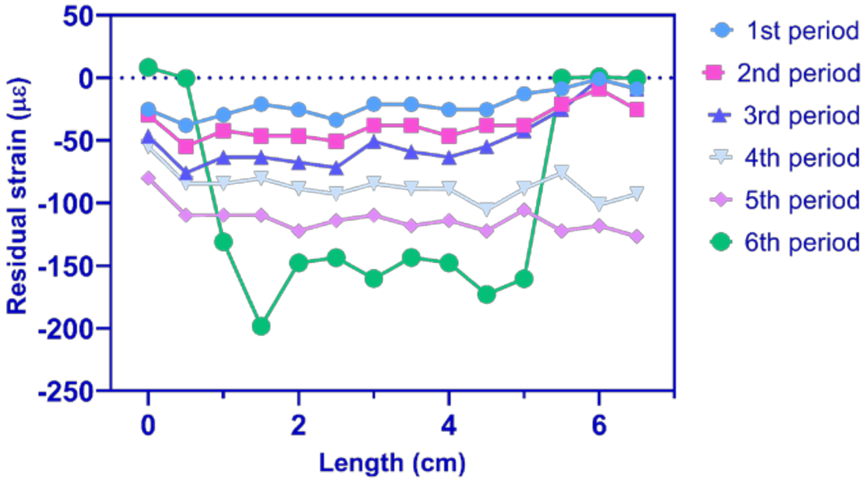

Figure 55 strain distribution of each laser shock peening period

A mechanical simulation was performed using ANSYS to simulate the residual strain evolution during the laser shock peening process, as shown in Fig. 56. The simulation results show that as laser shock peening applied to the metal component, compressive strain was generated along the fiber sensor embedded area, with the maximum value increased constantly and moving from left part of the cantilever beam to the center part, as summarized in Table 5. The simulation results generally agree with our experimental ones in magnitude.

Table 5 Simulated maximum compressive strain in each period

Period	Max compressive strain (με)	Location (cm)
1	13.2	0.5
2	37.5	1.2
3	64.0	2.0
4	82.1	2.7
5	110.6	3.0
6	130.4	3.2

These strain tests prove that the embedded optic fiber sensor may be a useful tool to provide distributed strain measurement in real-time for metal components during laser processing applications.

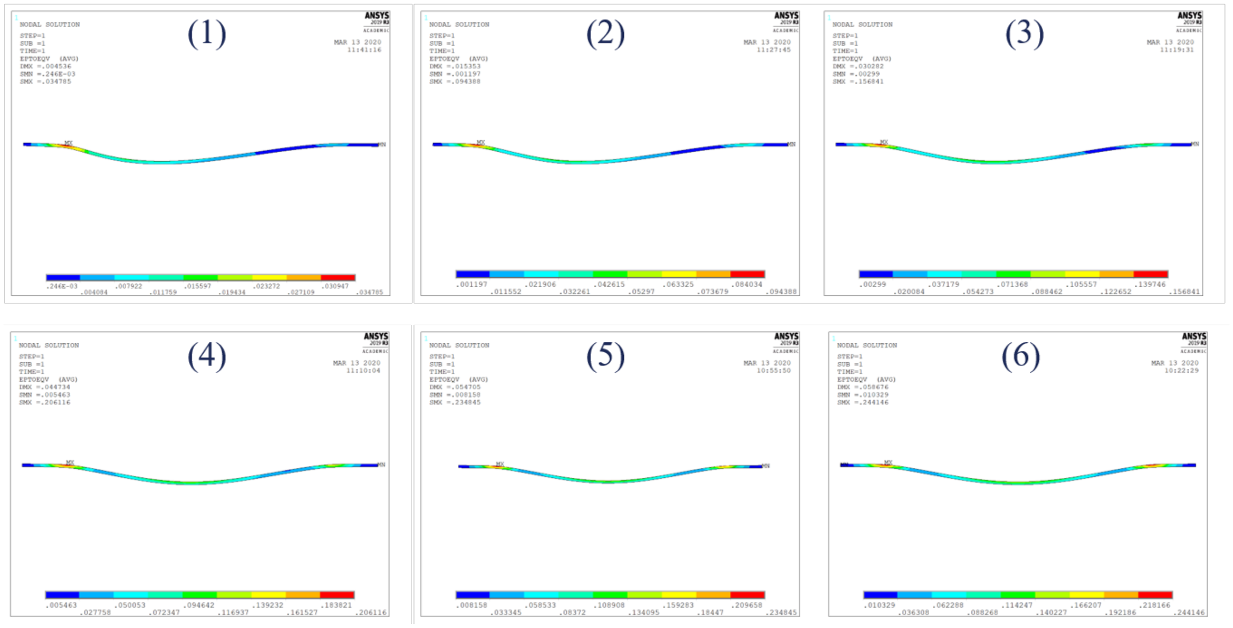

Figure 56 Mechanical simulation of residual strain distribution along the cantilever beam during the laser shock peening process.

5.0 Summary

The work presented in this dissertation includes the investigations on both simulation and experiment of the embedded distributed fiber sensors for measuring strain and temperature profiles of 3D printed metal components.

Chapter 2 focuses on establishing a theoretical model of the stresses induced during deposition and using the model to obtain parameters related to following experiments. In addition, the residual strains measured by the fiber sensors quantitatively agreed with the stress simulations, which laid a good foundation for reducing or mitigating residual strain during or following the manufacturing process.

Chapter 3 focuses on the procedures for embedding pre-shaped optical fiber sensors into 3D AM applications. Firstly, we successfully embedded the optical fiber sensors into curved surface, like a 3D printed Ti-6Al-4V turbine blade, which also indicates that we can monitor the distributed strain and temperature change in the 3D printing process in real-time. Moreover, the distributed strain along the embedded fiber sensor was measured and analyzed. The results shows that the distributed elastic strain along the embedded fiber sensor was increased when more load. Using a Rayleigh-scattering optical frequency domain reflectometer, temperature evolutions of the LENS deposition process were monitored with 5 mm spatial resolution. Residual strains were measured by the embedded fiber sensors with 5 mm spatial resolutions. Temperatures and strain profiles of the LENS deposition process were also modeled by conducting a transient thermomechanical finite element analysis. Discrepancy between temperature and strain profiles measured by embedded distributed fiber sensors and simulation results are less than 10%.

Chapter 4 focuses on the self-designed adaptive optical technique for laser shock micro-forming and laser shock peening for real-time distributed strain sensing in 3D MEMS Device Fabrication. In laser shock micro-forming process, spatial light modulator assisted adaptive laser shock micro forming are presented as an efficient and high throughput method to enhance surface qualities and to improve geometric shape accuracy for microscale fabrication. This work will first explore the rectangular beam shapes with different aspect ratios. The results presented in this chapter show that the adaptive-optics laser beam forming is an effective and flexible method to generate shockwave with various shapes and sizes of wavefront and at multiple locations for laser processing at microscales. In laser shock peening process, experimental and simulation results of the real-time distributed strain monitoring system for metal LSP applications with embedded fiber optic sensors were discussed. They show that fiber sensing is a powerful tool for smart components fabrication via additive manufacturing. The proposed framework can be further developed into a stable in-situ sensing tool which has great potential in monitoring the distributed strain evolutions in real-time during metal AM processing.

In the future work, real-time strain measurement at high temperature immediately after a thin strip/layer is deposited can be employed as input for optimizing the laser scanning strategy. As a result, the real-time feedback from the printer control system may adjust process parameters like laser power and scanning velocity so that the residual stress/distortion of the metal components can be mitigated at last, as a great benefit of the temperature/strain fiber sensors.

Bibliography

1. Chin, R., J. Beuth, and C. Amon. *Control of residual thermal stresses in shape deposition manufacturing*. in *Proceedings of the Solid Freeform Fabrication Symposium, Austin, TX, Aug*. 1995.

2. Gifford, D.K., et al. *Distributed fiber-optic temperature sensing using Rayleigh backscatter*. in *Optical Communication, 2005. ECOC 2005. 31st European Conference on*. 2005. IET.

3. Yan, A., et al., *Distributed Optical Fiber Sensors with Ultrafast Laser Enhanced Rayleigh Backscattering Profiles for Real-Time Monitoring of Solid Oxide Fuel Cell Operations.* 2017. **7**(1): p. 9360.

4. Zaghloul, M.A., et al., *High Spatial Resolution Radiation Detection Using Distributed Fiber Sensing Technique.* 2017. **64**(9): p. 2569-2577.

5. Yan, A., et al., *Sapphire fiber optical hydrogen sensors for high-temperature environments.* 2016. **28**(1): p. 47-50.

6. Li, S., et al. *3D temperature mapping of cellular passive cooling structures fabricated by additive manufacturing for lasers*. in *CLEO: Science and Innovations*. 2017. Optical Society of America.

7. Wang, M., et al. *Ultrafast Laser Enhanced Rayleigh Backscattering on Silica Fiber for Distributed Sensing under Harsh Environment*. in *CLEO: Applications and Technology*. 2018. Optical Society of America.

8. Gunes, O., *Failure modes in structural applications of fiber-reinforced polymer (FRP) composites and their prevention*, in *Developments in Fiber-Reinforced Polymer (FRP) Composites for Civil Engineering*. 2013, Elsevier. p. 115-147.

9. Di Sante, R., *Fibre optic sensors for structural health monitoring of aircraft composite structures: Recent advances and applications.* Sensors, 2015. **15**(8): p. 18666-18713.

10. Culshaw, B. and A. Kersey, *Fiber-optic sensing: A historical perspective.* Journal of lightwave technology, 2008. **26**(9): p. 1064-1078.

11. Ghetia, S., R. Gajjar, and P. Trivedi, *Classification of fiber optical sensors.* Int. J. Electron. Commun. Comput. Technol, 2013. **3**: p. 442-445.

12. Zhang, L., J. Lou, and L. Tong, *Micro/nanofiber optical sensors.* Photonic Sensors, 2011. **1**(1): p. 31-42.

13. Kirkendall, C.K. and A. Dandridge, *Overview of high performance fibre-optic sensing.* Journal of Physics D: Applied Physics, 2004. **37**(18): p. R197.

14. Udd, E. *A personal tour of the fiber optic Sagnac interferometer*. in *Fiber Optic Sensors and Applications VI*. 2009. International Society for Optics and Photonics.

15. LEFÈRE, H.C., *Fundamentals of the interferometric fiber-optic gyroscope.* Optical review, 1997. **4**(1A): p. 20-27.

16. Rao, Y.-J. *Recent advances in fiber-optic FP interferometric sensors*. in *Fundamental Problems of Optoelectronics and Microelectronics III*. 2007. International Society for Optics and Photonics.

17. Wang, L. and N. Fang, *Applications of fiber-optic interferometry technology in sensor fields*, in *Optical Interferometry*. 2017, InTech.

18. Hariharan, P., *Basics of interferometry*. 2010: Elsevier.

19. Udd, E. and W.B. Spillman Jr, *Fiber optic sensors: an introduction for engineers and scientists*. 2011: John Wiley & Sons.

20. Yin, S., P.B. Ruffin, and F.T.S. Yu, *Fiber Optic Sensors*. 2017: CRC Press.

21. Wan, X. and H.F. Taylor, *Intrinsic fiber Fabry–Perot temperature sensor with fiber Bragg grating mirrors.* Optics letters, 2002. **27**(16): p. 1388-1390.

22. Chin, K.K., et al., *Fabry-Perot diaphragm fiber-optic sensor.* Applied optics, 2007. **46**(31): p. 7614-7619.

23. Cibula, E. and D. Đonlagić, *Miniature fiber-optic pressure sensor with a polymer diaphragm.* Applied optics, 2005. **44**(14): p. 2736-2744.

24. Wada, A., S. Tanaka, and N. Takahashi. *High-sensitivity vibration sensing using in-fiber Fabry-Perot interferometer with fiber-Bragg-grating reflectors*. in *20th International Conference on Optical Fibre Sensors*. 2009. International Society for Optics and Photonics.

25. Dong, B., M. Han, and A. Wang. *Two-wavelength quadrature multipoint detection of partial discharge in power transformers using fiber Fabry-Perot acoustic sensors*. in *Fiber Optic Sensors and Applications IX*. 2012. International Society for Optics and Photonics.

26. Wolthuis, R.A., et al., *Development of medical pressure and temperature sensors employing optical spectrum modulation.* IEEE Transactions on Biomedical Engineering, 1991. **38**(10): p. 974-981.

27. Mitschke, F., *Fiber-optic sensor for humidity*. Optics letters, 1989. **14**(17): p. 967-969.

28. Beard, P. and T. Mills, *Miniature optical fibre ultrasonic hydrophone using a Fabry-Perot polymer film interferometer.* Electronics Letters, 1997. **33**(9): p. 801-803.

29. Beard, P. and T. Mills, *Extrinsic optical-fiber ultrasound sensor using a thin polymer film as a low-finesse Fabry–Perot interferometer.* Applied optics, 1996. **35**(4): p. 663-675.

30. Murphy, K.A., et al., *Quadrature phase-shifted, extrinsic Fabry–Perot optical fiber sensors.* Optics letters, 1991. **16**(4): p. 273-275.

31. Sirkis, J., et al., *In-line fiber etalon (ILFE) fiber-optic strain sensors.* Journal of lightwave technology, 1995. **13**(7): p. 1256-1263.

32. Culshaw, B., *Fiber optics in sensing and measurement.* IEEE Journal of selected topics in quantum electronics, 2000. **6**(6): p. 1014-1021.

33. Udd, E. *Fiber-optic acoustic sensor based on the Sagnac interferometer*. in *Single Mode Optical Fibers*. 1983. International Society for Optics and Photonics.

34. Rajkumar, N., V.J. Kumar, and P. Sankaran, *Fiber sensor for the simultaneous measurement of current and voltage in a high-voltage system.* Applied optics, 1993. **32**(7): p. 1225-1228.

35. López-Higuera, J.M., *Handbook of Optical Fibre Sensing Technology*. 2002: Wiley.

36. Hill, K., et al., *Photosensitivity in optical fiber waveguides: Application to reflection filter fabrication.* Applied physics letters, 1978. **32**(10): p. 647-649.

37. Meltz, G., W.W. Morey, and W. Glenn, *Formation of Bragg gratings in optical fibers by a transverse holographic method.* Optics letters, 1989. **14**(15): p. 823-825.

38. Poumellec, B., et al., *The UV-induced refractive index grating in Ge: preforms: additional CW experiments and the macroscopic origin of the change in index.* Journal of Physics D: Applied Physics, 1996. **29**(7): p. 1842.

39. Lemaire, P., R. Atkins, and V. Mizrahi, *WA; Reed. High pressure h2 loading as a technique for achieving ultrahigh uv photosensitivity and thermal sensitivity in geo2 doped optical fibres.* Electronic Letters. **29**.

40. Xu, M.G., et al., *Optical in-fibre grating high pressure sensor.* Electronics Letters, 1993. **29**(4): p. 2.

41. Morey, W., *Evaluation of a fiber Bragg grating hydrostatic pressure sensor.* Proc. OFS8, Moneterey, USA, Post-Deadline Session, 1982.

42. LeBlanc, M., et al., *Transverse load sensing by use of pi-phase-shifted fiber Bragg gratings.* Optics letters, 1999. **24**(16): p. 1091-1093.

43. Gander, M., et al., *Bend measurement using Bragg gratings in multicore fibre.* Electronics Letters, 2000. **36**(2): p. 120-121.

44. Hathaway, M., et al., *Combined ultrasound and temperature sensor using a fibre Bragg grating.* Optics communications, 1999. **171**(4-6): p. 225-231.

45. Berkoff, T. and A. Kersey, *Experimental demonstration of a fiber Bragg grating accelerometer.* IEEE Photonics Technology Letters, 1996. **8**(12): p. 1677-1679.

46. Ogawa, Y., J.-i. Iwasaki, and K. Nakamura. *A Multiplexing LoadMonitoring System of Power Transmission Lines using FiberBragg Grating*. in *Optical Fiber Sensors*. 1997. Optical Society of America.

47. Henderson, P., N. Fisher, and D. Jackson. *Current metering using fibre-grating based interrogation of a conventional current transformer*. in *Optical Fiber Sensors*. 1997. Optical Society of America.

48. Kersey, A.D. and M.J. Marrone. *Fiber Bragg grating high-magnetic-field probe*. in *Tenth International Conference on Optical Fibre Sensors*. 1994. International Society for Optics and Photonics.

49. Yang, Y., et al. *Characterization of fiber Bragg grating based Palladium tube hydrogen sensors*. in *Proc. Conf. Smart Structures and Materials*.

50. Meltz, G., S.J. Hewlett, and J.D. Love. *Fiber grating evanescent-wave sensors*. in *Chemical, Biochemical, and Environmental Fiber Sensors VIII*. 1996. International Society for Optics and Photonics.

51. Ecke, W., et al. *Chemical Bragg grating sensor network based on side-polished optical fiber*. in *Optical and Fiber Optic Sensor Systems*. 1998. International Society for Optics and Photonics.

52. Lee, B., *Review of the present status of optical fiber sensors.* Optical fiber technology, 2003. **9**(2): p. 57-79.

53. Vengsarkar, A.M., et al., *Long-period fiber gratings as band-rejection filters.* Journal of lightwave technology, 1996. **14**(1): p. 58-65.

54. Vengsarkar, A.M., et al., *Long-period fiber-grating-based gain equalizers.* Optics Letters, 1996. **21**(5): p. 336-338.

55. Wysocki, P.F., et al., *Broad-band erbium-doped fiber amplifier flattened beyond 40 nm using long-period grating filter.* IEEE Photonics Technology Letters, 1997. **9**(10): p. 1343-1345.

56. Qian, J. and H. Chen, *Gain flattening fibre filters using phase-shifted long period fibre gratings.* Electronics Letters, 1998. **34**(11): p. 1132-1133.

57. Gu, X., *Wavelength-division multiplexing isolation fiber filter and light source using cascaded long-period fiber gratings.* Optics letters, 1998. **23**(7): p. 509-510.

58. Lee, B.H. and J. Nishii, *Notch filters based on cascaded multiple long-period fibre gratings.* Electronics Letters, 1998. **34**(19): p. 1872-1873.

59. Ortega, B., et al., *High-performance optical fiber polarizers based on long-period gratings in birefringent optical fibers.* IEEE Photonics Technology Letters, 1997. **9**(10): p. 1370-1372.

60. Kurkov, A., et al., *Long-period fibre grating as a wavelength selective polarisation element.* Electronics Letters, 1997. **33**(7): p. 616-617.

61. Lee, K.S. and T. Erdogan, *Transmissive tilted gratings for LP/sub 01/-to-LP/sub 11/mode coupling.* IEEE Photonics Technology Letters, 1999. **11**(10): p. 1286-1288.

62. Ky, N.H., et al., *Efficient broadband intracore grating LP 01–LP 02 mode converters for chromatic-dispersion compensation.* Optics letters, 1998. **23**(6): p. 445-447.

63. Bhatia, V. and A.M. Vengsarkar, *Optical fiber long-period grating sensors.* Optics letters, 1996. **21**(9): p. 692-694.

64. Han, Y. *Performance enhancement of strain and temperature sensors using long period fiber grating*. in *13th International Conference on Optical Fiber Sensors*. 1999. International Society for Optics and Photonics.

65. Zhang, L., et al., *Design and realization of long-period grating devices in conventional and high birefringence fibers and their novel applications as fiber-optic load sensors.* IEEE Journal of Selected Topics in Quantum Electronics, 1999. **5**(5): p. 1373-1378.

66. Lee, B.H., et al., *Displacements of the resonant peaks of a long-period fiber grating induced by a change of ambient refractive index.* Optics Letters, 1997. **22**(23): p. 1769-1771.

67. Meissner, J., et al. *Strain monitoring at a prestressed concrete bridge*. in *Optical Fiber Sensors*. 1997. Optical Society of America.

68. Bao, X. and L. Chen, *Recent progress in distributed fiber optic sensors.* sensors, 2012. **12**(7): p. 8601-8639.

69. Boyd, R.W., *Nonlinear optics*. 2003: Elsevier.

70. Eickhoff, W. and R. Ulrich, *Optical frequency domain reflectometry in single‐mode fiber.* Applied Physics Letters, 1981. **39**(9): p. 693-695.

71. Farahani, M.A. and T. Gogolla, *Spontaneous Raman scattering in optical fibers with modulated probe light for distributed temperature Raman remote sensing.* Journal of Lightwave Technology, 1999. **17**(8): p. 1379.

72. Grandal, T., et al., *Analysis of fiber optic sensor embedded in metals by automatic and manual TIG welding.* IEEE Sensors Journal, 2019. **19**(17): p. 7425-7433.

73. Kong, C.Y. and R. Soar, *Method for embedding optical fibers in an aluminum matrix by ultrasonic consolidation.* Applied optics, 2005. **44**(30): p. 6325-6333.

74. Grandal, T., et al., *Laser cladding-based metallic embedding technique for fiber optic sensors.* Journal of Lightwave Technology, 2017. **36**(4): p. 1018-1025.

75. Claus, R., et al., *Embedded optical fiber sensors for materials evaluation.* Journal of Nondestructive Evaluation, 1989. **8**(2): p. 135-145.

76. Pan, X., D. Liang, and D. Li, *Optical fiber sensor layer embedded in smart composite material and structure.* Smart materials and structures, 2006. **15**(5): p. 1231.

77. Grandal, T., et al., *Laser Cladding-based metallic embedding technique for fiber optic sensors.* 2018. **36**(4): p. 1018-1025.

78. Havermann, D., et al., *Temperature and strain measurements with fiber Bragg gratings embedded in stainless steel 316.* 2015. **33**(12): p. 2474-2479.

79. Kuang, K., et al., *Embedded fibre Bragg grating sensors in advanced composite materials.* 2001. **61**(10): p. 1379-1387.

80. Gangopadhyay, T.K., P.C. Mukul, and L. Bjerkan. *Fiber-optic sensor for real-time monitoring of temperature on high voltage (400KV) power transmission lines*. in *20th International Conference on Optical Fibre Sensors, October 2009*. 2009.

81. Maier, R.R., et al., *Embedded fiber optic sensors within additive layer manufactured components.* 2013. **13**(3): p. 969-979.

82. Zou, R., et al. *Embedding Distributed Temperature and Strain Optical Fiber Sensors in Metal Components Using Additive Manufacturing*. in *CLEO: Applications and Technology*. 2018. Optical Society of America.

83. Zou, R., et al. *Optical fiber sensor-fused additive manufacturing and its applications in residual stress measurements*. in *CLEO: Applications and Technology*. 2017. Optical Society of America.

84. Mathew, J., et al. *SS316 structure fabricated by selective laser melting and integrated with strain isolated optical fiber high temperature sensor*. in *24th International Conference on Optical Fibre Sensors*. 2015. International Society for Optics and Photonics.

85. Li, Y., et al., *Metal coating of fiber Bragg grating and the temperature sensing character after metallization.* 2009. **15**(4): p. 391-397.

86. Li, X., *Embedded sensors in layered manufacturing*. 2001, Stanford University Stanford, CA, USA:.

87. Li, Y., et al., *Ultrasonic embedding of nickel-coated fiber Bragg grating in aluminum and associated sensing characteristics.* 2012. **18**(1): p. 7-13.

88. Sandlin, S., et al., *A simple method for metal re-coating of optical fibre Bragg gratings.* 2006. **201**(6): p. 3061-3065.

89. Yang, Q., et al., *Finite element modeling and validation of thermomechanical behavior of Ti-6Al-4V in directed energy deposition additive manufacturing.* 2016. **12**: p. 169-177.

90. Mandich, N. and D. Baudrand, *Troubleshooting electroplating installations: nickel sulfamate plating systems.* Plating and surface finishing, 2002. **89**(9): p. 68-76.

91. Vollertsen, F., *Mechanisms and models for laser forming.* Proc. of the LANE1994, 1994. **1**: p. 345.

92. Wang, Y., et al., *Energy-level effects on the deformation mechanism in microscale laser peen forming.* Journal of Manufacturing Processes, 2007. **9**(1): p. 1-12.

93. Niehoff, S.H. and F. Vollertsen, *Laser induced shock waves in deformation processing.* Metalurgija, 2005. **11**(3): p. 183-194.

94. Jiang, S.Q., et al. *Numerical analysis on the process of laser continuous peen forming of metal plate*. in *Key Engineering Materials*. 2008. Trans Tech Publ.

95. Fairand, B., et al., *Laser shock‐induced microstructural and mechanical property changes in 7075 aluminum.* Journal of Applied Physics, 1972. **43**(9): p. 3893-3895.

96. Clauer, A.H., J.H. Holbrook, and B.P. Fairand, *Effects of laser induced shock waves on metals*, in *Shock waves and high-strain-rate phenomena in metals*. 1981, Springer. p. 675-702.

97. Jiang, Y., et al., *Research on precision control of sheet metal forming by laser shock waves with semi-die.* Optics & Laser Technology, 2013. **45**: p. 598-604.

98. Ye, Y., et al., *Mold-free fs laser shock micro forming and its plastic deformation mechanism.* Optics and Lasers in Engineering, 2015. **67**: p. 74-82.

99. Ye, Y., et al., *Experimental research on laser shock forming metal foils with femtosecond laser.* Applied surface science, 2013. **285**: p. 600-606.

100. Hua, D., W. Yun, and C. Lan, *Laser shock forming of aluminum sheet: Finite element analysis and experimental study.* Applied Surface Science, 2010. **256**(6): p. 1703-1707.

101. Sagisaka, Y., et al., *Application of Femtosecond Laser Peen Forming to Sheet Metal Bending.* Journal of Laser Micro/Nanoengineering, 2012. **7**(2).

102. Ocaña, J.L., et al., *Nanosecond laser shock microforming of thin metal components.* Journal of Laser Micro/Nanoengineering, 2009. **4**: p. 55-60.

103. Clauer, A.H., B.P. Fairand, and J.E. Slater, *Laser shocking of 2024 and 7075 aluminum alloys*. 1977.

104. Fairand, B. and A. Clauer. *Applications of laser-induced stress waves*. in *Lasers in Modern Industry Seminar*. 1978.

105. Clauer, A.H. and D.F. Lahrman. *Laser shock processing as a surface enhancement process*. in *Key Engineering Materials*. 2001. Trans Tech Publ.

106. Peyre, P., et al., *Experimental study of laser-driven shock waves in stainless steels.* Journal of applied physics, 1998. **84**(11): p. 5985-5992.

107. Hong, X., et al., *Confining medium and absorptive overlay: Their effects on a laser-induced shock wave.* Optics and Lasers in Engineering, 1998. **29**(6): p. 447-455.

108. Auroux, E., et al., *Debonding study of Ni-base substrate/Pt coatings interfaces using laser shock waves: characterization of the targets and experimental study.* Surface and Coatings Technology, 2001. **138**(2-3): p. 269-277.

109. Peyre, P., et al., *Laser-shock processing of aluminium-coated 55C1 steel in water-confinement regime, characterization and application to high-cycle fatigue behaviour.* Journal of materials science, 1998. **33**(6): p. 1421-1429.

110. Peyre, P., et al. *Laser-shock processing of materials and related measurements*. in *High-Power Laser Ablation*. 1998. International Society for Optics and Photonics.

111. Ding, K. and L. Ye, *Laser shock peening: performance and process simulation*. 2006: Woodhead Publishing.

112. Bass, M., et al., *Handbook of optics, volume i: Geometrical and physical optics, polarized light, components and instruments (set)*. 2009: McGraw-Hill, Inc.

113. Phillips, J.D., M.E. Goda, and J. Schmidt. *Atmospheric turbulence simulation using liquid crystal spatial light modulators*. in *Advanced Wavefront Control: Methods, Devices, and Applications III*. 2005. International Society for Optics and Photonics.

114. Gerchberg, R.W., *A practical algorithm for the determination of phase from image and diffraction plane pictures.* Optik, 1972. **35**: p. 237.

115. Pence, C., et al., *Experimental analysis of sheet metal micro-bending using a nanosecond-pulsed laser.* The International Journal of Advanced Manufacturing Technology, 2013. **69**(1-4): p. 319-327.

116. Montross, C., V. Florea, and J. Bolger, *Laser-induced shock wave generation and shock wave enhancement in basalt.* International journal of rock mechanics and mining sciences (1997), 1999. **36**(6): p. 849-855.

117. AlMangour, B. and J.-M. Yang, *Improving the surface quality and mechanical properties by shot-peening of 17-4 stainless steel fabricated by additive manufacturing.* Materials & Design, 2016. **110**: p. 914-924.

118. Cottam, R., et al., *The role of microstructure in the stress relaxation and tempering of laser clad Ti–6Al–4V.* Materials Science and Engineering: A, 2014. **601**: p. 65-69.

119. Damon, J., et al., *Process dependent porosity and the influence of shot peening on porosity morphology regarding selective laser melted AlSi10Mg parts.* Additive Manufacturing, 2018. **20**: p. 77-89.

120. Zhang, P. and Z. Liu, *Effect of sequential turning and burnishing on the surface integrity of Cr–Ni-based stainless steel formed by laser cladding process.* Surface and Coatings Technology, 2015. **276**: p. 327-335.

121. Zhuang, W., et al., *Deep surface rolling for fatigue life enhancement of laser clad aircraft aluminium alloy.* Applied Surface Science, 2014. **320**: p. 558-562.